Synthesis, Characterization and Structure-Property Relationship of Alkali Metal Tungsten Bronzes

Dissertation

zur Erlangung des Doktorgrades der Naturwissenschaften

-Dr. rer. nat.-

Vorgelegt dem Promotionsausschuss

des Fachbereichs 02 (Biologie/Chemie)

der Universität Bremen

von

Md. Shahidur Rahman

Chemische Kristallographie fester Stoffe

Bremen, im März 2015

Erstgutachter: Prof. Dr. Thorsten M. Gesing (Universität Bremen)

Zweitgutachter: Prof. Dr. Reinhard X. Fischer (Universität Bremen)

Tag des Kolloquiums: 8. Mai 2015

Statement of Authorship

I, the undersigned, hereby declare that I am the sole author of this thesis. I have fully acknowledged and referenced the ideas and work of others, whether published or unpublished. My thesis does not contain work extracted from a thesis, dissertation or research paper previously presented for another degree at this or any other university. I have prepared my thesis specifically for the degree of Dr. rer. nat., while under supervision at University of Bremen.

(Md. Shahidur Rahman)
University of Bremen
Bremen, Germany

Acknowledgement

I have a great pleasure to acknowledge with sincere appreciation and deepest sense of gratitude to my supervisor, Prof. Dr. Thorsten M. Gesing, Solid State Chemical Crystallography at Institute of Inorganic Chemistry, University of Bremen, Germany; for his scholastic supervision, suggestions and constructive guidance to carry out this research work.

I would like to acknowledge with pleasure and great thanks to Prof. Dr. Reinhard X. Fischer, Department of Geosciences, University of Bremen, Germany; for his scholastic suggestions and being a reviewer of this research work.

My heartfelt thanks to all the members of the PhD defense panel, all the members of Solid State Chemical Crystallography, and all the members of Crystallography, University of Bremen; for their helps, important discussions, suggestions and guidelines.

I am highly obliged to Dr. M. Murshed, Solid State Chemical Crystallography, at Institute of Inorganic Chemistry, University of Bremen, Germany; for guidance, scientific discussions, and carefully monitoring this research work.

Thanks a lot to Dr. Stefan Zander, Helmholtz Zentrum Berlin, Germany; Dr. Ashfia Huq Oak Ridge National Laboratory, USA; Dr. Siidra Oleg, Saint Petersburg State University, Russia; for allocation of beam time and facilities.

Thanks a lot to Prof. Dr. Altaf Hussain, Prof. Dr. Pradip Kumar Bakshi, Prof. Dr. Md. Abdus Salam, Prof. Dr. Md. Aftab Ali Shaikh, Associate Prof. Dr. Tapas Debnath, Department of Chemistry, University of Dhaka, Bangladesh; and Prof. Dr. Katsuyuki Aoki, Department of Materials Science, Toyohashi University of Technology, Aichi, Japan; for their kind helps and inspirations.

My earnest thanks to Thorsten and his family, Murshed and his family, Lars, Gabi, Julia, Irma, Kristin, Pei, Malik, Michael, Andrea, Ariane, Niels, Hilke, Mathias, Elena, Uwe, Günter, Hanna, Li, Miriam, Jenny, Anja, Sanja, Christian and Marc for their cordial helps, cooperation, friendly and lovely activities.

Besides, I would like to thank all of my friends, colleagues, students and well wishers in Germany, Japan, Bangladesh, and all over the world who always make my life happy.

I would also like to thank to my loving parents, brothers and sisters for their constant encouragement for carrying out this research work.

Finally, I would like to thank University of Bremen, Germany for financial support as well as for others facilities to carry out this research work.

Dedicated to my beloved parents

CONTENTS

Publications within this thesis

Full paper

1. **M. S. Rahman**, M. M. Murshed, Th. M. Gesing, Synthesis, characterization and time dependent phase transformation of $Li_{0.4}WO_3$ bronze, Z. Kristallogr. 229(12) (2014) 797–805.
2. **M. S. Rahman**, M. M. Murshed, Th. M. Gesing, Tantalum and vanadium substitution in hexagonal $K_{0.3}WO_3$ bronze: synthesis and characterization, Z. Kristallogr. (submitted).
3. **M. S. Rahman**, M. M. Murshed, Th. M. Gesing, Thermal behaviors of lithium tungsten bronzes, (manuscript in preparation).
4. **M. S. Rahman**, M. M. Murshed, Th. M. Gesing, Preparation and characterization of tantalum and vanadium substituted hexagonal $Rb_{0.3}WO_3$ bronzes, (manuscript in preparation).
5. A. Schaefer, N. Lefeld, **M. S. Rahman**, M. Murshed, Th. Gesing, Effects of air exposure and vacuum storage on $Li_{0.4}WO_3$ studied by photoelectron spectroscopy, (manuscript in preparation).

Conference contributions

1. **M. S. Rahman**, M. M. Murshed, Th. M. Gesing, A study on alkali metal tungsten bronzes, Christmas colloquium, FB 02 (Biology/Chemistry), University of Bremen, 17.12.2012.
2. **M. S. Rahman**, M. M. Murshed, Th. M. Gesing, Synthesis, characterization and phase transition of $Li_{0.4}WO_3$ bronze, Z. Kristallogr. Suppl. 33 (2013) 75.
3. **M. S. Rahman**, M. M. Murshed, Th. M. Gesing, Tantalum and vanadium substitution in potassium tungsten bronzes, 16th NDDK, p 53, 19.-20. 09. 2013, Bremen, Germany.
4. **M. S. Rahman**, M. M. Murshed, Th. M. Gesing, Tantalum and vanadium substitution in potassium tungsten bronzes, ISBN 978-3-981-6508-2-2, p 132-133.
5. **M. S. Rahman**, M. M. Murshed, Th. M. Gesing, A study on alkali metal tungsten bronzes, 1st Meeting of the Young Crystallographers (DGK), p 15, 28.-30.09.2014, Bremen, Germany.
6. **M. S. Rahman**, M. M. Murshed, M. Fischer, A. Huq, Th. M. Gesing, Thermal expansion anomaly in lithium tungsten bronzes, Z. Kristallogr. Suppl. 35 (2015) 102.
7. N. Lefeld, A. Schaefer, M. M. Murshed, **M. S. Rahman**, M. Bäumer, Th. M. Gesing, Time-dependent X-ray photoelectron spectroscopic studies on $Li_{0.4}WO_3$, Z. Kristallogr. Suppl. 35 (2015) 133.

Parts of these publications were reproduced within this thesis.

INTRODUCTION

1.1. Tungsten bronzes

The tungsten bronzes are interesting and highly appreciable family of materials. They are not associated to the bronze, an alloy of copper and tin, apart from the coloration in some cases. The name 'bronze' originates since 1823 given by Friedrich Wöhler [1]. The tungsten bronzes may be considered to be the high-symmetry forms of WO_3; those are stable by the presence electropositive cations into tetragonal, pentagonal or hexagonal channels. In particularly, tungsten bronzes are a group of well-known non-stoichiometric compounds of general formula A_xWO_3, formed by the host tungsten trioxide-matrix (WO_3) and guest A^{n+} cation with different x-compositions (A^{n+} refers to an electropositive cation, such as elements of group 1, 2, 13, 14, lanthanides series etc.). In the WO_3 structure each tungsten atom is surrounded by six oxygen atoms, producing WO_6 octahedra, which are linked by corner-sharing common oxygen atoms in a three-dimensional network. The displacement of tungsten atom from the center of an octahedron takes place with the change of temperature, resulting in the symmetry change of the WO_3 octahedron [2]. There are several well defined polymorphic structures of WO_3, which are stable within a given temperature range and transform reversibly [3]. Triclinic, monoclinic, orthorhombic and tetragonal phases are most stable structural modifications of WO_3 which are observed in the temperature range of 93 K to 1173 K [4]. WO_3 having hexagonal symmetry has also been prepared by soft methods [5]. Tungsten trioxide, WO_3, a semiconductor material, and structurally a close relative of perovskite, is the active material in many chromic windows [6].

In 1935, Hägg described that all sodium tungsten bronzes of cubic symmetry are not different compounds but members of a continues series of solid solutions corresponding to a general formula Na_xWO_3 of variable x-values with a very extended homogeneity range $0.32 \leq x \leq 1$ [7, 8]. The theoretical upper limit of x is equal to one, and where all the tungsten atoms are in the pentavalent state; the resultant bronzes have complete perovskite-type structures. With decreasing statistically distributed sodium atoms generated vacant positions in the original lattice and a corresponding number of tungsten atoms acquire the highest oxidation state six. Tungsten bronzes have received much attention since 1823 [1] after the discovery of sodium tungsten bronze and other alkali metal tungsten bronzes [9, 10, 11] were discovered by many

distinguished researchers. In the earlier time it was considered that tungsten bronzes were stoichiometric compounds until 1935. Afterwards, lots of data were accumulated for different types of tungsten bronzes especially to investigate their crystal structures [12, 13, 14, 15, 16] and for interesting physical properties such as electrical [17], magnetic [18], electrochromic [19], and superconductivity [20, 21, 22, 23].

Another type of tungsten oxide materials are the fully oxidized phases where W^{5+} cations are completely replaced by others low-valance cations and analogous to the bronzes, called bronzoid [24] compounds. Reports have been published which illustrate that the pentavalent tungsten cations from the tungsten bronze can be replaced by other pentavalent cations such as Nb^{5+} or Ta^{5+} to produce bronzoid materials [25, 26, 27, 28]. Other lower valence metal cations also can replace tungsten for giving fully oxidized phases. Sabatier et al. [29] reported that monovalent (Li), divalent (Mg), trivalent (Cr), tetravalent (Ti), and hexavalent (Mo) cations can also partially substitute tungsten in appropriate amount, the resultant phases are entirely oxidized compounds.

The alkali metal tungsten bronzes can also be represent with a general formula $A_x(W^{6+}_{1-x}W^{5+}_x)O_3$, which indicates the presence of penta- and hexavalent tungsten in the same bronze composition. The assumption has been described by Yang et al. [30] and Gu et al. [31] from their investigations of the tetragonal and hexagonal tungsten bronzes of composition K_xWO_3 using X-ray photoelectron spectroscopy and reported the presence of W^{5+} and W^{6+} cations in the same compound. A number of articles have been published describing the substitution of W^{5+} cations from tungsten bronze by pentavalent cations of suitable sizes such as Nb^{5+} and Ta^{5+} cations. The resultant compounds showed higher electrical resistivity due to the presence of d^0 electronic configuration Nb^{5+} and Ta^{5+} cations [32, 33, 34]. Weller et al. [32] prepared about 10 % Nb^{5+} or Ta^{5+} incorporated sodium tungsten bronzes by electrolytic reduction. Nb^{5+} containing solid solution series of $Na(W_{1-y}Nb_y)O_3$ were prepared by Miyamoto et al. [33] at high-temperature (1823 K) and high-pressure (6 GPa) conditions. It was found that with a composition of $y \approx 0.16$ and for $0.52 \leq y \leq 1$ produced cubic structure. Dubson et al. [34] also reported tantalum substituted sodium tungsten bronzes, prepared by electrolytic reduction. In 2002, Hussain et al. [35] published the results of Nb^{5+} substituted hexagonal tungsten bronzes of potassium and rubidium. Dey et al. [36] also worked on Nb and Mo substitution in the cubic (Li_xWO_3) and hexagonal (Cs_xWO_3) tungsten bronze structures. Recently, attempts were

made for the synthesis and composition-structure relationship of Nb^{5+} substituted cubic perovskite-type sodium tungsten bronzes and tetragonal potassium tungsten bronzes [37, 38]. Additional attempts were made for the synthesis of Ta^{5+} or V^{5+} cations substituted hexagonal potassium tungsten bronzes [39, 40] using solid state synthesis method. However, details of the structural features are missing and the associated physical properties could not be explained so far.

1.2. Crystal chemistry of tungsten bronzes

Tungsten bronzes, $A_x(W^{6+}_{1-x}W^{5+}_x)O_3$ undergo one or more structural phase transitions when x is varied from zero to one, high x-values produced high-symmetry and low x-values resulting in the low-symmetry phases [41]. The crystal structure of $A_x(W^{6+}_{1-x}W^{5+}_x)O_3$ bronze is built up by corner-sharing WO_6 octahedron (building units) forming different type of channels into which the A^+ cations are sited. The number of octahedral units forming a ring leading to channels varies from three to six as a function of the type of A^+ cation as well as the concentration x. Ngai et al. [42, 43] explained this variation in terms of the optimization of the free energy for each ring type and also associated with placing the A^+ cation in the tunnel environment. So far there are four different types of tungsten bronzes based on their crystal structures. These are (a) perovskite-type tungsten bronzes (PTB); (b) tetragonal tungsten bronzes (TTB); (c) hexagonal tungsten bronzes (HTB); and (d) intergrowth tungsten bronzes (ITB). The size and the concentration of the guest atoms, and the preparation-conditions play major roles for the formation of different types of tungsten bronze structures. Brief structural descriptions of each type of tungsten bronze are given below.

1.2.1. Perovskite-type tungsten bronzes (PTB)

Tungsten bronzes are formed when ternary metal atoms are in the channels present in the host WO_3-matrix. If all these channels are filled, the structure would have composition AWO_3, identical to perovskite structure. It is not observed that all the channels are occupied in the tungsten bronze family; they are non-stoichiometric phases A_xWO_3 in which the available sites are only partially filled. It is observed that WO_6 octahedra produce tetragonal channels by sharing common-corner oxygen atoms, and the metal atoms are in the channels. The crystal structures of PTB can be explained by taking into account three important factors: (a)

distortions of the WO_6 octahedral units, (b) displacement of the W atom within the octahedra, and (c) tilting of the common corner-shared WO_6 octahedra. PTB structure allows only smaller cations with a maximum radius of 130 pm at normal pressure. Therefore, among the alkali metals Li and Na, and H are suitable candidates to form PTB structure.

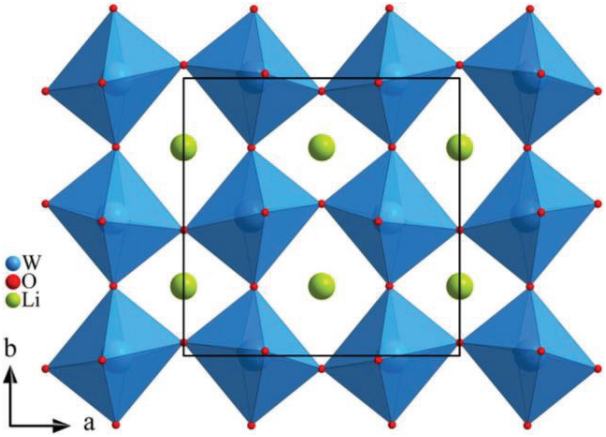

Figure 1.1(a). Crystal structure model of orthorhombic perovskite-type tungsten bronze (PTB_O) of space group *Pcnb*.

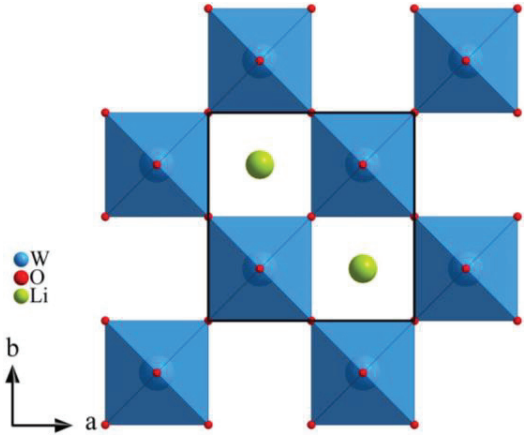

Figure 1.1(b). Crystal structure model of tetragonal perovskite-type tungsten bronze (PTB_T) of space group *P4/nmm*.

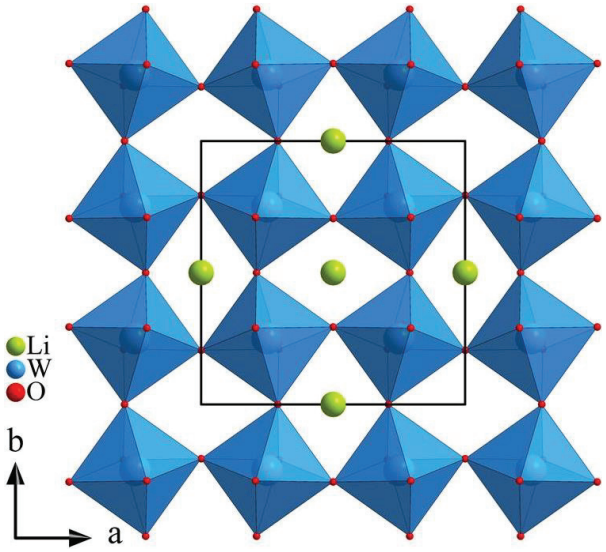

Figure 1.1(c). Crystal structure model of body-centered cubic perovskite-type tungsten bronze (PTB_{CI}) of space group $Im\bar{3}$.

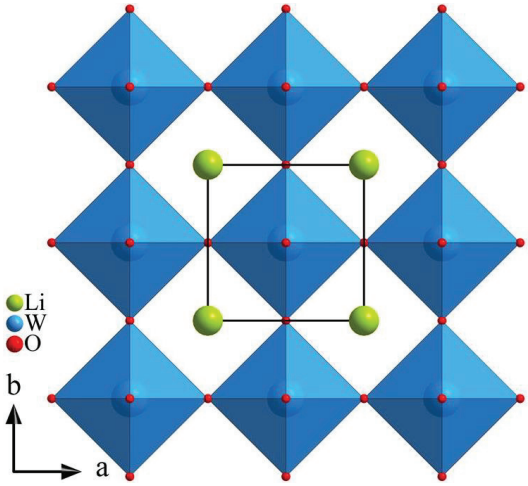

Figure 1.1(d). Crystal structure model of cubic perovskite-type tungsten bronze (PTB_{CP}) of space group $Pm\bar{3}m$.

As a step toward, perovskite-type tungsten bronze can be divided into three crystal systems; orthorhombic perovskite-type tungsten bronze (PTB_O), tetragonal perovskite-type tungsten bronze (PTB_T), cubic perovskite-type tungsten bronze (PTB_C) [44] as shown in Figure 1.1. For example, Na_xWO_3 has pure PTB_O structure in the range of $0.03 \leq x \leq 0.04$, pure PTB_T phase when x stands for $0.07 \leq x \leq 0.11$, and pure PTB_C for $x \geq 0.43$, and all these are stable at 298 K [44]. The tilting of the WO_6 octahedral units resulted the lower symmetric PTB_O phase. The low-content guest cations A^+ (low x concentration) are statistically distributed into the tetragonal channels. The anti-ferroelectric pattern of the cations displacement seems to be restricted in the PTB_O structure. The PTB_T structure is generated by the displacement of tungsten within the WO_6 octahedra. Magnéli [45] determined the crystal structures of A_xWO_3 (A = Li, Na) bronzes having PTB_T symmetry of space group *P*4/*nmm*. Dey et al. [46] reported that $Li_{0.1}WO_3$ bronze also crystallized in the space group *P*4/*nmm*. Conversely, Rüscher et al. [47] proposed that $Li_{0.1}WO_3$ might be produced in the space group *P*4/*nmm* or *P*4/*ncc*. Space group *P*4/*ncc* is possible when tungsten atoms have anti-ferroelectric displacement within the octahedra as well as the octahedral units go through tilting around the **z**-axis. Many reports described that Na_xWO_3 and Li_xWO_3 bronzes also crystallized in the PTB_C structure of space group $Pm\bar{3}m$ [48, 49]. However, precise experimental techniques such as neutron powder diffraction data showed that there are super structure reflections in the diffraction patterns of those materials. These are crystallized as body-centered cubic symmetry (space group $Im\bar{3}$) instead of primitive cubic space group $Pm\bar{3}m$. Wiseman et al. [50] refined neutron diffraction data for $Li_{0.36}WO_3$ bronze in the space group $Im\bar{3}$ and showed that the WO_6 octahedra are tilted about 13° while in the space group $Pm\bar{3}m$ there is no such octahedral tilting.

1.2.2. Tetragonal tungsten bronzes (TTB)

This type of tungsten bronzes are formed when WO_6 octahedral units undergo various degree of tilting for forming trigonal, tetragonal and pentagonal channels within the same framework. The A^+ cation can be found either tetragonal or pentagonal or both channels, preferentially into the larger dimensional pentagonal channels (Figure 1.2). Among the alkali metals Na and K prefer to form TTB structure. Magnéli determined the TTB structure of K_xWO_3 (x = 0.4 – 0.6) bronzes [51]. In the structural investigation of $K_{0.37}WO_3$, it is reported that about 88 % K^+ cations were situated in the pentagonal channels and about 12 % were found in the tetragonal

tunnels [52]. All pentagonal and tetragonal channels were occupied by potassium correspond to the composition of $K_{0.6}WO_3$. TTB structure of Na_xWO_3 (x = 0.33 and 0.48) were published by Takusagawa [53], and reported that Na^+ cations prefer to occupy the pentagonal channels first then with a higher x-concentration also occupies tetragonal channels. Therefore, $Na_{0.48}WO_3$ has less distorted structure than $Na_{0.33}WO_3$ bronze, because in the $Na_{0.48}WO_3$ structure all the pentagonal and about 40 % tetragonal tunnels were occupied by sodium whereas only pentagonal channels were occupied in the $Na_{0.33}WO_3$ composition.

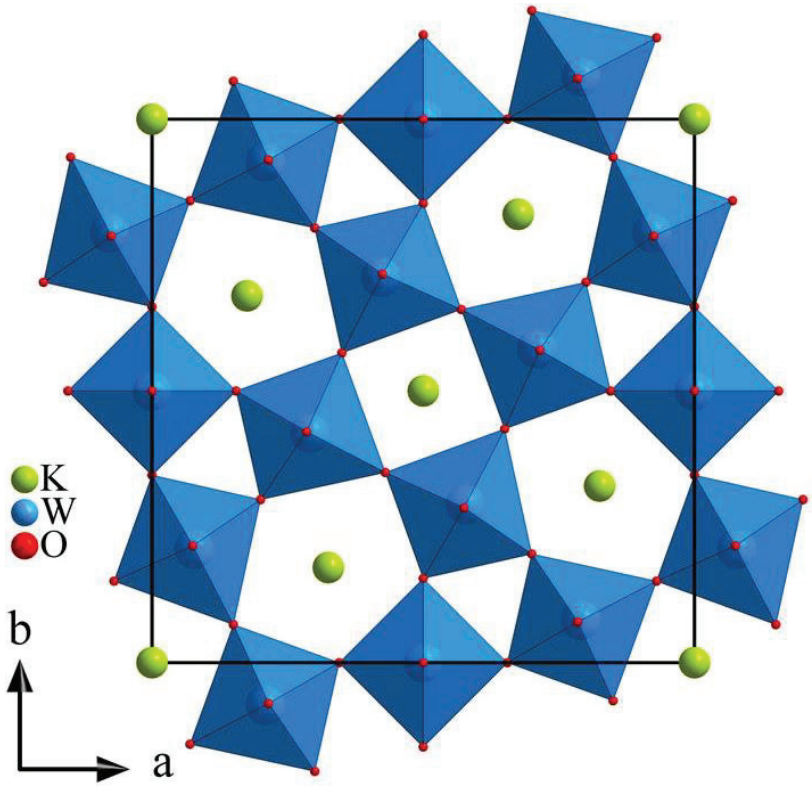

Figure 1.2. Crystal structure model of tetragonal tungsten bronze (TTB) of space group *P*4/*mbm*.

1.2.3. Hexagonal tungsten bronzes (HTB)

In these systems, an arrangement of corner sharing WO_6 octahedra provides the main framework of the structure. In the structure two axial oxygen atoms are situated along the **c**-direction while four equatorial oxygen atoms are positioned in the *xy*-plane. The packing is such that they leave triangular and hexagonal tunnels. The guest A^+ cations reside in the hexagonal tunnels (Figure 1.3). The triangular rings are rather small compared to the ionic

radii of incorporated guest atoms. In 1953, Magnéli discovered HTB structure for $Rb_{0.29}WO_3$ bronze [54]. Since the channel dimension for HTB is larger than those in PTB or TTB, the larger cations can easily be positioned into the channels of the HTB structure [55]. Alkali metal cations (K, Rb, Cs), and a number cations of other elements or ions like NH_4^+, Ca, Ba, Sn, Tl, Nd, etc. produced HTB structure [56, 57, 58, 59]. The maximum composition of the inserted gust atom for the formation of pure HTB phase is x = 0.33, where A^+ cations occupies all available hexagonal tunnels.

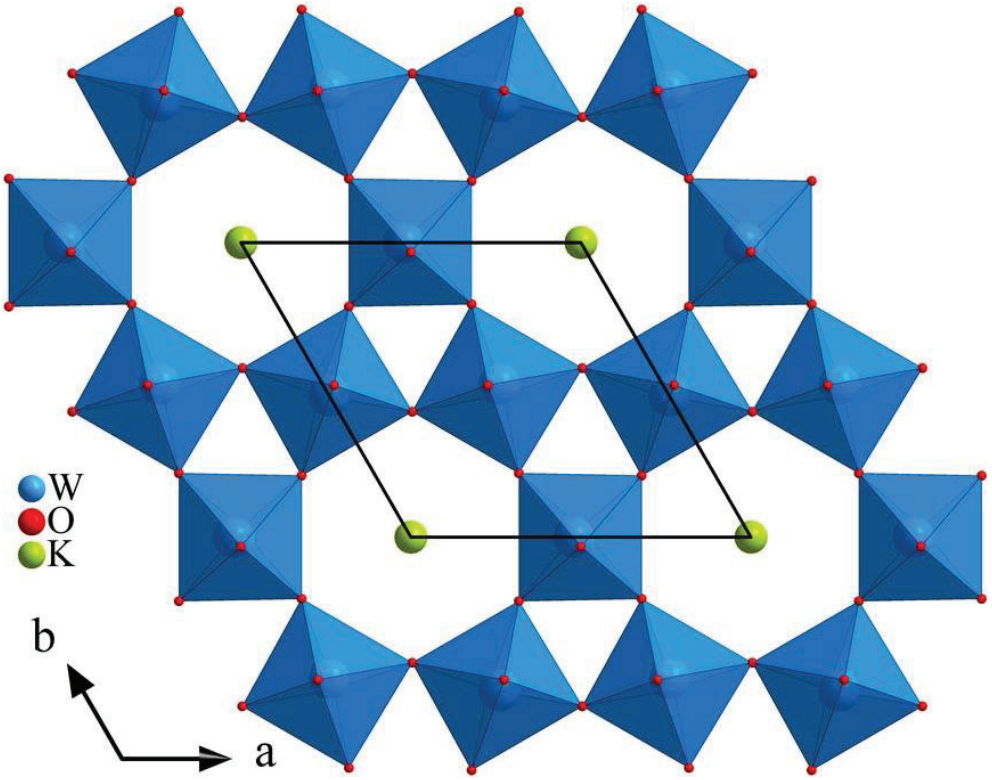

Figure 1.3. Crystal structure model of hexagonal tungsten bronze (HTB), possible space groups are $P6_3$, $P6_322$ or $P6_3/mcm$.

1.2.4. Intergrowth tungsten bronzes (ITB)

Low concentrations ($0.01 \leq x \leq 0.12$) of heavier alkali metals (K, Rb, Cs) produced less stable HTB structure, and ITB structure is formed instead of HTB (Figure 1.4) [60, 61]. The ITB crystals are flaky with shiny faces, and formed with an elongated structure [60, 61]. It consists of alternating HTB and WO_3 slabs within the same structure. In this structure, the WO_6 octahedra are tilted by about 15° in an alternating sequence to build WO_3 slabs and allow the

two slabs fit together. The WO_3 structure becomes more compact because of tilting. The slabs of WO_3 can be different widths and inter-grown with single or double slices of HTB structure. Hussain et al. [60, 61] introduced the nomenclature of ITB, e.g. a single row of hexagonal tunnels structures separated by n (n = 2, 3, 4) slabs of WO_6 octahedra denoted (n)-ITB, while ITB containing double hexagonal tunnels separated by n-chains of WO_6 octahedra designated (1, n)-ITB. A large variation of tunnel occupancy in the ITB, A_xWO_3 (A = Cs, Ba, Sn, Sb) has also been observed [62, 63, 64]. Zakharov et al. prepared (2)-ITB of $(Nd, Ca)_xWO_3$ [65] and (n)-ITB of Pr_xWO_3 (n = 2, 3, 4) [66] using a pressure of 5 $\bullet 10^3$ MPa and 1570 K. The ITB phases with different alkali metals, or others elements behave similarly and many of them have orthorhombic symmetry.

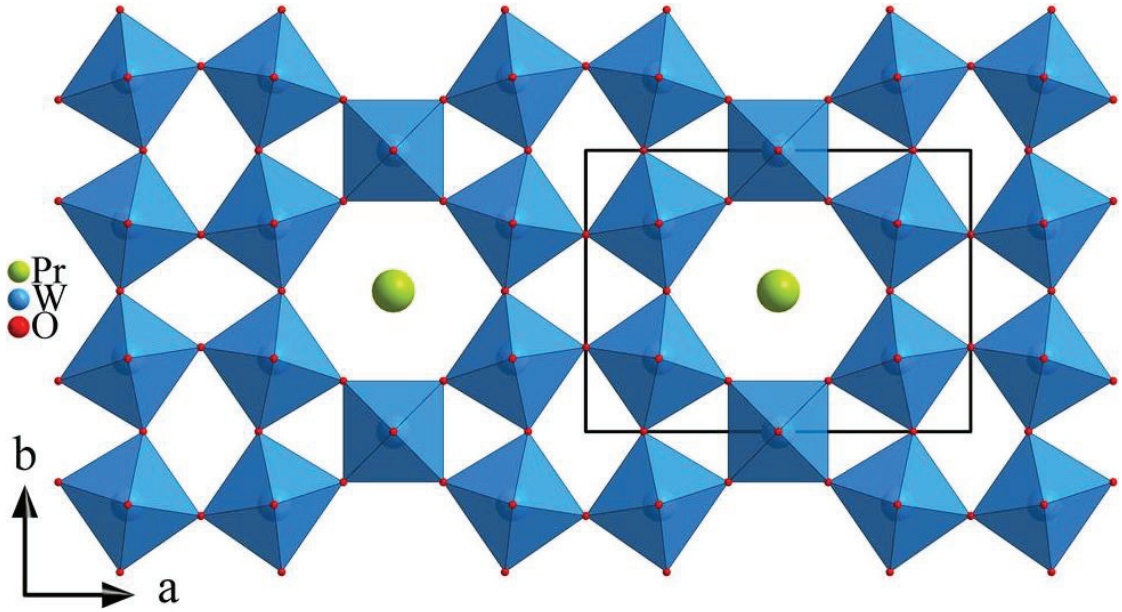

Figure 1.4. Crystal structure model of intergrowth tungsten bronze, ((2)-ITB) of space group *P*222).

Sharma [67] reported a series of intergrowth tungsten bronzoids of composition $Cs_xNb_xW_{1-x}O_3$ (x = 0.08 – 0.12) and described the structure with respect to x-composition using high resolution electron microscopy. In the pure HTB, the homogeneity range is $0.19 \leq x \leq 0.33$, which shows a varying degree of filling of the channel sites. All the channels are completely filled for x = ⅓. However, Nb containing cesium tungsten bronzoid, crystallized in the HTB structure, has a very narrow range of homogeneity around x = 0.2, which implies about 60 % of the tunnels sites are filled. In the ITB phases the possible correlation between the alkali

content and the structure is complicated because it was not possible to prepare single-phase products.

1.3. Properties of tungsten bronzes

The properties of tungsten bronzes or bronzoid-type materials depend on many factors such as concentration of the incorporated cations, methods of synthesis, keeping environments, preparation temperatures and pressures, and on the nature of the inserted cations, particularly. Tungsten bronzes have many fascinating properties such as intense color, metallic luster, metallic or semi-metallic conductivity, and inertness towards strong acids and alkalis. The immense attention for tungsten bronzes have received because of their interesting electrical, optical and magnetic properties. In the next part some of the interesting properties are described in brief.

1.3.1. Electrical properties

Extensive attentions have been aroused by the unusual electrical conductivities of tungsten bronzes. The electrical conductivity of sodium tungsten bronzes as a function of temperature were measured by Hägg [8], and found them to be electronic semiconductors. Indeed the conducting properties of tungsten bronzes have been observed when the measurement is done on powder samples [68]. However, Brown and Banks [69] measured the electric conductivity on the single crystals of Na_xWO_3 bronzes and found the resistivity increases almost linearly with temperature from 125 K to 600 K, within the broad compositional range, $0.53 \leq x \leq 0.85$; a property characteristic of metals. Ellerbeck et al. [70] reinvestigated such measurement on single crystals of Na_xWO_3 prepared by electrolysis technique, carefully homogenized the materials by thermal annealing at 920 K for 24 hours. There was no minimum resistivity at any temperature; nonetheless, the resistivity has a tendency to vary only slightly with the x-concentration for $x \geq 0.7$. The authors ascribed the minimum found by Brown and Banks to the use of single crystals containing domains of different composition, the maximum homogeneity corresponding to the minimum resistivity.

In 1963, Shanks et al. [71] reported that the alkali metal (Li, Na, K) tungsten bronzes are metallic when $x > 0.25$ and semiconductor for $x < 0.25$. It was also concluded that the resistivity is only the function of x-composition and approximately independent on the nature

of alkali metals (Li, Na and K). The observed electrical conductivity of these metal tungsten bronzes showed that the alkali metals within the bronzes do not participate in the conduction mechanism at room-temperature. At certain temperature the mobility can only be due to a scattering of electrons by the lattice vibration and by the insertion ion vacancies in the tunnels. The semiconductor properties of the tungsten bronzes having a low concentration of insertion elements implies rather a localization of the *d*-orbital electrons into 5*d* orbital of the t_{2g} symmetry at specific tungsten atoms. Straumanis et al. [49] studied various single and mixed bronze systems and observed that the cubic lithium tungsten bronze of highest alkali content shows considerable ionic conductivity. This result was explained as due to the lithium atoms being small enough and able to slip through the open space between the WO_6 octahedra of the lattice.

Superconductivity of tungsten bronzes has been known since 1964 [20]. The hexagonal tungsten bronzes of potassium, rubidium and cesium show superconductivity with T_c around 1.5 K [72, 73]. The main WO_3-matix is an insulator because the empty 5*d* orbitals of tungsten were hybridized with the 2*p* orbitals of oxygen atoms resulting in an occupied valance band and an empty conduction band. The alkali metal atoms, A donate their *s* orbital electron to the conduction band of WO_3 giving rise to the metallic and eventually superconducting transition [17]. The interesting and remarkable feature of these materials is that the superconducting properties can be tuned by controlling the stoichiometry and the lattice dynamical properties can be controlled by changing the nature of the inserted cations.

1.3.2. Magnetic properties

Magnetic susceptibility measurements were carried out on single crystals of cubic sodium tungsten bronzes (Na_xWO_3; $0.45 < x < 1$) and were found to be weak temperature independent paramagnetic [74] from 70 K to 300 K for three representative samples with x = 0.49, 0.76 and 0.85. The susceptibility of WO_3 was also measured and it also showed temperature independent magnetic susceptibility. The observed and calculated susceptibilities gave a satisfactory result and it assumes that the bronzes consist of dispersion of sodium cations into WO_3 lattice. Dickens and Whittingham [75] reported that the measurement made on powder samples of the alkali metal tungsten bronzes reveal similar behavior. The x-concentration dependent molar susceptibilities of lithium tungsten bronzes have been measured and were

found to be consistent with the magnetic susceptibilities calculated for an electron-gas model [76]. Lithium tungsten bronzes were found to be diamagnetic as the concentration of lithium in the bronze is reduced. A number of reports also mentioned temperature independent weak paramagnetic behavior of hexagonal potassium- rubidium- and cesium tungsten bronzes [13, 18, 77]. They found rubidium and some of the lithium and potassium bronzes are diamagnetic while sodium bronzes showed weak paramagnetism. Such variation is not clear yet; it may be well possible they use different sample preparation or measurement techniques. Hexagonal phase of indium tungsten bronze is isotropic diamagnetic [78] material. It was described by the compensation of the very weak Pauli paramagnetism by the diamagnetic indium into the system. Magnetic susceptibility measurement on single crystals of indium tungsten bronzes along the both crystallographic axes showed independency of the direction of the applied magnetic field.

1.3.3. Optical properties

Tungsten bronzes are the ternary or quaternary inorganic oxide materials which show attractive color variation depending on the amount of x-composition of the inserted guest cations. Noticeable color is one of the most interesting and characteristic property of tungsten bronzes. For this reason tungsten bronzes are attractive and useful pigments materials in the dyes and paints. Hägg [8] pointed out that the color of cubic sodium bronzes depends on the proportions of penta- and hexavalent tungsten cations are present in the lattice. The same relations were observed between the color and average valence of metal atoms for a great number of tungsten bronzes, binary oxides of tungsten and molybdenum [79]. This is also true for hexagonal tungsten bronzes, the colors which are comparable to that of the tetragonal tungsten bronzes of Na_xWO_3 ($x \sim 0.3$). It is also proposed that the color of the binary oxides of molybdenum (Mo) or tungsten (W) and the tungsten bronzes are essentially depends on the average oxidation state of Mo and W in the compounds. The variation of the x-composition affects the crystal structure and act as a color determining factor for tungsten bronzes and bronzoid materials. In tungsten bronzes, $A_x(W^{6+}_{1-x}W^{5+}_x)O_3$ the electrons are introduced in WO_3 lattice by the donor atoms are affected by strong electron-phonon coupling. These electrons are therefore self-trapped forming polarons rather than being free electron and that are characterized by their strong absorption feature in the near infrared spectral range tailing

into the visible range with increasing metal concentration, x. The spectral changes are dominated by the appearance of a Drude free carrier plasma frequency. Thus the visual appearance in Na_xWO_3 from greenish to blue via grey might be explained by the increase in polaron concentration from zero to above the metal insulator transition. As x-concentration is increased further to 1.0 the color changes to purple, red, orange and yellow. This can be explained by further increase in carrier concentration due to gradual shift in the plasma frequency through the visible part of the spectrum [80].

1.3.4. Chemical properties

The tungsten bronzes show inertness towards water or other common solvents, which makes their chemical analysis very difficult [79]. The chemical inertness may be associated with the high activation energy for the diffusion of alkali metal in the WO_3-matrix (216.88 $kJmol^{-1}$ for Na in $Na_{0.78}WO_3$) [81]. They react only with the chemicals capable of attacking the WO_3-lattice, the location of the inserted cations within the tunnels effectively protected from the common reagents. Hence acids, even in relatively strong concentration, have no reaction with the tungsten bronzes. These properties are of obvious interest for application purposes. Use as a catalyst in the strong acidic solution has been considered, especially. The tungsten bronzes are readily oxidized to tungstate of A^+ cation in the alkali media. They are capable to convert ammoniacal silver nitrate to metallic silver and this reaction may be useful for the quantitative analysis of these materials. Strong electron acceptors like iodine or tungsten(VI) oxide can degrade sodium tungsten bronzes to compounds of closer in composition to WO_3 [82]. Electron donors like molecular hydrogen cause the formation of compounds closer in composition to $NaWO_3$ [83, 84]. Conversely, the hydrogen tungsten bronzes, H_xWO_3 prepared by the wet reduction of tungstic acid are extremely reactive [85, 86]. They are slowly attacked by air and rapidly oxidized by hot dichromate solution. They are also deep blue and structurally related to the sodium tungsten bronzes, Na_xWO_3.

1.4. Intention of this research

This study has been carried out for the redetermination and confirmation of the crystal structures of some well-known alkali metal tungsten bronzes, in particularly structures of $Li_{0.1}WO_3$, $Li_{0.4}WO_3$ and $K_{0.3}WO_3$ bronzes. Physical properties of these bronzes and their

stability into different storing conditions are also an area of interest of this research work. Preparation of tungsten oxide bronzes and bronzoid-type compounds in which tungsten is partially replaced by pentavalent cations of two different ionic radii (tantalum or vanadium), miscibility limits of Ta^{5+} and V^{5+} in these systems and their structure-property relationships are another area of interest. The overall program of this research work fits with the following key points.

(a) Preparation of lithium tungsten bronzes, $Li_x(W^{6+}_{1-x}W^{5+}_x)O_3$ for x = 0.1, 0.2, 0.3, 0.4, 0.5, and 0.6.

(b) Characterization and crystal structure determination of lithium tungsten bronzes by X-ray and neutron powder diffraction.

(c) The effect of air pressure inside the reaction tubes, reaction-temperatures, and reaction-time for the preparation of $Li_{0.4}(W^{6+}_{0.6}W^{5+}_{0.4})O_3$ bronzes.

(d) Investigations of time-dependent phase transformations of $Li_{0.4}(W^{6+}_{0.6}W^{5+}_{0.4})O_3$ bronzes kept into different environments such as low-pressure conditions, ambient conditions, and sealed glass capillaries by fusing.

(e) Thermal behaviors of $Li_{0.1}(W^{6+}_{0.9}W^{5+}_{0.1})O_3$ and $Li_{0.4}(W^{6+}_{0.6}W^{5+}_{0.4})O_3$ bronzes by X-ray and neutron powder diffraction as well as Raman spectroscopy.

(f) Synthesis, characterization, and crystal structure redetermination of hexagonal potassium tungsten bronze of composition $K_{0.3}(W^{6+}_{0.7}W^{5+}_{0.3})O_3$ using powder X-ray diffraction and complementary Raman spectroscopy.

(g) Investigations of low-temperature powder X-ray diffraction data and Raman spectra of $K_{0.3}(W^{6+}_{0.7}W^{5+}_{0.3})O_3$ bronze.

(h) Synthesis and characterizations of tantalum (Ta^{5+}) or vanadium (V^{5+}) incorporated hexagonal tungsten bronzes (HTB's) of potassium or rubidium of compositions $A_{0.3}(W^{6+}_{0.7}W^{5+}_{0.3})O_3$ (A = K or Rb).

(i) The co-sharing effects of larger (Ta^{5+}) and smaller (V^{5+}) cations in the $K_{0.3}(W^{6+}_{0.7}W^{5+}_{0.3})O_3$ bronze.

(j) Structure-property relationship of HTB's in terms of out-of-center octahedral distortion of MO_6 octahedron.

(k) Substitution of tungsten (W^{5+}) by tantalum (Ta^{5+}) cations in cubic perovskite-type tungsten bronze (PTB_C) of composition $Na_{0.6}(W^{6+}_{0.4}W^{5+}_{0.6})O_3$.

EXPERIMENTAL

2.1. Synthesis

Series of samples of alkali metal (Li, Na, K, and Rb) tungsten bronzes and pentavalent cations (Ta^{5+} and V^{5+}) substituted tungsten bronzes of Na, K and Rb were prepared using conventional solid state synthesis method. Details of the synthesis procedures of different series of samples are described in the next parts.

2.1.1. Lithium tungsten bronzes, $Li_x(W^{6+}_{1-x}W^{5+}_x)O_3$ series

Polycrystalline samples of $Li_x(W^{6+}_{1-x}W^{5+}_x)O_3$ (x = 0.1, 0.2, 0.3, 0.4, 0.5, and 0.6) bronzes were synthesized using Li_2WO_4, WO_3 and WO_2 according to the chemical equation (2.1).

$$x/2\ Li_2WO_4 + (1\text{-}x)\ WO_3 + x/2\ WO_2 = Li_x(W^{6+}_{1-x}W^{5+}_x)O_3 \qquad (2.1)$$

Stoichiometric amounts of the starting materials were intimately mixed in an agate mortar and transferred into a seasoned quartz tube. The internal air pressure of the reaction tubes was reduced to 10^{-7} MPa. $Li_{0.4}(W^{6+}_{0.6}W^{5+}_{0.4})O_3$ bronzes were prepared using different air pressures from 10^{-2} MPa to 10^{-7} MPa. After sealing, the tubes were heated in a muffle furnace at 973 K for seven days and thereafter quenched in water to room-temperature. Single crystals, suitable sizes for single crystal X-ray diffraction measurements, were selected from mainly the polycrystalline samples for structural analysis of $Li_{0.4}(W^{6+}_{0.6}W^{5+}_{0.4})O_3$ bronze.

2.1.2. Tantalum and vanadium substituted potassium tungsten bronzes, $K_{0.3}(W^{6+}_{0.7}W^{5+}_{0.3-y}M^{5+}_y)O_3$ (M = Ta^{5+} and V^{5+}) solid solution series

Powder samples of $K_{0.3}(W^{6+}_{0.7}W^{5+}_{0.3-y}Ta^{5+}_y)O_3$, $K_{0.3}(W^{6+}_{0.7}W^{5+}_{0.3-y}V^{5+}_y)O_3$, and $K_{0.3}(W^{6+}_{0.7}W^{5+}_{0.3-y}Ta^{5+}_{y/2}V^{5+}_{y/2})O_3$ bronzes, as well as $K_y(W^{6+}_{1-y}Ta^{5+}_y)O_3$ bronzoid-type oxides (Table 2.1) were synthesized using K_2WO_4, WO_3, WO_2, Ta_2O_5, and V_2O_5 as the starting materials. The general chemical equations (2.2) and (2.3) were followed for their syntheses. Stoichiometric amounts of reactants were mixed in an agate mortar and transferred into a dry preheated quartz tube. The internal air pressure of the reaction tubes was reduced to 10^{-7} MPa. The tubes containing the reactants were sealed and heated in a muffle furnace at 1073 K for seven days. Thereafter, the samples were quenched in water to room-temperature.

$$x/2\ K_2WO_4 + (1\text{-}x\text{-}y/2)\ WO_3 + ½(x\text{-}y)\ WO_2 + y/2\ M_2O_5 = K_x(W^{6+}_{1-x}W^{5+}_{x-y}M^{5+}_y)O_3 \qquad (2.2)$$

$$y/2\ K_2WO_4 + (1\text{-}3y/2)\ WO_3 + y/2\ Ta_2O_5 = K_y(W^{6+}_{1-y}Ta^{5+}_{y})O_3 \qquad (2.3)$$

Table 2.1. Nominal composition of tantalum and vanadium substituted $K_{0.3}(W^{6+}_{0.7}W^{5+}_{0.3-y}M^{5+}_{y})O_3$ solid solution series.

$K_{0.3}(W^{6+}_{0.7}W^{5+}_{0.3-y}Ta^{5+}_{y})O_3$	y = 0, 0.05, 0.10, 0.15, 0.20, 0.25, 0.30
$K_{0.3}(W^{6+}_{0.7}W^{5+}_{0.3-y}V^{5+}_{y})O_3$	y = 0, 0.05, 0.08, 0.10, 0.13, 0.15, 0.16, 0.18
$K_{0.3}(W^{6+}_{0.7}W^{5+}_{0.3-y}Ta^{5+}_{y/2}V^{5+}_{y/2})O_3$	y = 0, 0.05, 0.10, 0.15, 0.20, 0.25, 0.30
$K_y(W^{6+}_{1-y}Ta^{5+}_{y})O_3$	y = 0.20, 0.24, 0.26, 0.28, 0.33

2.1.3. Rubidium tungstate, Rb_2WO_4

Rubidium tungstate (Rb_2WO_4) was prepared using $RbNO_3$ and WO_3 as starting materials. Stoichiometric amounts of the reactants (2:1) were intimately mixed in an agate mortar and transferred into a porcelain crucible. The mixture was heated in a muffle furnace at 1073 K for overnight using a heating rate of 100 K /h and a cooling rate of 200 K /h. The purity of the product was confirmed by powder X-ray diffraction.

2.1.4. Tantalum and vanadium substituted rubidium tungsten bronzes, $Rb_{0.3}(W^{6+}_{0.7}W^{5+}_{0.3-y}M^{5+}_{y})O_3$ (M = Ta^{5+} and V^{5+}) solid solution series

Series of polycrystalline powder samples of $Rb_{0.3}(W^{6+}_{0.7}W^{5+}_{0.3-y}Ta^{5+}_{y})O_3$, and $Rb_{0.3}(W^{6+}_{0.7}W^{5+}_{0.3-y}V^{5+}_{y})O_3$ (Table 2.2) bronzes were also prepared by conventional solid state synthesis method using Rb_2WO_4, WO_3, WO_2, Ta_2O_5, and V_2O_5 as starting materials. The chemical equation (2.4) was used to calculate the stoichiometric quantities of the reactants for this synthesis.

$$x/2\ Rb_2WO_4 + (1\text{-}x\text{-}y/2)\ WO_3 + \tfrac{1}{2}(x\text{-}y)\ WO_2 + y/2\ M_2O_5 = Rb_x(W^{6+}_{1-x}W^{5+}_{x-y}M^{5+}_{y})O_3 \qquad (2.4)$$

Table 2.2. Nominal composition of tantalum and vanadium substituted $Rb_{0.3}(W^{6+}_{0.7}W^{5+}_{0.3-y}M^{5+}_{y})O_3$ solid solution series.

$Rb_{0.3}(W^{6+}_{0.7}W^{5+}_{0.3-y}Ta^{5+}_{y})O_3$	y = 0, 0.05, 0.10, 0.15, 0.20, 0.25, 0.30
$Rb_{0.3}(W^{6+}_{0.7}W^{5+}_{0.3-y}V^{5+}_{y})O_3$	y = 0, 0.05, 0.08, 0.10, 0.12, 0.13, 0.14, 15

Stoichiometric amounts of the reactants were mixed in an agate mortar and transferred into a seasoned quartz tube. The internal air pressure of the reaction tubes was reduced to 10^{-7} MPa.

The sealed quartz tubes containing the reactants were heated in a muffle furnace at 1073 K for seven days. Thereafter, the samples were quenched in water to room-temperature.

2.1.5. Tantalum substituted sodium tungsten bronzes, $Na_{0.6}(W^{6+}_{0.4}W^{5+}_{0.6-y}Ta^{5+}_{y})WO_3$ solid solution series

Additional attempts were made for the preparation of cubic perovskite-type tungsten bronzes of composition $Na_{0.6}(W^{6+}_{0.4}W^{5+}_{0.6-y}Ta^{5+}_{y})O_3$ (y = 0.00, 0.05, 0.10, 0.15, 0.20, 0.25, 0.30, 0.35, 0.40, 0.45, 0.50, 0.55 and 0.60) by conventional solid state synthesis method using Na_2WO_4, WO_3, WO_2, and Ta_2O_5 according to the chemical equation (2.5). Stoichiometric amounts of the starting materials were mixed in an agate mortar and transferred into a dried quartz tube. The internal air pressure of the reaction tubes was reduced to 10^{-7} MPa. The tubes were sealed and heated in a muffle furnace at 973 K for 7 days. Thereafter, the samples were quenched in water to room-temperature.

$$x/2\ Na_2WO_4 + (1-x-y/2)\ WO_3 + ½(x-y)\ WO_2 + y/2\ Ta_2O_5 = Na_x(W^{6+}_{1-x}W^{5+}_{x-y}Ta^{5+}_{y})O_3 \quad (2.5)$$

2.2. Analytical methods

A number of available analytical methods (mainly diffraction and spectroscopic techniques) were used for checking the purity of the products, crystallinity and homogeneity of these materials, confirmation of their crystal structures and structure-property relationships. Details of the procedures are described in the following parts.

2.2.1. Single crystal X-ray diffraction

Diffraction data were collected on a STOE IPDS1 single crystal diffractometer using graphite monochromator and Mo Kα radiation (λ = 71.073 pm) at room-temperature. A blue colored single crystal (approx. 20 μm sizes) of $Li_{0.4}WO_3$ sample was mounted on a glass fiber fixed on a metal pin. Details of data collection procedure and crystal structure are summarized in Table 2.3. The absorption was numerically corrected using the software X-Shape (STOE, Darmstadt, Germany). The structure was solved using the Patterson method to locate heavy-atoms [87] and refined by full-matrix least-squares method [88], minimizing the function $\Sigma w(|F_o|-|F_c|)^2$. Lithium atoms were placed on both the 2*a* and 6*b* sites. Refining the occupancy parameters of both sites with displacement parameters fixed at reliable values ($0.05 \cdot 10^4$ pm^2)

lithium was found only sitting on the 6*b* position (within one estimated standard deviation). In the final refinement cycles tungsten and oxygen were refined with anisotropic displacement parameters. The resulting structural parameters are given in Table 3.4, and selected interatomic distances are given in Table 3.5.

Table 2.3. Crystal data and structure refinement of $Li_{0.4}(W^{6+}_{0.6}W^{5+}_{0.4})O_3$ obtained from single crystal X-ray diffraction data.

Empirical formula	$Li_{0.4}WO_3$
Relative molar mass	234.62
Crystal system	Cubic
Space group	$Im\bar{3}$
Unit cell dimension /pm	a = 746.44(9)
Volume /10^6 pm^3	415.90(9)
Formula units /cell	Z = 8
Temperature /K	293(2)
Crystal density /gcm^{-3}	7.63
Absorption coefficient /mm^{-1}	55.2
F(000)	809
Crystal dimension /μm	20 x 20 x 20
Theta range Mo Kα	3.86° – 29.95º
Reflection range	-10 ≤ h, k, l ≤ 10
Reflections collected /unique	4532 /129
Merging residual	R_i = 0.0365
Refinement method /Program	Full-matrix least-squares on F^2/Shelx
Data /parameters	129 /12
Goodness-of-fit	1.110
Final Residuals [I > 2σ(I)] /%,	R_1 = 3.65
Weighted Residuals /%	wR_1 = 12.12

2.2.2. Powder X-ray diffraction

The X-ray powder diffraction data of $Li_x(W^{6+}_{1-x}W^{5+}_x)O_3$ bronzes were collected on a Bruker D8 Advance powder diffractometer equipped with a germanium (*111*) monochromator and Cu Kα_1 radiation (λ = 154.0596 pm). Data were recorded from 2θ range of 10º to 120º with a step width of 0.02º using the Debye-Scherrer geometry with glass capillaries of 0.3 mm outer diameter at ambient conditions. The X-ray powder diffraction data for all other samples were collected on a Panalytical MPD powder diffractometer (Panalytical, Almelo, Nederland) using the Bragg-Brentano geometry. The instrument was equipped with a secondary Ni filter, Cu K$\alpha_{1,2}$ (λ_1 = 154.0596 pm, λ_2 = 154.4414 pm) radiation, and an 'X' Celerator multi-strip detector. Data were collected at ambient conditions from 2θ range of 10° to 90° with a step width of 0.0167° /step and a collection time of 50 s /step. X-ray powder diffraction data of selected samples of $K_{0.3}(W^{6+}_{0.7}W^{5+}_{0.3-y}V^{5+}_y)O_3$ and $K_{0.3}(W^{6+}_{0.7}W^{5+}_{0.3-y}Ta^{5+}_{y/2}V^{5+}_{y/2})O_3$ series were collected on a StadiP powder diffractometer equipped with a germanium (*111*) monochromator and Cu Kα_1 radiation (λ = 154.0596 pm). Diffraction data were recorded using the Debye-Scherrer geometry putting the samples in glass capillaries of 0.2 mm outer diameter. Low-temperature powder X-ray diffraction data of $Li_{0.1}(W^{6+}_{0.9}W^{5+}_{0.1})O_3$, $Li_{0.4}(W^{6+}_{0.6}W^{5+}_{0.4})O_3$ and $K_{0.3}(W^{6+}_{0.7}W^{5+}_{0.3})O_3$ bronzes were collected on a Rigaku powder diffractometer using the Debye-Scherrer geometry. Samples were filled into glass capillaries of 0.2 mm outer diameter. Data were recorded from 100 K to 300 K with 15 K steps and 2θ range of 5° to 90° with a step width of 0.02°. Temperature-dependent X-ray powder diffraction data of $Li_{0.1}(W^{6+}_{0.9}W^{5+}_{0.1})O_3$ and $Li_{0.4}(W^{6+}_{0.6}W^{5+}_{0.4})O_3$ bronzes were also collected on a Panalytical MPD powder diffractometer with an attached Anton Paar HTK1200N heating chamber. Samples were prepared in a flat corundum sample holder using acetone to submerge the fine powder producing small evaporation channels which served for additional space for the thermal expansion of the compound. Measurements were carried out from 300 K to 780 K with 10 K steps and 2θ range of 10° to 110° with a step size of 0.0167° and a 40 s /step total data collection time. Powder X-ray data Rietveld refinements were carried out using "Diffrac^{Plus} Topas 4.2" software (Bruker AXS GmbH, Karlsruhe). To describe the X-ray diffraction profile the fundamental parameter approach was applied in the Rietveld refinements. For each diffractometer configuration, the corresponding fundamental parameters were fitted to powder data of standard LaB_6. During the refinements, general

parameters such as scale factors, background parameters (Chebychev polynomial) and average crystallite size were optimized. Additionally, the cell parameters, atomic coordinates and isotropic atomic displacement parameters were refined.

2.2.3. Neutron powder diffraction

Room-temperature neutron powder diffraction data of $Li_{0.4}(W^{6+}_{0.6}W^{5+}_{0.4})O_3$ bronze samples were recorded using the high-resolution neutron powder diffractometer E9 of the Berlin Neutron Scattering Center (BENSC) at Helmhotz-Zentrum Berlin (HZB). Neutron beam with a constant wavelength of 179.82(1) pm and Ge (*511*) monochromator was used. The sample was loaded in a 6 mm outer diameter vanadium container. The angular range of the detector was $-9.354 \leq 2\theta \leq 141.771$. The data were recorded in the range of $0.0185 \leq 2\theta \leq 141.7685$. The obtained diffraction pattern was analyzed by GSAS program [89] using the recorded diffraction data in the range of $15 \leq 2\theta \leq 135$. The wavelength of the neutron beam was refined using the cell parameters (fixed) obtained from powder X-ray diffraction data. Then the cell parameter was refined by fixing the wavelength. The background was refined in every cycle. Simultaneous refinement of lithium occupancy and isotropic displacement parameter shifted the convergence to higher *R*-values. Therefore the lithium occupancy was set to the nominal composition and the isotropic displacement parameter was refined. Afterwards, lithium occupancy was refined by fixing the displacement parameter. Finally the lithium displacement parameter was refined by fixing the occupancy. Detailed results of the crystal structure are summarized in Table 3.6. The resulting structural parameters are given in Table 3.7, and selected interatomic distances in Table 3.8.

Temperature-dependent neutron powder diffraction data (NPD) of $Li_{0.1}(W^{6+}_{0.9}W^{5+}_{0.1})O_3$ and $Li_{0.4}(W^{6+}_{0.6}W^{5+}_{0.4})O_3$ series were recorded using time-of-flight (TOF) neutron flux of POWGEN diffractometer at the Spallation Neutron Source (SNS) (OAK RIDGE NATIONAL LABORATORY, USA). About 3 g of the powder sample was loaded into a thin-walled vanadium sample container. The container filled with the sample was placed in an ILL-type low-pressure ($\sim 2.7 \times 10^{-9}$ MPa) furnace and heated from 380 K to 780 K with a ramp of 25 K each step. The data were collected using a center wavelength of 133.3 pm. Rietveld refinement of the temperature-dependent NPD data were also performed using GSAS software [89].

2.2.4. Scanning electron microscopy and energy dispersive X-ray spectroscopy, SEM/EDX

The scanning electron microscopy (SEM) micrographs and the energy dispersive X-ray spectroscopy (EDX) data were recorded using JMS-6510 instrument equipped with X-Flash detector 410-M operated at an accelerating voltage of 20 kV. The SEM specimen was prepared by mounting a small amount of the sample on an aluminum stub with a conducting carbon tape. The elemental analysis offered the constituent metals ratio in atom-% in the compound. The whole spectrum was used for the quantification of the component elements. The atom-% of the metal also gave approximate compositions of the synthesized products.

2.2.5. Raman spectroscopy

Raman spectra were collected using a pressed pellet of 5 mm diameter. The spectra were recorded on a Horiba LabRam Aramis spectrometer equipped with a laser of 532 nm, 633 nm and 785 nm wavelengths. Data were collected between 80 cm^{-1} to 1200 cm^{-1} Raman shift with a spectral resolution of approx. 2 cm^{-1} using a grating of 1800 groves /mm. Temperature-dependent Raman data were collected from 78 K to room-temperature. For the low-temperature measurements, liquid-nitrogen was passed through the sample-chamber attached with a Linkam temperature control stage. The computer-controlled software was used to set and to read the temperature around the sample-environment. The spectra were baseline corrected and peak fitting were performed using the LabSpec version 5 software packages. Component analysis was carried out using Lorentz-Gauss functions.

2.2.6. Infrared spectroscopy

The Fourier transform infrared (FTIR) absorption spectra were recorded using BRUKER IFS66v spectrometer in the mid-infrared (MIR, 370 cm^{-1} – 4000 cm^{-1}) region. The spectra were collected using the standard KBr method (1 mg sample diluted into 200 mg KBr), obtained from 64 scans with a spectral resolution of approximately 2 cm^{-1}. Finely ground sample was mixed together with KBr and pressed into pellet of 13 mm diameter for measuring transmission MIR spectra. The spectra are shown in absorbance units, Abs = $\log(I_o/I)$, where I_o and I are transmitted intensities through the reference KBr pellet and sample pellet diluted with KBr, respectively.

RESULTS AND DISCUSSION

3.1. Composition (x) dependent $Li_x(W^{6+}_{1-x}W^{5+}_x)O_3$ bronzes

Samples synthesized using different nominal compositions of lithium show gradual change of their colors. The low-lithium content (x = 0.1) bronze is light-blue whereas high-lithium (x = 0.2, 0.3, 0.4, 0.5 and 0.6) content materials are dark-blue colored. The color of the samples becomes deeper with successive increase of Li concentration. X-ray powder diffraction data of polycrystalline $Li_x(W^{6+}_{1-x}W^{5+}_x)O_3$ (x = 0.1, 0.2, 0.3, 0.4, 0.5, and 0.6) bronzes as shown in Figure 3.1 were recorded and Rietveld refinements were performed for their crystal structures determination. Rietveld refinements of powder X-ray diffraction data offered the structural details and the relative phase fractions of these bronzes. The observed results are given in Table 3.1. The sample of nominal composition x = 0.1 ($Li_{0.1}WO_3$) shows pure perovskite-type tungsten bronze structure in the orthorhombic symmetry (PTB_O), whereas a mixture of two phase (PTB_O and PTB_C, PTB_C ≡ cubic perovskite-type tungsten bronze) products are observed for x = 0.2 and 0.3. Pure PTB_C phases are found for lithium composition of x = 0.4, 0.5 and 0.6. Details of the crystal structure of the PTB_O and the PTB_C phases are described in the next part. The system transferred into high-symmetry phase from low-symmetry WO_3 structure due to the incorporation of lithium into the tetragonal channels of the WO_3-matrix. Low-temperature phase of WO_3 is triclinic whereas room-temperature phase is monoclinic [4]. Lithium is incorporated into the tunnels of WO_3 resulted high-symmetry orthorhombic or cubic phase at high-temperature (973 K) and low-pressure (10^{-7} MPa) conditions. These higher symmetry $Li_x(W^{6+}_{1-x}W^{5+}_x)O_3$ bronze phases are stable at room-temperature and low-pressure conditions. Whereas, applying high-temperature the parent WO_3 can be converted into the high-symmetry phases such as orthorhombic or tetragonal phase [4]. High-symmetry phases of WO_3 are unstable at ambient conditions. The lithium concentration plays the main role for the formation of high-symmetry $Li_x(W^{6+}_{1-x}W^{5+}_x)O_3$ bronzes. In the same crystal-structure type of $Li_x(W^{6+}_{1-x}W^{5+}_x)O_3$ (PTB_C) bronzes, that is in the cubic phase of different lithium content, the lattice parameter gradually decreased when more lithium is incorporated into the WO_3-network. Such trend for lattice parameter changes of the lithium tungsten bronzes are distinct from that of the others metal tungsten bronzes [90], though all these bronzes have cubic symmetry. In case of tungsten bronzes of other elements (e.g. Na, Gd, U

etc.) crystallized in the cubic structure show opposite behavior of their metric parameters change with respect to the concentration of incorporated metal cations.

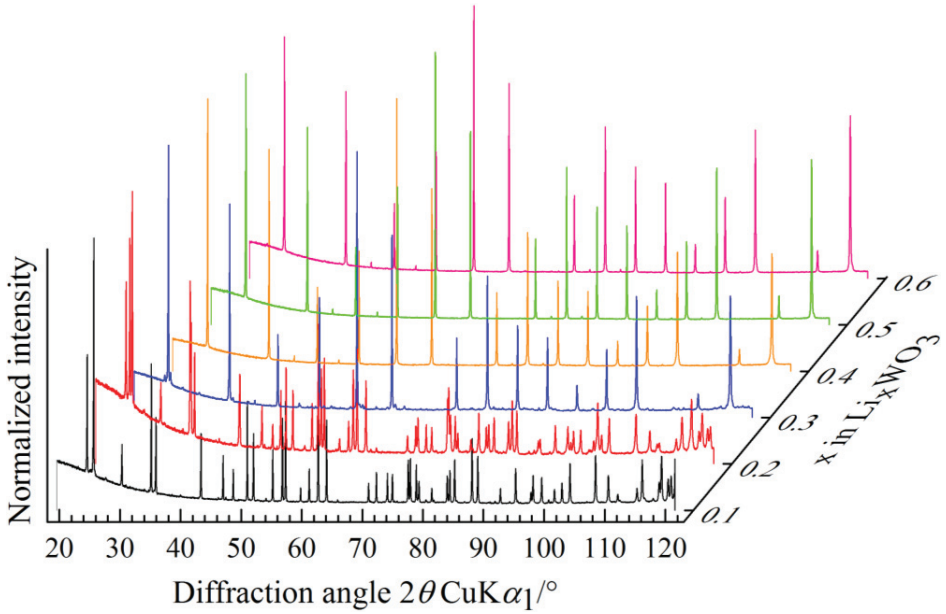

Figure 3.1. Powder X-ray diffraction patterns of $Li_x(W^{6+}_{1-x}W^{5+}_x)O_3$ bronzes, where x = 0.1 (pure PTB_O); x = 0.2 and 0.3 (mixed phases of PTB_C and PTB_O); x = 0.4, 0.5, and 0.6 (pure PTB_C).

Table 3.1. Rietveld refinements results obtained from powder X-ray diffraction data of $Li_x(W^{6+}_{1-x}W^{5+}_x)O_3$ series.

x	Crystal structure	Space group	Phase fractions /wt-%	Lattice parameter /pm		
				a	*b*	*c*
0.1	PTB_O	*Pcnb*	100	735.76(1)	735.52(1)	769.46(0)
0.2	PTB_O	*Pcnb*	67.4(3)	735.27(2)	735.05(2)	767.08(5)
	PTB_C	$Im\bar{3}$	32.6(3)	747.30(4)	-	-
0.3	PTB_O	*Pcnb*	11.3(4)	736.41(6)	735.17(2)	766.78(5)
	PTB_C	$Im\bar{3}$	88.7(4)	746.98(3)	-	-
0.4	PTB_C	$Im\bar{3}$	100	745.25(6)	-	-
0.5	PTB_C	$Im\bar{3}$	100	744.35(3)	-	-
0.6	PTB_C	$Im\bar{3}$	100	744.26(2)	-	-

It is assumed that in case of others metal tungsten bronzes the metal atoms donate their outer shell electrons to W^{6+} giving rise of W^{5+} cations, whereas the electrons donated by the Li

atoms behave as free electron-gas [76]. It may well possible that the electrons provided by Li are delocalized into the tetragonal channels of WO_3 rather than being localized over tungsten.

3.1.1. $Li_{0.1}(W^{6+}_{0.9}W^{5+}_{0.1})O_3$ bronze

The lithium tungsten bronze with a nominal composition of $Li_{0.1}WO_3$ crystallized in the pure PTB_O structure, confirmed by X-ray powder diffraction data. Figure 3.2 shows the powder X-ray diffraction pattern along with Rietveld refinement fit using the space group *Pcnb*. This phase is comparable to the high-temperature phase of host-WO_3 [91]. The observed lattice parameters of PTB_O structure are dissimilar from that of the high-temperature structure of WO_3. The details of the refined structural parameters of $Li_{0.1}(W^{6+}_{0.9}W^{5+}_{0.1})O_3$ bronze are given in Table 3.2, and selected interatomic distances and angle are given in Table 3.3.

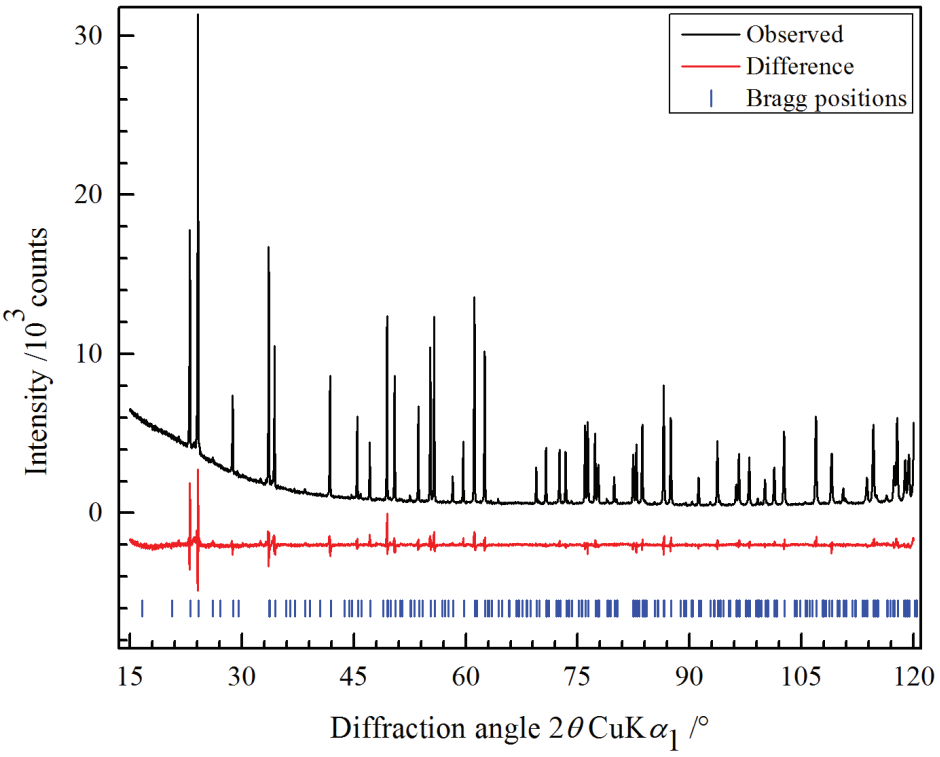

Figure 3.2. Rietveld refinement plot of powder X-ray diffraction data of $Li_{0.1}(W^{6+}_{0.9}W^{5+}_{0.1})O_3$ bronze.

Several earlier reports [46, 47, 92, 93], describing that the $Li_{0.1}(W^{6+}_{0.9}W^{5+}_{0.1})O_3$ bronze crystallizes in the space group *P*4/*nmm* or *P*4/*ncc*, show conflicting results compared to this observation. However, details of the crystallographic information are not available from

powder X-ray diffraction data, especially position of Li and its content, in the earlier reports. In this study, the details of structural parameters were determined from room-temperature X-ray and high-temperature neutron powder diffraction data. The characteristics reflections of *Pcnb* space group are discernable in the diffraction profiles which are forbidden for the space group *P*4/*nmm*. Temperature-dependent X-ray and neutron powder diffraction data as well as Raman spectra were also studied as a complementary method for confirming the space group.

Table 3.2. Details of the crystal structure of $Li_{0.1}(W^{6+}_{0.9}W^{5+}_{0.1})O_3$ bronze. The atomic displacement of Li is chosen as an arbitrary constant value of 1.0.

Space group: *Pcnb*, *a* = 735.74(1) pm, *b* = 735.53(1) pm, *c* = 769.46(1) pm, *Z* = 8, R_{wp} = 5.6 %						
Atom	Wyckoff	*x*	*y*	*z*	Occupancy	B_{eq} /10^4 pm^2
W	8*d*	0.24288(16)	0.00365(26)	0.28455(7)	1	0.16(2)
O1	8*d*	0.0010(17)	0.0202(37)	0.2016(25)	1	0.45(2)[a]
O2	8*d*	0.2044(31)	0.2501(28)	0.2574(37)	1	0.45[a]
O3	8*d*	0.2926(27)	0.0276(32)	0.0068(10)	1	0.45[a]
Li	4*c*	½	¼	0.00(13)	0.21(9)	1.0

[a] Values were constrained to each other during the refinements.

Table 3.3. Selected interatomic distances and angles of $Li_{0.1}(W^{6+}_{0.9}W^{5+}_{0.1})O_3$ bronze obtained from powder X-ray diffraction data Rietveld refinement.

Atoms	Count	Distances /pm	Atoms	Distances /pm	W–O–W/°
Li–O1a	2x	285(8)	W–O1a	189(1)	155.40(74)
Li–O1b	2x	304(8)	W–O1b	191(1)	
Li–O2a	2x	240(8)	W–O2a	185(2)	159(1)
Li–O2b	2x	294(7)	W–O2b	193(2)	
Li–O3a	2x	224(3)	W–O3a	173.9(9)	158.87(45)
Li–O3b	2x	255(3)	W–O3b	217.5(9)	

In the structure, the tungsten is displaced from the center of the WO_6 octahedron, having six different W–O bond distances. There is about 10º inter-octahedral tilting among the WO_6

octahedral network. Lithium is distributed into the channels within a twelve-fold coordination environment. The shortest Li–O distance is 224(3) pm which is much larger than usual Li–O bond distance. It indicates lithium is weakly bonded with the oxygen atoms into the tetragonal channels formed by the corner-shared distorted WO_6 octahedral units.

3.1.2. $Li_{0.4}(W^{6+}_{0.6}W^{5+}_{0.4})O_3$ bronze

The crystal structure of $Li_{0.4}(W^{6+}_{0.6}W^{5+}_{0.4})O_3$ bronze is confirmed by single crystal and powder X-ray diffraction, and neutron powder diffraction. The collected single-crystal data of $Li_{0.4}(W^{6+}_{0.6}W^{5+}_{0.4})O_3$ bronze were refined in the space group $Im\bar{3}$. Details of data collection procedure and crystal structure are summarized in Table 2.3 and 3.4, respectively. Resulting selected bond distances and angles are given in Table 3.5. The observed lattice parameter (746.44(9) pm) slightly deviates from the values calculated from X-ray as well as neutron powder diffraction data [50, 94, 95], however, it agrees well with the theoretical value of *a* [pm] = 2 • (378.5 – 13.4 • x) pm = 746.28 pm proposed for cubic Li_xWO_3 bronzes [90]. The initial nominal composition $Li_{0.4}WO_3$, corresponding to a lithium occupancy factor of 0.53, fits to the refined value 0.49(12) and a composition of $Li_{0.37(12)}WO_3$. The discrepancy with a high uncertainty may arise due to lithium distribution considered only at 6*b* position during the refinement leaving the 2*a* site completely empty or simply from the rather low scattering cross-section of lithium compared to tungsten and oxygen and the resulting error.

Table 3.4. Atomic coordinates and anisotropic displacement parameters of $Li_{0.4}(W^{6+}_{0.6}W^{5+}_{0.4})O_3$ bronze obtained from single crystal X-ray diffraction data.

Atom	Wyckoff	Site symmetry	Occupancy	*x*	*y*	*z*	U_{iso} /10^4 • pm^2
Li	6*b*	*mmm*	0.49(12)	½	½	0	0.014(17)
W	8*c*	.-3.	1	¼	¼	¼	
O	24*g*	*m*..	1	0	0.2088(14)	0.2930(13)	
Anisotropic displacement parameters x10^4 /pm^2							
Atom	U_{11}	U_{22}	U_{33}	U_{12}	U_{13}	U_{23}	U_{eq} /10^4 • pm^2
W	0.014(1)	0.014(1)	0.014(1)	0	0	0	0.014(1)
O	0.004(4)	0.086(8)	0.075(8)	0	0	-0.015(2)	0.055(5)

Table 3.5. Selected interatomic distances and angles of $Li_{0.4}(W^{6+}_{0.6}W^{5+}_{0.4})O_3$ bronze obtained from single crystal X-ray diffraction data.

Atoms	Count	Distances /pm	W–O–W /°
Li–O	4x	219.5(7)	
Li–O	4x	267(1)	
W–O	6x	192(1)	153.20(1)

A single crystal, picked from the same batch and left at atmospheric condition for about one year, showed an almost similar lattice parameter (746.95(1) pm), however with almost three-times increased internal *R*-values of 10.24 %. Of important notes, the one-year exposed sample showed clear hints of slightly smearing the reflections, which may be due to presence of intimately mixed up cubic phases. This observation is consistent with the results obtained by Rüscher et al. [47] using laser ablation inductively coupled plasma optical emission on a polished surface of single crystals. For a nominal compositions of x = 0.30 and 0.35 bright and dark areas were identified corresponding to boundary compositions of the tetragonal (x ~ 0.18) and cubic (x ~ 0.38) phase. Assuming that both of these samples preserved the nominal composition, lithium-enriched cubic and lithium-deficient tetragonal phases were produced where none contains the initial composition.

Polycrystalline powder sample of $Li_{0.4}(W^{6+}_{0.6}W^{5+}_{0.4})O_3$ bronze produced at 973 K for 168 h using a pressure of 10^{-7} MPa resulted in pure body-centered cubic perovskite-type tungsten bronze (PTB_{CI}) as confirmed by X-ray and neutron powder diffraction data Rietveld refinement. Rietveld refinement plot for pure PTB_{CI} phase of $Li_{0.4}(W^{6+}_{0.6}W^{5+}_{0.4})O_3$ is shown in Figure 3.3. Details of the crystal structure are summarized in Table 3.6. The resulting structural parameters are given in Table 3.7, and selected interatomic distances are given in Table 3.8. Using pressures greater than 10^{-7} MPa always led to a mixed phase of PTB_{CI} and primitive cubic perovskite-type tungsten bronze (PTB_{CP}). Figure 3.4 shows the relation between the phase fraction of PTB_{CP} and the applied pressure in the quartz tube for synthesis. Even using different reaction temperatures (973 K – 1073 K) and time (24 h to 168 h) at 10^{-7} MPa gave the same results for the formation of PTB_{CI} phase. Although Dey et al. [46] observed the PTB_{CI} phase, identified as weak reflections, they took during their refinements only the PTB_{CP} into account.

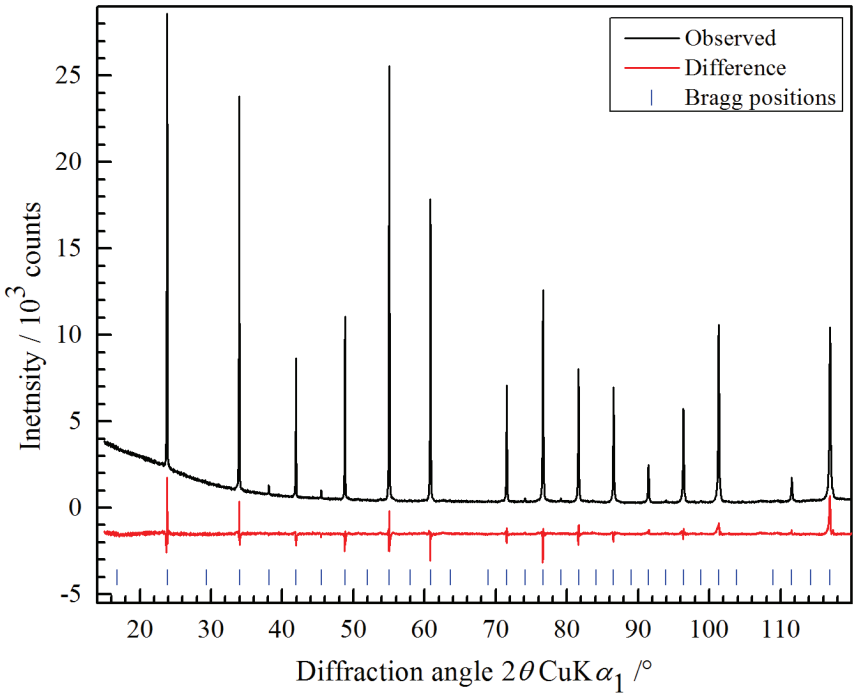

Figure 3.3. Rietveld refinement plot of powder X-ray diffraction data of $Li_{0.4}(W^{6+}_{0.6}W^{5+}_{0.4})O_3$ bronze.

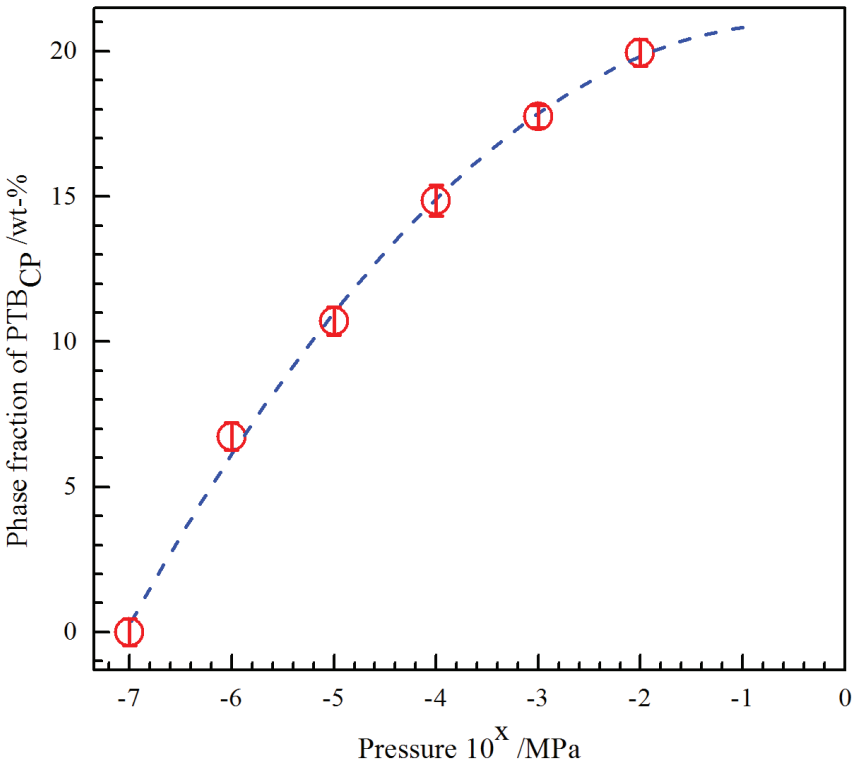

Figure 3.4. Synthesis-pressure dependent phase fraction of the coexisting PTB_{CP} (*Pm$\bar{3}$m)* phase during the formation of PTB_{CI} (*Im$\bar{3}$*) $Li_{0.4}(W^{6+}_{0.6}W^{5+}_{0.4})O_3$ bronzes. This figure is reprinted from ref. [95].

Theoretically the first superstructure reflection *301* intensity is about 1 % of the high intense *002* reflection; it may be well possible that they did not consider PBT_{CI} as the major component due to the low intensity of the superstructure reflections from the X-ray powder diffraction data. Notably, Dey et al. [46] produced $Li_{0.4}WO_4$ bronze using a pressure of $1.334 \cdot 10^{-6}$ MPa (10^{-2} torr). Our pressure-dependent data analysis estimates that they might produce about 7(1) wt-% PBT_{CP} assuming PBT_{CI} to be the major component of the products.

The ambient conditions neutron powder diffraction data, collected on samples prepared with an air pressure of 10^{-7} MPa, were refined against the structure of pure PTB_{CI}. The resulting Rietveld plot is shown in Figure 3.5. The characteristic reflections of the body centered phase are clearly discernable in the pattern. Details of the crystal structure are summarized in Table 3.6. The resulting structural parameters are given in Table 3.7, and the selected interatomic distances and angles are given in Table 3.8. The neutron powered diffraction data and complementary Raman spectrum of this sample clearly confirm the space group $Im\bar{3}$.

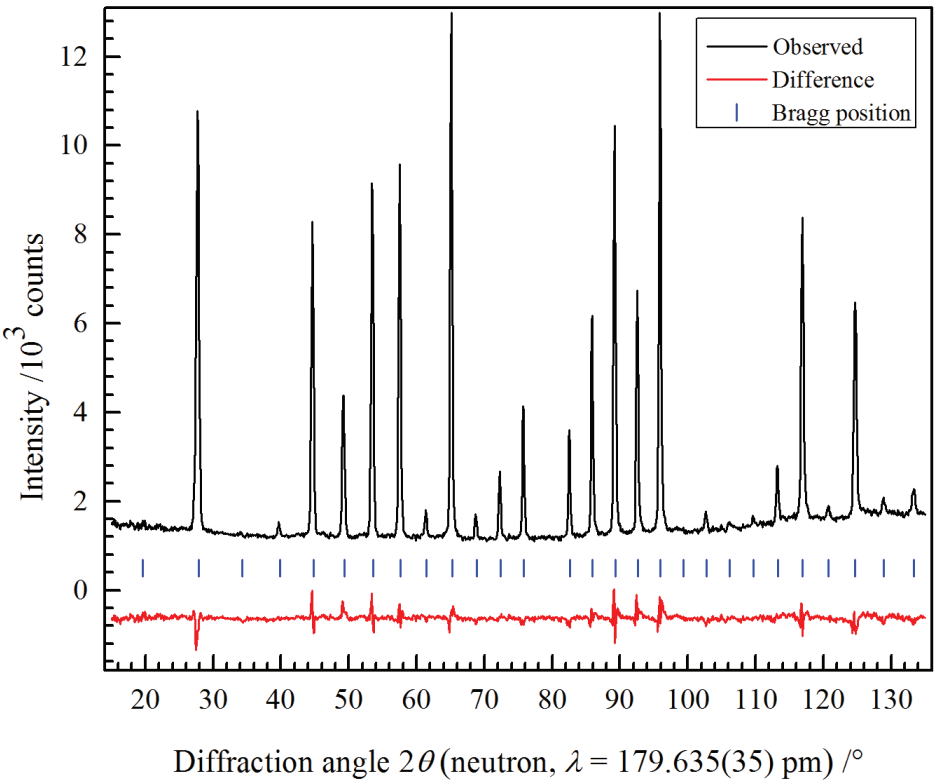

Figure 3.5. Rietveld refinement plot of room-temperature neutron powder diffraction data of $Li_{0.4}(W^{6+}_{0.6}W^{5+}_{0.4})O_3$ bronze ($Im\bar{3}$). This figure is reprinted from ref. [95].

Crystal structure results from a freshly prepared sample and that of a sample left in vacuum for six weeks in a quartz tube are similar. The calculated geometric parameters are very close to the reported ones [94]. It clearly demonstrates that if $Li_{0.4}(W^{6+}_{0.6}W^{5+}_{0.4})O_3$ bronze is stored at vacuum condition, the PTB_{CI} phase does not change in time. Simultaneous occupancy refinement both in the 2*a* and 6*b* sites showed higher *R*-values with unphysical occupancy parameters. Thus the occupancy of lithium was refined placing only in the 6*b* site with better convergence indices. This finding unambiguously supports the lithium occupancy of 0.53(1).

Table 3.6. Experimental data of $Li_{0.4}(W^{6+}_{0.6}W^{5+}_{0.4})O_3$ from X-ray and Neutron powder diffraction.

	X-ray	neutron
Space group	$Im\bar{3}$	
a /pm	744.906(3)	744.906(15)
V /10^6 pm^3	413.337(5)	413.337(24)
Formula units /cell	$Z = 8$	
Calculated density /gcm^{-3}	7.52(1)	7.54(1)
Wavelength /pm	154.0596(1)	179.635(35)
2θ-range /°	$10 < 2\theta < 120$	$15 < 2\theta < 135$
No. of data points	5567	1891
Rietveld program	Topas 4.2	GSAS
Weighted residual (profile) /%	$R_{WP} = 6.51$	$R_{WP} = 3.68$
Residual (profile) /%	$R_P = 4.23$	$R_P = 2.83$
Residual (intensity) /%	$R_B = 5.72$	$R_B = 1.23$

Table 3.7. Atomic coordinates and isotropic displacement parameters of $Li_{0.4}(W^{6+}_{0.6}W^{5+}_{0.4})O_3$ bronze obtained from neutron and X-ray (*in italics*) powder diffraction data.

Atom	Wyckoff site	Occupancy	*x*	*y*	*z*	U_{iso} /10^4 • pm^2
Li	6b	0.53(1)[a] *0.533*[b]	½	½	0	0.039(3)[a] *0.038(17)*
W	8*c*	1	¼	¼	¼	0.0069(4) *0.003(2)*
O	24*g*	1	0	0.2052(2) *0.2090(57)*	0.2902(2) *0.2934(55)*	0.010(2) *0.011(2)*

[a] Simultaneous refinement were not possible, [b] fixed to the nominal composition.

Table 3.8. Selected interatomic distances and angles of $Li_{0.4}(W^{6+}_{0.6}W^{5+}_{0.4})O_3$ bronze obtained from neutron and X-ray (*in italics*) powder diffraction data.

Atoms	Count	Distances /pm	W–O–W /°
Li–O	4x	218.8(2) *219(3)*	
Li–O	4x	269.8(1) *266(4)*	
W–O	6x	191.8(1) *192(1)*	152.92(7) *153.13(1)*

3.2. Phase transformation of $Li_{0.4}(W^{6+}_{0.6}W^{5+}_{0.4})O_3$ bronze

Samples prepared under the same conditions showed different behaviors keeping them, after the first opening of the synthesis tube, under open or closed conditions. In this respect open conditions means that the samples were kept in (covered) glass bottles (vial) in air at ambient conditions whereas in closed conditions the samples were sealed in glass capillaries by fusing. Pure PTB_{CI} ($Im\bar{3}$) samples (prepared at 10^{-7} MPa, 973 K, 168 h) transformed into the tetragonal phases (PTB_T, *P*4/*nmm*) at open storage condition as shown in Figure 3.6.

For example, a pure PTB_{CI} powder sample transformed into PTB_T (a = 520.11(2), c = 383.58(2) pm) when kept at ambient conditions into a glass vial. The transformation behavior could be fitted using the equation (3.1):

$$C_t = C_0 + C\, t^{\,n} \tag{3.1}$$

where C_t is the concentration of the respective phase after time t (day), C_0 is the concentration at the beginning and, C and n are fitting values. For the transformation of the body-centered phase (PTB_{CI}) C_0 = 100 and C and n were refined to -6.6017(5) and 0.50(1), respectively. For the calculation of the PTB_T increase C_0 becomes 0 and C changes its sign. For the samples containing mixed phases after the synthesis (prepared above 10^{-7} MPa, 973 K, 168 h) a linear change of the phase fraction could be observed (Figure 3.7). In these samples PTB_{CI} transformed into PTB_{CP} in closed conditions and to PTB_T in open conditions. For the latter case any amount of PTB_{CP} observed after the synthesis in the sample stays more or less constant (changed from 8(5) wt-% to 7(5) wt-% in 200 days). The increase of the tetragonal phase fraction could be fitted using the equation (3.1) setting n = 1 (linear dependency). The slope was fitted to C = 0.193(2) for closed conditions and C = 0.187(2) for open conditions, which is very close to each other. For the latter case C_0 was calculated to be 7.90(3) wt-%.

Rietveld refinements plot of coexisting PTB_{CI}, PTB_{CP} and PTB_T phases is shown in Figure 3.8(a). Details of the crystal structure of PTB_{CP} and PTB_T phases are given in Table 3.9. A schematic summary of the observations is given in Figure 3.8(b).

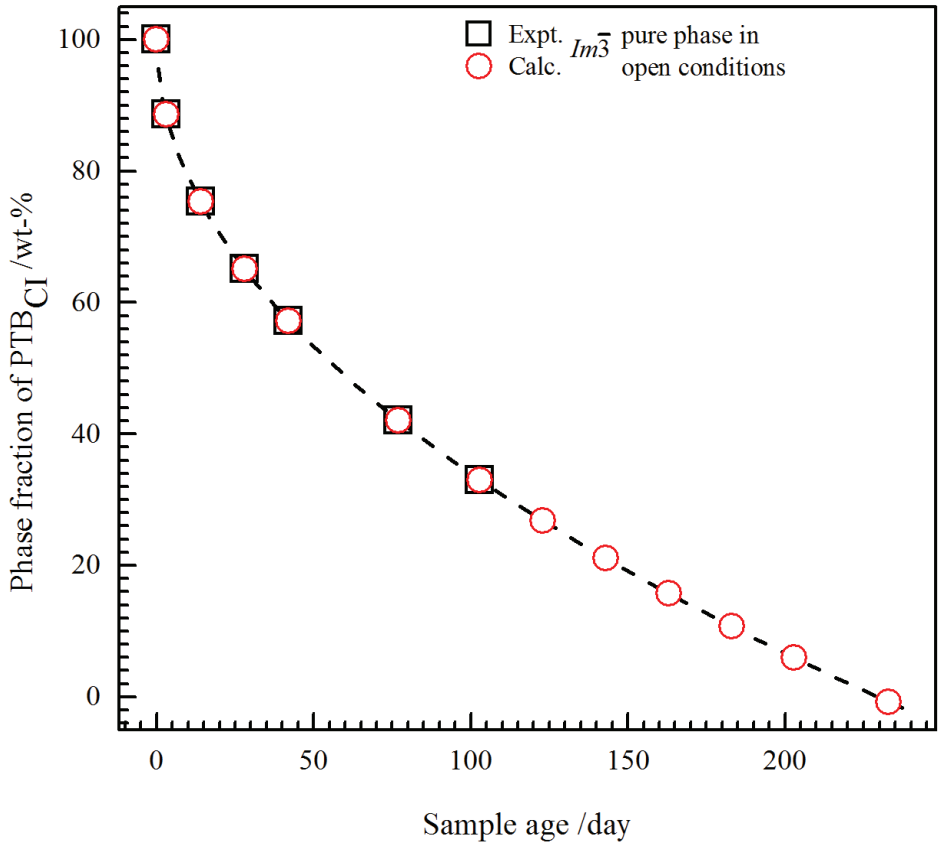

Figure 3.6. Time-dependent phase transformation behavior of $Li_{0.4}(W^{6+}_{0.6}W^{5+}_{0.4})O_3$ kept at ambient conditions. Pure $Im\bar{3}$ phase kept into open conditions with respective fit. This figure is reprinted from ref. [95].

Unlike other alkali metal tungsten bronze systems, where the electrons from A^+ cation are considered to be strongly associated with the W^{6+} giving rise of W^{5+} cations, electrons from lithium could act as free electron gas, which is then weakly associated with the whole lattice. Both magnetic susceptibility [76] and NMR [96] experiments on cubic Li_xWO_3 bronzes support Pauli-Bloch 'free electron gas' model. Whereas the cell parameter in other bronze systems increases with increasing A^+ cation concentration due to the corresponding increase of the W^{5+} cation, increasing lithium in the cubic Li_xWO_3 bronze the cell parameter decreases as a consequence as shown in Figure 3.9. Evidently, the expansion-contraction mechanism in

the lithium system is mainly occurred by the tilting of WO_6 octahedra. For example, with increasing compositional x from 0.14 (a = 753.25 pm) to 0.36 (a = 747.35 pm), the W–O bond distance remains constant (191.7 pm), however, $Li_{0.36}WO_3$ experiences a tilting of about 13.8° [50].

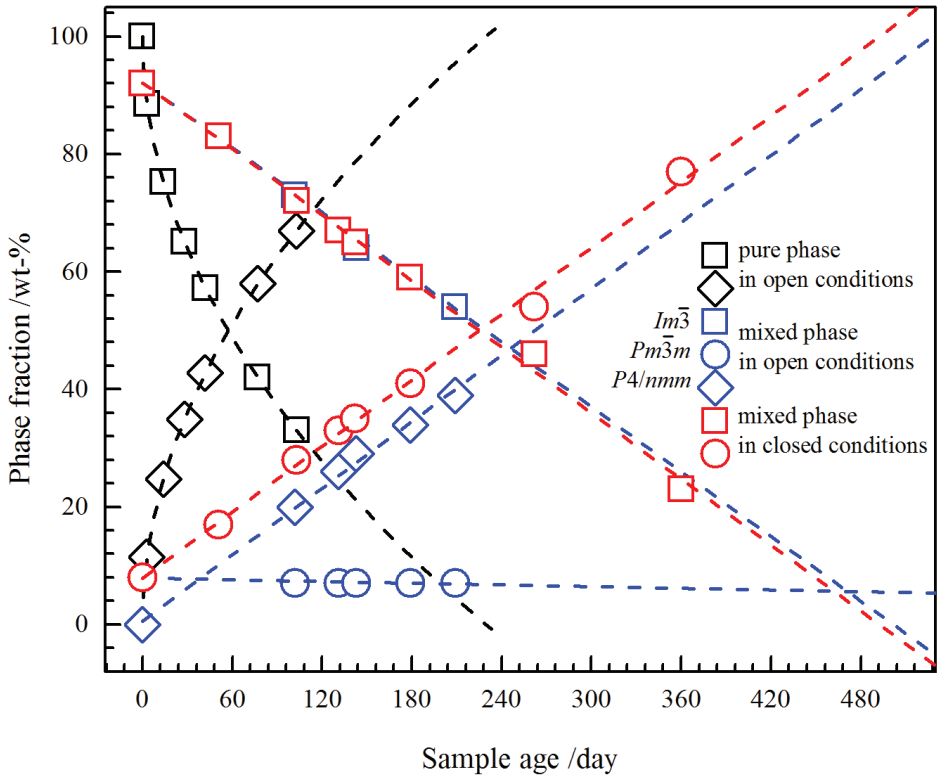

Figure 3.7. Time-dependent phase transformation behavior of $Li_{0.4}WO_3$ kept at ambient conditions. All conditions are showing changes. The symbol type and color represent the respective phases and conditions. The dotted lines are for their respective fit. This figure is reprinted from ref. [95].

In Figure 3.9 most of the available cell parameters corresponding to cubic systems belong to initial (i.e., nominal) composition. The lateral high scattering from the model line is assumed to be due either to lack of information of the refined composition (x) using in-house X-ray diffraction or to incorrect space group, or a thorough revision is required in this regards in particular for a high x-region. In phases crystallizing in other than cubic symmetry the electrons cannot be considered as free, and increasing lithium can contribute to lattice expansion. For example, in the $K_{0.24}Li_xWO_3$ hexagonal bronze, the cell parameter increases up to a saturation value [97] with increasing x. Clearly, in this observation increasing lithium

content gradually contributes to reduction of W^{6+} into W^{5+}, that is, as long as lithium is not identified as ionic form (Li^+) in the Li_xWO_3 bronze it does not likely to contribute to the expansion /contraction mechanism of the unit cell as well as to phase transitions (Figure 3.9).

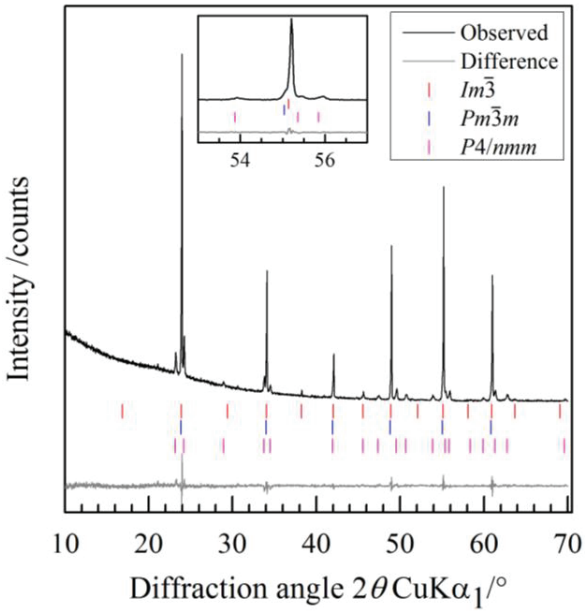

Figure 3.8(a). Rietveld refinement plot of coexisting PTB_{CI}, PTB_{CP} and PTB_T phase of aged $Li_{0.4}WO_3$ bronze sample containing mixed phases after the synthesis.

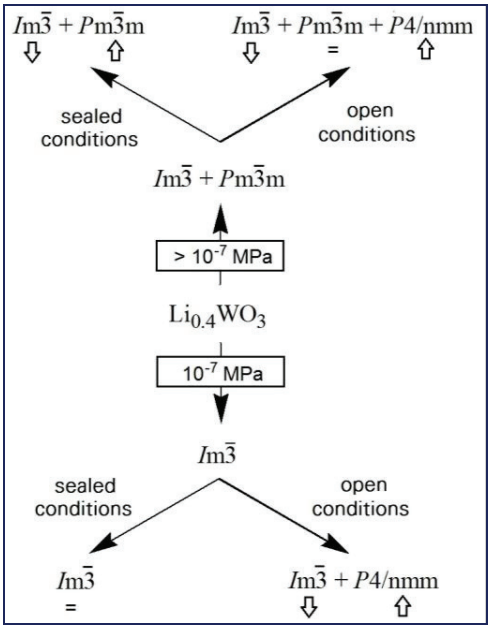

Figure 3.8(b). Schematic overview on time-dependent phase transformation behavior of $Li_{0.4}WO_3$ kept at ambient conditions. Arrows indicate decreasing (down) or increasing (up) phase fraction, (=) indicates (almost) no changes. This figure is reprinted from ref. [95].

Considering four-fold coordination of Li in the 6*b* site, the planar four-oxygen offers an aperture [½(shortest O–O distance – 2•r_o (CN, CR)] of 26.7 pm which is much smaller than the ionic radius of the Li^+ cation of 59 pm [98]. So far two kinds of diffusion pathways have been proposed in the PTB_{CI} system: 6*b* → 6*b*, and 2*a* → 6*b* → 2*a* [99]. That is, Li^+ cannot move from one 2*a* to another 2*a* site without passing through the 6*b* site. In fact, the aperture through which the diffusing atom must move is almost the same for both pathways. In the PTB_T structure the tilting of the octahedra turns into zero, resulting in internal distortion of the octahedra with two different W−O bond distances (192 pm and 186 pm).

Table 3.9. Details of the crystal structures, atomic coordinates and displacement parameters of PTB_{CP} and PTB_T phases obtained from powder X-ray diffraction data Rietveld refinements of $Li_{0.4}(W^{6+}_{0.6}W^{5+}_{0.4})O_3$. The atomic displacement of Li is chosen as an arbitrary constant value of 1.0.

Space group: $Pm\bar{3}m$, a = 372.82(3) pm, V = 51.82(1) •10^6 pm^3, R_{wp} = 5 %						
Atom	Wyckoff	x	y	z	Occupancy	B_{eq} /10^4 • pm^2
Li	1*a*	0	0	0	0.4	1.0
W	1*b*	½	½	½	1	0.25(9)
O	3*c*	½	½	0	1	0.3(2)
Space group: *P*4/*nmm*, a = 520.11(2) pm, c = 383.58(2) pm, V = 103.76(1) •10^6 pm^3, R_{wp} = 5 %						
Li	2*a*	¾	¼	0	0.4	1.0
W	2*c*	¼	¼	0.43594(94)	1	0.24(9)
O1	2*c*	¼	¼	0.9568(91)	1	0.3(1)[a]
O2	4*e*	0	0	½	1	0.3[a]

[a] Values were constrained to each other during the refinements.

Moreover, in PTB_T there is only one possible site for lithium (2*a*), and only a one dimensional channel with an aperture radius of 58 pm along the **c**-axis for lithium percolation. Since in PTB_{CI} the mobility of lithium at 2*a* is limited we assume that once lithium hops to a 2*a* site, a $2a \rightarrow 6b \rightarrow 2a$ mechanism might happen leading to $PTB_{CI} \rightarrow PTB_T$ phase transition. Because the transformation kinetics is very slow at the used temperature, consolidated evidence to validate this hypothesis seems to be tedious. However, if temperature-induced backward kinetics ($PTB_T \rightarrow PTB_{CI}$) is fast enough, temperature-dependent in-situ neutron diffraction can unravel this structural crux. Like other d^0 elements tungsten is susceptible to second-order Jahn-Teller (SOJT) distortion leading to spontaneous formation of off-centering WO_6 octahedra in the associated crystal structures [100]. With increasing lithium concentration more electrons can go into the W ($5d$-t_{2g}) conduction band. As a consequence, the energetic advantage for SOJT distortion diminishes, and the W-ions moves back to its centrosymmetric position. Since the *P*4/*nmm* possesses SOJT distortion causing one longer and one shorter W–O bonds along the **c**-axis, it is reasonable to assume that the transformed *P*4/*nmm* is a phase of low lithium concentration. Therefore the $Im\bar{3} \rightarrow P4/nmm$ phase transformation might be driven by the SOJT distortion leaving the WO_6 octahedra un-tilted. In the sealed capillary the

transformation from $Im\bar{3}$ to aristotype $Pm\bar{3}m$ takes place, where both the SOJT distortion and the WO_6 octahedral tilting are absent. This transformation can be assumed to be due to higher lithium content in the $Pm\bar{3}m$ phase as the lattice parameter of $Pm\bar{3}m$ is slightly smaller than that of parent $Im\bar{3}$ (Figure 3.9). Both these transformations support the density functional theory works on Na_xWO_3 bronzes [101].

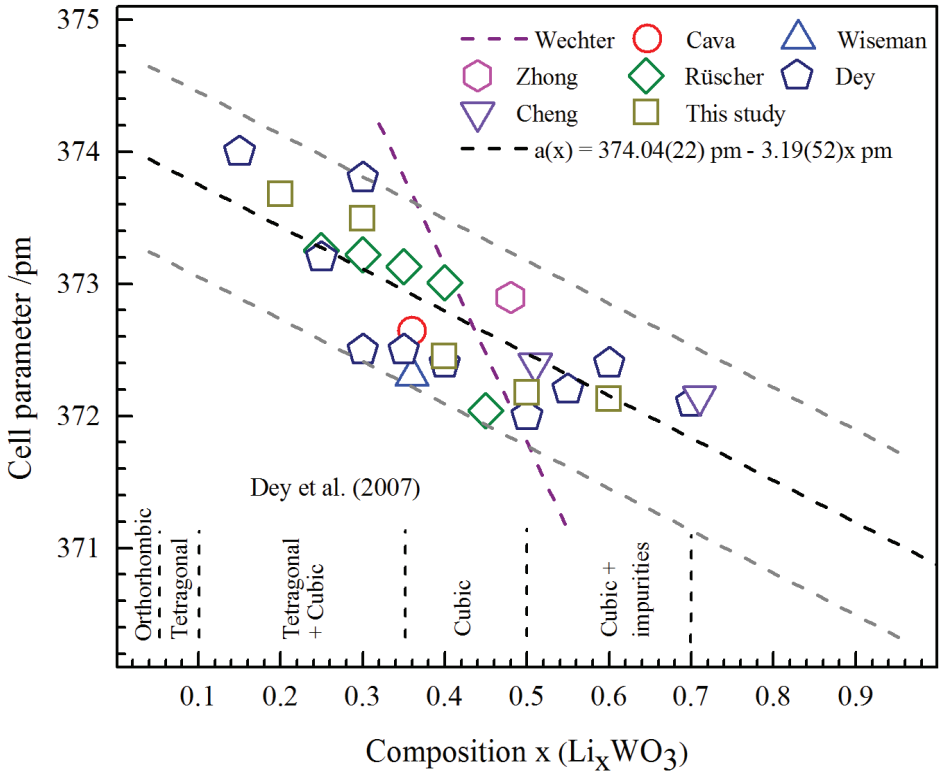

Figure 3.9. Change of cell parameter with lithium composition of cubic Li_xWO_3 bronze (including data from Cava et al. [94], Wiseman et al. [50], Zhong et al. [92], Rüscher et al. [47], Dey et al. [46], Cheng et al. [93] and from the equation given by Wechter et al. [90]). The dotted lines represent the calculated lattice parameter development and a probability range in dark and light dots, respectively. This figure is reprinted from ref. [95].

3.3. Thermal behavior of $Li_{0.1}(W^{6+}_{0.9}W^{5+}_{0.1})O_3$ bronze

Thermal expansions of $Li_{0.1}(W^{6+}_{0.9}W^{5+}_{0.1})O_3$ bronze have been studied from temperature-dependent X-ray (100 K to 400 K) and neutron (380 K to 780 K) powder diffraction data. Temperature-dependent Raman spectra were also analyzed at low-temperature region (78 K to 303 K) for studying the behaviors of different vibrational modes of this bronze material.

3.3.1. Temperature-dependent powder diffraction data investigation

The time-of-flight neutron powder diffraction (NPD) data collected at high-temperature conditions were also refined in the space group *Pcnb* same as the temperature-dependent powder X-ray diffraction (XRD) data. Rietveld refinement plot for NPD data of $Li_{0.1}(W^{6+}_{0.9}W^{5+}_{0.1})O_3$ bronze at 380 K is shown in Figure 3.10, details of the crystal structure are given in Table 3.10. The characteristic reflections of space group *Pcnb* are clearly discernable in the neutron powder diffraction data which are very weak in the powder X-ray diffraction profile. Successive trial was made for indexing all the reflections using space group *P*4/*nmm* and the efforts were failed to index the whole diffraction pattern. The observed NPD data fits well with the space group *Pcnb* though the difference curve is not quite good. The observed *a*- and *b* lattice parameters are very close to each other, this indicates the structure is looks like pseudo-tetragonal. The highly distorted WO_6 octahedral networks, containing few Li into the channels, maybe led to this pseudo-tetragonal structure.

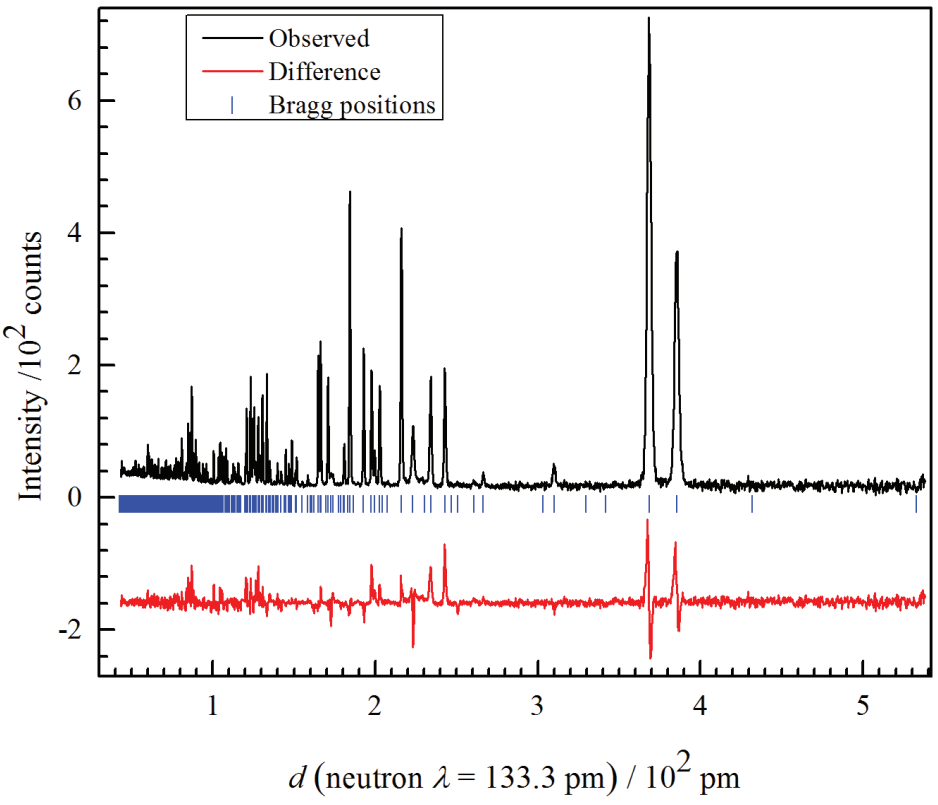

Figure 3.10. Rietveld refinement plot for time-of-flight neutron powder diffraction data of $Li_{0.1}(W^{6+}_{0.9}W^{5+}_{0.1})O_3$ bronze measured at 380 K.

Table 3.10. Details of the crystal structural feature of $Li_{0.1}(W^{6+}_{0.9}W^{5+}_{0.1})O_3$ bronze obtained from time-of-flight neutron powder diffraction data collected at 380 K.

Space group: *Pcnb*, *a* = 737.13(3) pm, *b* = 737.30(4) pm, *c* = 771.36(3) pm, *Z* = 8, R_{wp} = 15.94 %						
Atom	Wyckoff	*x*	*y*	*z*	Occupancy	U_{iso} /10^4 • pm^2
W	8*d*	0.2429(7)	0.9989(6)	0.2854(5)	1	0.0053(7)
O1	8*d*	0.0008(7)	0.9686(6)	0.2084(5)	1	0.0051(6)
O2	8*d*	0.2173(14)	0.2530(19)	0.2542(16)	1	0.0683(27)
O3	8*d*	0.2970(6)	0.0195(7)	0.0024(5)	1	0.0151(10)
Li	4*c*	½	¼	0.05(7)	0.20(1)	0.07(7)

All the atomic positional parameters given in Table 3.10 are in good agreement with the results obtained from room-temperature powder XRD data. Rietveld refinement results of powder XRD data showed that simultaneous refinement of occupancy and mean atomic displacement parameter of lithium is not possible because of low X-ray scattering power of Li, whereas neutron powder diffraction data offered better results and the lithium content is almost close to the used nominal composition, that is x = 0.1. Selected interatomic distances and angles are given in Table 3.11. All these values are in the acceptable range compared to those of others alkali metal tungsten bronzes [102].

Table 3.11. Selected interatomic distances and angles of $Li_{0.1}(W^{6+}_{0.9}W^{5+}_{0.1})O_3$ bronze obtained from time-of-flight neutron powder diffraction data measured at 380 K.

Atoms	Count	Distances /pm	Atoms	Distances /pm	W–O–W /°
Li–O1a	2x	246(41)	W–O1a	189.41(71)	155.78(37)
Li–O1b	2x	335(42)	W–O1b	191.67(73)	
Li–O2a	2x	261(3)	W–O2a	186(1)	165.10(87)
Li–O2b	2x	279(4)	W–O2b	190(1)	
Li–O3a	2x	229(9)	W–O3a	170.63(55)	157.79(28)
Li–O3b	2x	252(9)	W–O3b	222.43(55)	

The mean atomic displacement of Li is large enough because its content is very few compared to the available empty sites and the dimensions of tetragonal tunnels. Since Li is in the

channels, the Li–O interatomic distances are larger than that of the typical Li–O bond distance. Among the six W–O bond distances, one is shorter followed by another longer bond, others four are close to the normal W–O bond distances. It indicates the distorted WO_6 octahedron further more elongated in a particular direction.

Temperature-dependent NPD data Rietveld refinements results show a nonlinear change of the metric parameters. Powder XRD data collected from 100 K to 400 K also showed a nonlinear change of the lattice parameters. All three lattice parameters are nonlinearly lengthened with increasing temperature (Figure 3.11). The anisotropy parameter $A = |a - b| + |b - c| + |c - a|$ showed a sigmoid behavior with slowing down saturation at about 680(5) K. Moreover, the intensity of at least one Bragg reflection (*311*) gradually decreased and finally disappeared at 680 K, which is a clear hint of structural change at high-temperature region. Temperature-dependent cell volume also expanded nonlinearly with temperature as shown in Figure 3.11. The $Li_{0.1}(W^{6+}_{0.9}W^{5+}_{0.1})O_3$ bronze shows positive volume thermal expansion like many others common solid materials. Temperature-dependent metric parameters show an anomaly in the region of 200 K – 300 K. The observed temperature-dependent matric parameters were fitted using Debye-Einstein (DE) model. It could be expressed using the equations given below, for more details see ref. [103, 104, 105].

$$M(T) = M_0 + \sum_{i=1}^{d} k_{\mathrm{Di}} U_{\mathrm{Di}}(T) + \sum_{i=1}^{e} k_{\mathrm{Ei}} U_{\mathrm{Ei}}(T) + k_{\mathrm{A}} U_{\mathrm{A}}(T)$$

$$U_{\mathrm{Di}}(T) = \left[9Nk_{\mathrm{B}}T\left(\frac{T}{\theta_{\mathrm{Di}}}\right)^3 \int_0^{\theta_{\mathrm{Di}}/T} \frac{x^3}{e^x - 1} dx \right]^3 \qquad U_{\mathrm{Ei}}(T) = \left[\frac{3Nk_{\mathrm{B}}\theta_{\mathrm{Ei}}}{e^{(\theta_{\mathrm{Ei}}/T)} - 1} \right]$$

$$U_{\mathrm{A}}(T) = \left[a_A \frac{3Nk_{\mathrm{B}}\theta_{\mathrm{A}}^2}{24T} \left[Te^{(3\theta_{\mathrm{A}}/T)} + 9Te^{(2\theta_{\mathrm{A}}/T)} - 12\theta_{\mathrm{A}}e^{(2\theta_{\mathrm{A}}/T)} - 9\mathrm{T}e^{(\theta_{\mathrm{A}}/T)} - 12\theta_{\mathrm{A}}e^{(\theta_{\mathrm{A}}/T)} - T \right] \left[\left(e^{(\theta_{\mathrm{A}}/T)} - 1\right)^3 \right]^{-1} \right]$$

N refers to the number of atoms per unit cell, k_B is the Boltzmann constant, θ_{Di} and θ_{Ei} are the characteristic Debye ($\theta_{Di} = hc\omega_{Di}/k_BT$) and Einstein ($\theta_{Ei} = hc\omega_{Ei}/k_BT$) temperatures. *M(T)* refers to any of the temperature-dependent metric parameters (*V(T)*, *a(T)*, *b(T)*, and *c(T)*), k_{Di}, k_{Ei} and k_A are adjustable fitting parameters given in Table 3.13, U_{Di}, U_{Ei} and U_A are Debey, Einstein and anharmonic internal energies contributions, respectively. Here the anharmonic energy contribution (k_AU_A(T)) is not used for fitting the observed data set. The DE model fit

provides the metric parameters M_0 at 0 K, Debye (θ_D)- and Einstein (θ_E) temperatures of this bronze material. The calculated metric parameters at 0 K, the Debye- and the Einstein temperatures are given in Table 3.13.

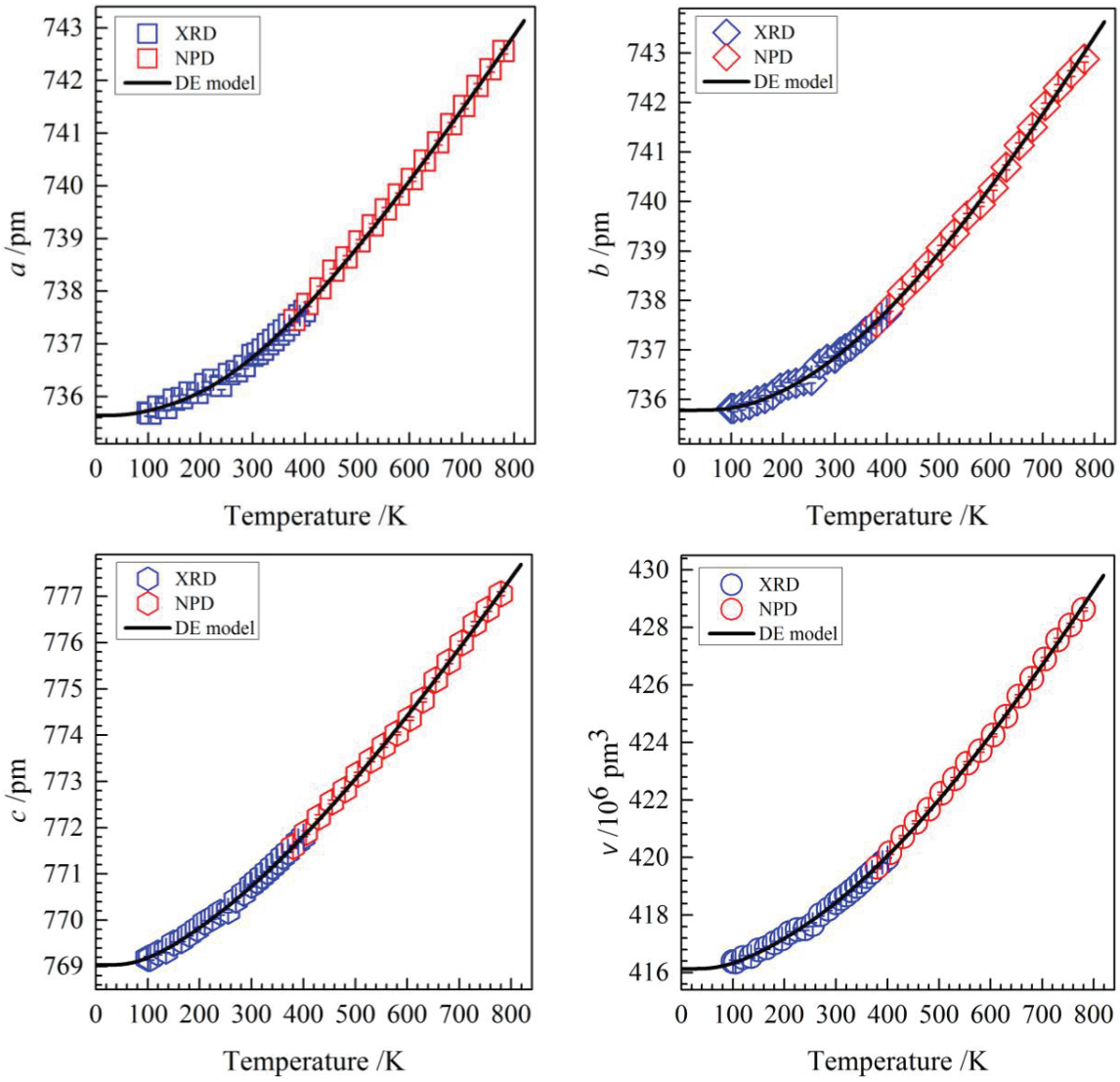

Figure 3.11. Change of lattice parameters and cell volume with respect to temperature of $Li_{0.1}(W^{6+}_{0.9}W^{5+}_{0.1})O_3$ bronze obtained from X-ray (90 K – 400 K) and neutron (380 K – 780 K) powder diffraction data Rietveld refinements. The solid red line is for Debye-Einstein model.

3.3.2. Low-temperature Raman spectra analysis

The factor group analysis predicts ($4 \bullet (3A_g + 3B_{1g} + 3B_{2g} + 3B_{3g}) = 4 \bullet 12$) 48 Raman active modes for the space group *Pcnb* of $Li_{0.1}(W^{6+}_{0.9}W^{5+}_{0.1})O_3$ bronze. The Raman spectrum of

$Li_{0.1}(W^{6+}_{0.9}W^{5+}_{0.1})O_3$ powder sample shows 30 bands in the range of 80 cm^{-1} – 880 cm^{-1} at 78 K as shown in Figure 3.12. Some bands could be located in the lower Raman shift region and others may not be well resolved from the background because of very low intensity peaks. Whereas the factor group analysis offers six Raman active modes for the *P*4/*nmm* space group, fewer bands compared to the number of bands observed. The observed Raman spectrum also indicates that the *P*4/*nmm* space group is not correct for $Li_{0.1}(W^{6+}_{0.9}W^{5+}_{0.1})O_3$ bronze as confirmed by X-ray and neutron powder diffraction data.

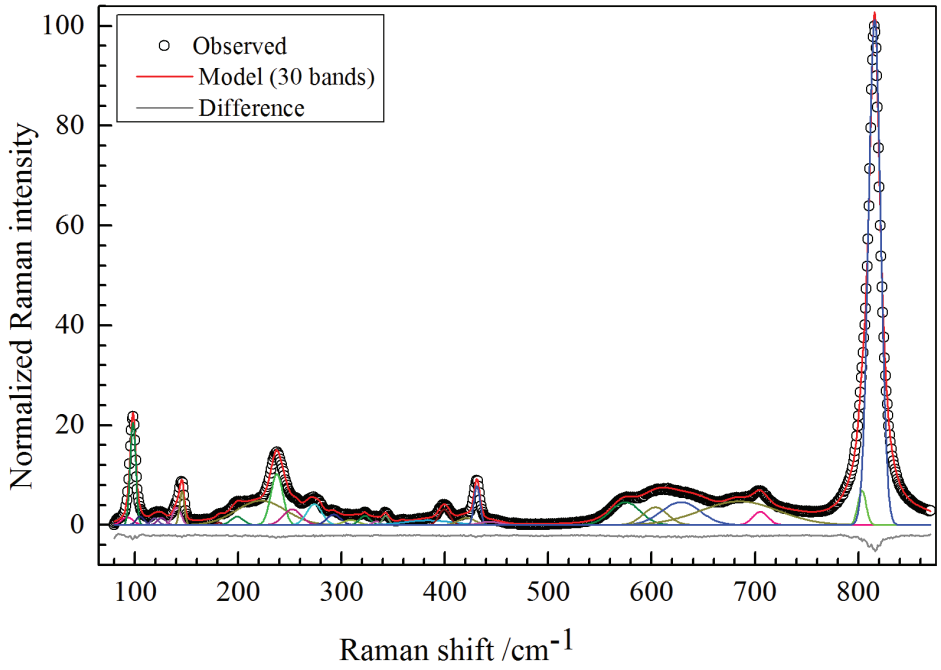

Figure 3.12. Raman spectrum of $Li_{0.1}(W^{6+}_{0.9}W^{5+}_{0.1})O_3$ bronze recorded at 78 K on a smooth surface of pressed pellet powder sample.

The observed Raman peaks in the range of 80 cm^{-1} to 880 cm^{-1} Raman shift region presented in the Figure 3.12 can be divided into two parts; 520 cm^{-1} – 880 cm^{-1} and 80 cm^{-1} – 460 cm^{-1}. In the first range only the stretching vibrations of W–O bonds are observed [106]. There are seven bands in this region. In the second region, the bending modes of W–O–W bridging bond and O–W–O bonds are observed [106]. There are 23 observable bands in this region. Some bands are diffuse and broad whereas few bands are very sharp. The phonon modes with frequencies < 500 cm^{-1} are due to the bending modes of O–W–O vibrations and those which are sited below 200 cm^{-1} because of W–O–W bridging bonds vibrations. The characteristics

bands associated with the vibrational modes of Li–O bonds are possibly located in the very low Raman shift region since Li–O interatomic distances are very large, and it may be well possible that the bands are situated below the detection limit (≤ 80 cm^{-1}) of this instrument. The temperature-dependent Raman shift for selected W–O bonds show most of the vibrational modes become harder at low-temperature conditions; however one of the W–O stretching mode (about 705 cm^{-1} at 78 K) shows right Raman shift (Figure 3.13). It indicates that one particular W–O bond is becoming harder while the material is heated up from liquid-nitrogen temperature to room-temperature. Temperature-dependent Raman data also demonstrate that there is a phonon modes anomaly from 205 K to 250 K as shown in Figure 3.13 (light dotted lines). The reason for such anomaly is still unknown. It may be due to the thermal phonon decay or inter-octahedral rearrangement within the structure. Temperature-dependent X-ray powder diffraction data Rietveld refinements results also show an anomaly for the lattice parameters change within this temperature range.

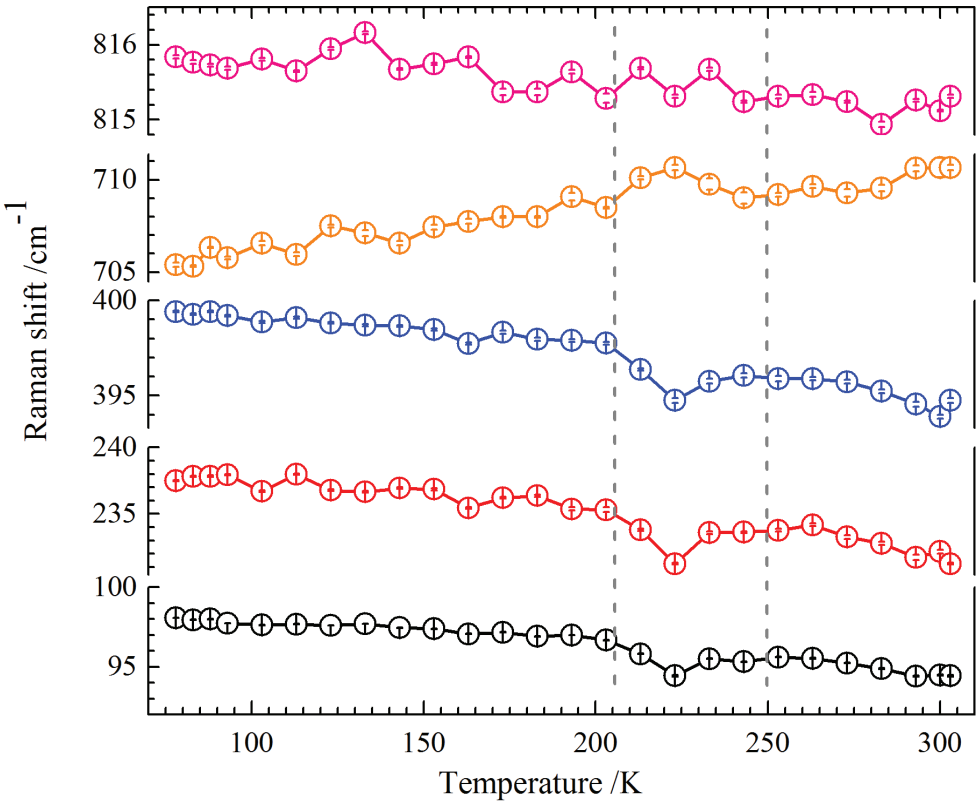

Figure 3.13. Temperature-dependent Raman shift for selected bands within the $Li_{0.1}(W^{6+}_{0.9}W^{5+}_{0.1})O_3$ bronze. The solid lines are for eye guide and dotted lines are for showing anomaly region.

3.4. Thermal behavior of $Li_{0.4}(W^{6+}_{0.6}W^{5+}_{0.4})O_3$ bronze

The temperature-dependent thermal expansions of $Li_{0.4}(W^{6+}_{0.6}W^{5+}_{0.4})O_3$ bronze have been investigated from NPD data collected at high-temperature (380 K to 780 K), as well as from temperature-dependent (100 K – 400 K) powder X-ray diffraction data. Temperature-dependent Raman spectra were also examined at low-temperature region (78 K – 303 K) for studying the thermal behaviors of different vibrational modes of this compound.

3.4.1. Temperature-dependent powder diffraction data investigation

The high-temperature NPD data of $Li_{0.4}(W^{6+}_{0.4}W^{5+}_{0.6})O_3$ bronze were also refined in the space group $Im\bar{3}$. Rietveld refinement plot of NPD data of $Li_{0.4}(W^{6+}_{0.6}W^{5+}_{0.4})O_3$ bronze at 380 K is shown in Figure 3.14. Details of the crystal structure are given in Table 3.12. The NPD data Rietveld refinements allowed to unambiguously locate lithium over two different Wyckoff sites centered at 2*a* and 6*b* of space group $Im\bar{3}$ for $Li_{0.4}(W^{6+}_{0.6}W^{5+}_{0.4})O_3$ bronze.

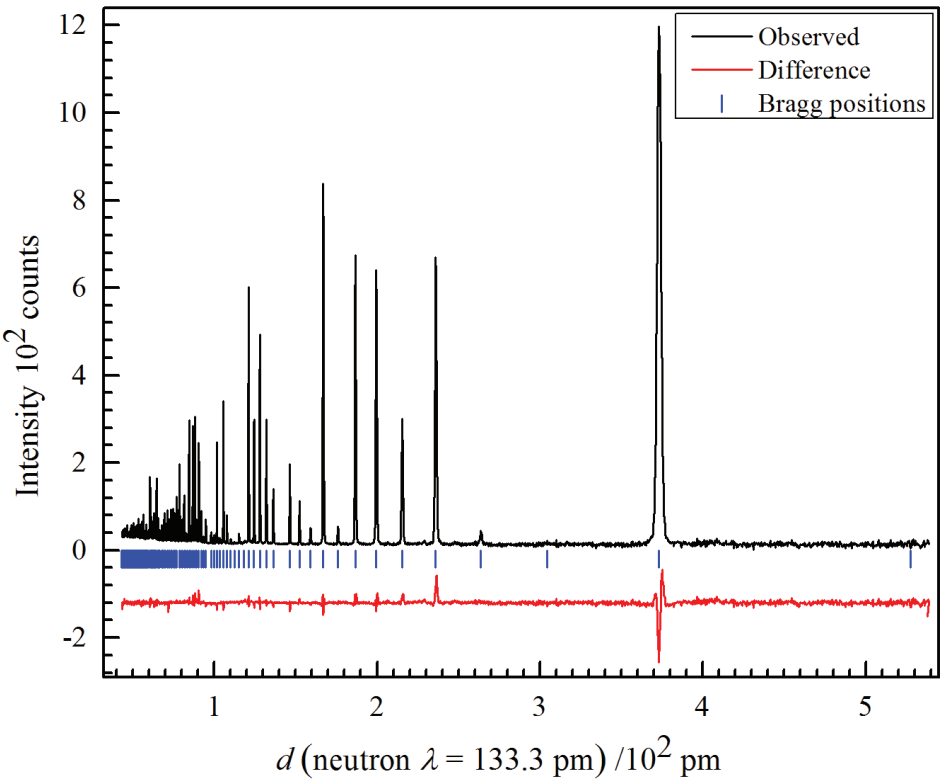

Figure 3.14. Rietveld refinement plot for neutron powder diffraction data of $Li_{0.4}(W^{6+}_{0.6}W^{5+}_{0.4})O_3$ bronze ($Im\bar{3}$) measured at 380 K.

Constraints were used to calculate the distribution of total lithium content into eight perovskite-type cavities (centered at 2*a* and 6*b*) formed in the space group $Im\bar{3}$. It offers the total lithium content to be equivalent to the used nominal composition (i.e. x = 0.4). Isotropic mean atomic displacement of Li1 (occupied at 2*a* site) was set as four times of Li2, (occupied at 6*b* site) because the channels dimensions of both cavities are different from each other. In the 6*b* site four-fold coordinated oxygen atoms offer the smaller aperture [½(shortest O–O distance – 2•r_o (CN, CR)] of 26.7 pm for Li2 whereas in the 2*a* site twelve-fold coordinated oxygen environment provide a lager cavity [½(shortest O–O distance – 2•r_o (CN, CR)] of 39.5 pm for Li1. Temperature-dependent NPD data show that the Li atoms are successively moving from 6*b* site to 2*a* site in the studied temperature region (380 K to 780 K) as shown in Figure 3.15. It is an interesting phenomenon that the loosely bonded Li2 occupied at 6*b* site are in dynamic motion, gaining energy and hopping to 2*a* site with increasing temperature. This observation support the ionic conductivity of some Li_xWO_3 bronzes at high-temperature conditions [49].

Table 3.12. Details of the crystal structure of $Li_{0.4}(W^{6+}_{0.6}W^{5+}_{0.4})O_3$ bronze obtained from neutron powder diffraction data Rietveld refinement measured at 380 K.

Space group: $Im\bar{3}$, a = 746.263(17) pm, Z = 8, R_{wp} = 6 %						
Atom	Wyckoff	*x*	*y*	*z*	Occupancy	U_{iso} /10^4 • pm^2
Li1	2*a*	0	0	0	0.23(1)	0.12
Li2	6*b*	½	0	0	0.46(2)	0.030(2)
W1	8*c*	¼	¼	¼	1	0.0064(1)
O1	24*g*	0	0.20607(9)	0.28998(9)	1	0.0101(1)

Temperature-dependent NPD data of $Li_{0.4}(W^{6+}_{0.6}W^{5+}_{0.4})O_3$ bronze show nonlinear thermal expansions of its metric parameters. The cell parameter is increasing with increasing temperature. The lattice parameters of $Li_{0.4}(W^{6+}_{0.6}W^{5+}_{0.4})O_3$ bronze obtained from NPD data show a kink at about 410 K. Rietveld refinements results of powder XRD data measured from 90 K to 400 K also show an anomaly ongoing at 260 K for the lattice parameter change of this bronze sample. It is assumed that there is a broad anomaly in between 400 K to 500 K, as well. It indicates that there is a structural change either phase transformation, or occurrence of

metastability due to local rotations of some WO_6–octahedra blocks leading to eventually a soft phonon for electron-phonon interaction as seen in superconducting bronzes [42].

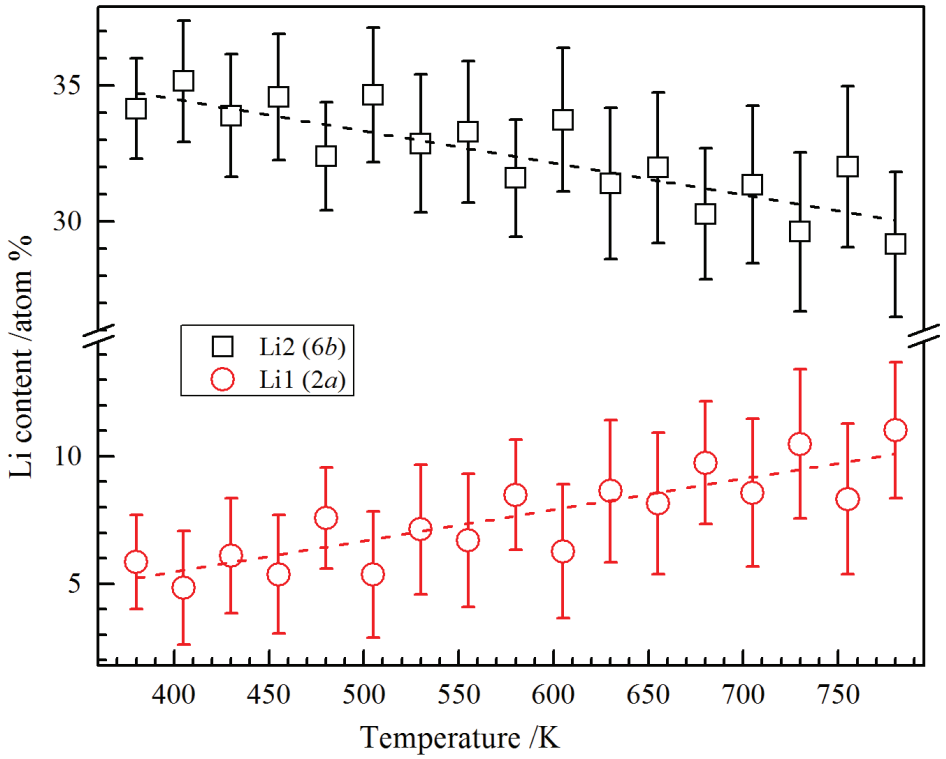

Figure 3.15. Distribution of lithium with temperature into two different Wyckoff sites centered at 2*a* and 6*b* of space group $Im\bar{3}$. The dotted lines are for eye-guide.

Temperature-dependent lattice parameters and cell volumes were fitted (Figure 3.16) using Debye quasi-harmonic and Einstein harmonic model for calculating the metric parameters, M_0 at 0 K, Debye (θ_D),– and Einstein (θ_E) temperatures. The data in the range of 90 K to 400 K and 430 K – 780 K were fitted using individual Debye – and Einstein model, respectively. Both models intersect at about 512 K which could be the borderline of the observed anomaly. The calculated M_0, θ_D and θ_E for $Li_{0.4}(W^{6+}_{0.6}W^{5+}_{0.4})O_3$ bronze are given in Table 3.13. Again, it is observed that the low-Li containing $Li_{0.1}(W^{6+}_{0.9}W^{5+}_{0.1})O_3$ bronze has larger cell volume than that of $Li_{0.4}(W^{6+}_{0.6}W^{5+}_{0.4})O_3$ bronze even at low-temperature. This results indicate that the metric parameters of Li_xWO_3 bronzes were decreased when more lithium is incorporated while others alkali metal tungsten bronzes show opposite behavior for their metric parameters change [90]. The Debye temperatures of both compositions are nearly same; however the

Einstein temperature of low-lithium containing phase is larger than that of high-lithium containing phase. The estimated standard errors are large enough which indicate that the fitted model is not quite good. Since there are anomaly regions of the total data sets and three different data sets which were measured in different instruments, it could be possible that the applying corrections factors are not perfect enough.

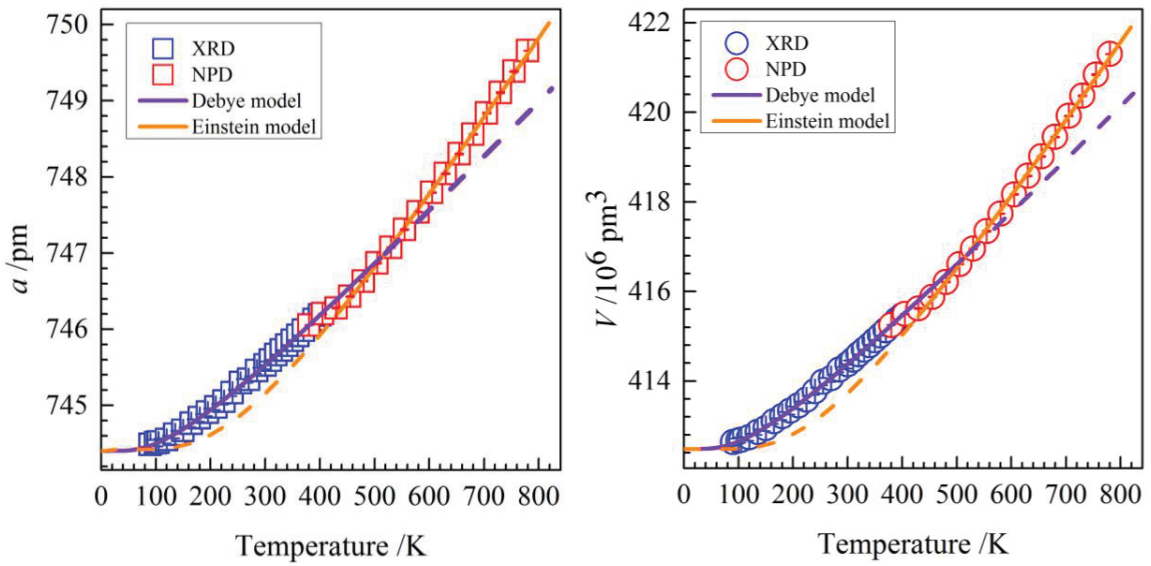

Figure 3.16. Change of lattice parameter and cell volume with respect to temperature of $Li_{0.4}(W^{6+}_{0.6}W^{5+}_{0.4})O_3$ bronze obtained from X-ray (90 K – 400 K) and neutron (380 K – 780 K) powder diffraction data Rietveld refinements. The solid lines are for Debye– and Einstein model.

Table 3.13 Resulting values obtained from the Debye-Einstein fitting of the temperature-dependent metric parameters of lithium tungsten bronzes.

M	$Li_{0.4}(W^{6+}_{0.6}W^{5+}_{0.4})O_3$		$Li_{0.1}(W^{6+}_{0.9}W^{5+}_{0.1})O_3$			
	a	*V*	*a*	*b*	*c*	*V*
M_0	744.40(1)	412.48(1)	735.64(1)	735.78(1)	769.01(1)	416.13(1)
$k_D/10^{-12}$	4.43(10)	7.37(15)	2.6(20)	5.5(28)	6.2(9)	8.4(16)
θ_D/K	483(17)	477(16)	383(293)	745(264)	453(78)	468(98)
$k_E/10^{-12}$	6.82(23)	11.4(4)	7.1(16))	6.1(20)	4.6(7)	11.1(12)
θ_E/K	763(36)	756(36)	1106(234)	1587(563)	1636(452)	1641(309)

Metric parameters *a*, *b*, *c*, and *V* at 0 K are given in pm and 10^6 pm^3, respectively. Estimated uncertainty is given in the parentheses. Median values is 2σ e.s.d.'s

Temperature-dependent mean atomic displacement (U_{iso}) parameters of constituent elements of $Li_{0.4}(W^{6+}_{0.6}W^{5+}_{0.4})O_3$ bronze were refined from high-temperature NPD data. These are increasing with temperature for all atoms as shown in Figure 3.17. Another notable feature, the U_{iso} of all the constituent elements follow a general trend. The lighter element lithium has larger mean atomic displacement than that of heavier atoms oxygen or tungsten, similarly the U_{iso} of oxygen is larger than that of the heavier atom tungsten. It is already noticed that since Li1 is located into larger cavities than that of Li2, the isotropic mean atomic displacement parameter of Li1 was set as four-times larger than that of Li2, and constraints were set in such a manner during the refinements. Otherwise, it shows some unphysical values for Li1 occupying in 2*a* site and the total content of Li is lower than the used nominal composition.

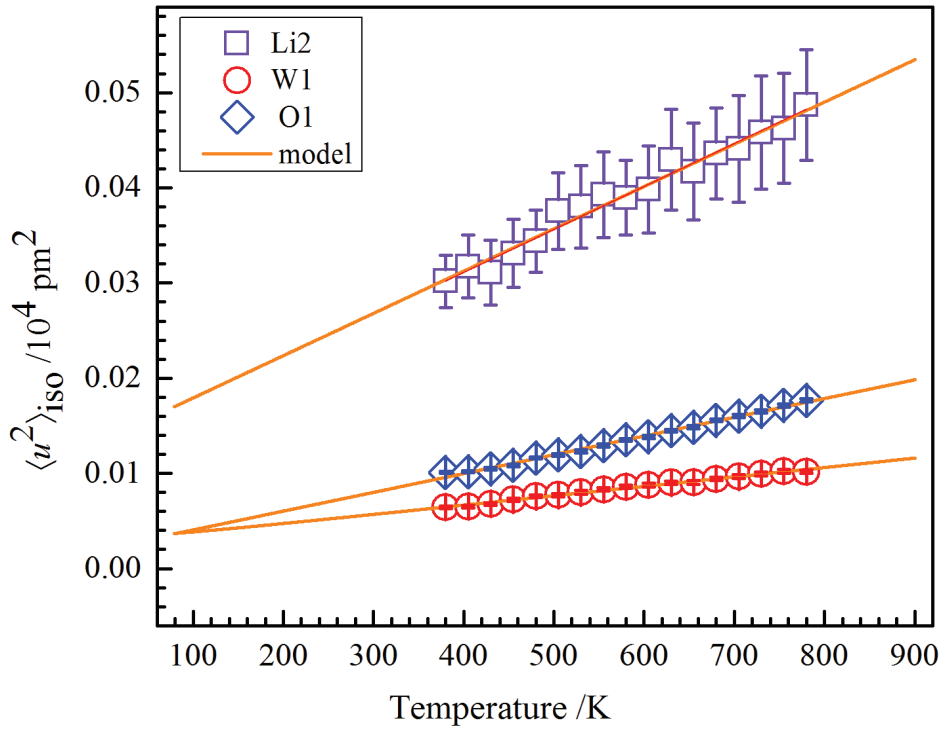

Figure 3.17. Changes of mean atomic displacement parameters (U_{iso}) of Li2, O1 and W1 in the $Li_{0.4}(W^{6+}_{0.6}W^{5+}_{0.4})O_3$ bronze obtained from neutron powder diffraction data Rietveld refinements measured from 380 K to 780 K.

3.4.2. Low-temperature Raman spectra analysis

Ten Raman active modes are predicted from the factor group analysis ($2A_g + 2^1E_g + 2^2E_g + 4T_g = 10$) of $Li_{0.4}(W^{6+}_{0.6}W^{5+}_{0.4})O_3$ bronze crystallized in the space group $Im\bar{3}$. The Raman

spectrum of $Li_{0.4}(W^{6+}_{0.6}W^{5+}_{0.4})O_3$ powder sample recorded at 78 K was fitted using 17 bands as shown in Figure 3.18, more number of bands than the theoretical calculation. There are many reasons for finding more Raman bands in this material. One of the causes could be the different oxidation states (probably W^{6+} and W^{5+}) of tungsten. The energy differences between W^{6+}–O and W^{5+}–O bonds present in the same compound maybe led Raman peaks at closely related two different positions. The material contains a lot of free carriers which also maybe influence the number of Raman bands. Since Li^+ are in the channels as a free carrier and the electrons donated by Li are delocalized over the tungsten atoms could also be effects the Raman bands. The given spectrum was recorded in the range of 80 cm^{-1} – 1100 cm^{-1}. It may also possible that there are more Raman bands in the lower wavenumber region, located below the detection limit of this instrument (≤ 80 cm^{-1}). The observed Raman peaks in the range of 80 cm^{-1} to 1100 cm^{-1} wavenumber presented in the Figure 3.18 can be divided into two broad parts; 500 cm^{-1} – 1050 cm^{-1} and 80 cm^{-1} – 500 cm^{-1}. In the first range (500 cm^{-1} – 1100 cm^{-1}) only the stretching vibrations of W=O and W–O bonds are observed [106].

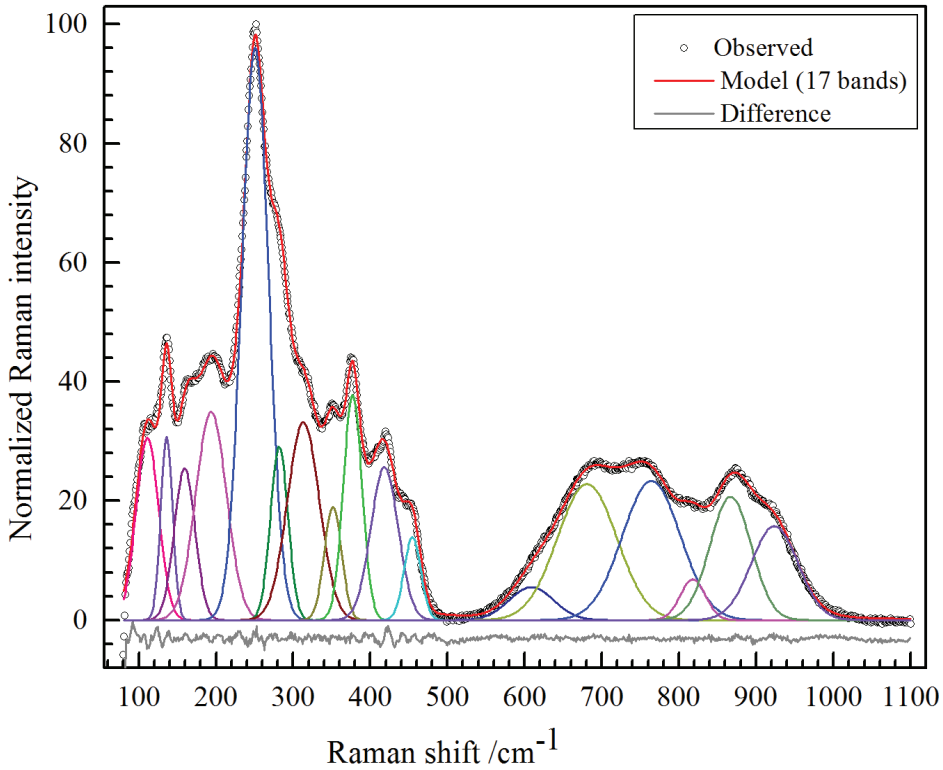

Figure 3.18. Raman spectrum of $Li_{0.4}(W^{6+}_{0.6}W^{5+}_{0.4})O_3$ bronze recorded on a smooth surface of pressed pellet powder sample and at 78 K.

There are six bands in this region. All these bands are broad, diffuse and compound peaks. In the second region (80 cm^{-1} – 500 cm^{-1}), the bending modes of W–O–W bridging bonds and O–W–O bonds are observed [106]. The numbers of observable bands in this region are 11. Most of the peaks are very sharp except few overlapping peaks. The phonon modes with frequencies < 500 cm^{-1} are due to bending modes of O–W–O vibrations and those which are below 200 cm^{-1} are attributable to W–O–W bridging bonds vibrations.

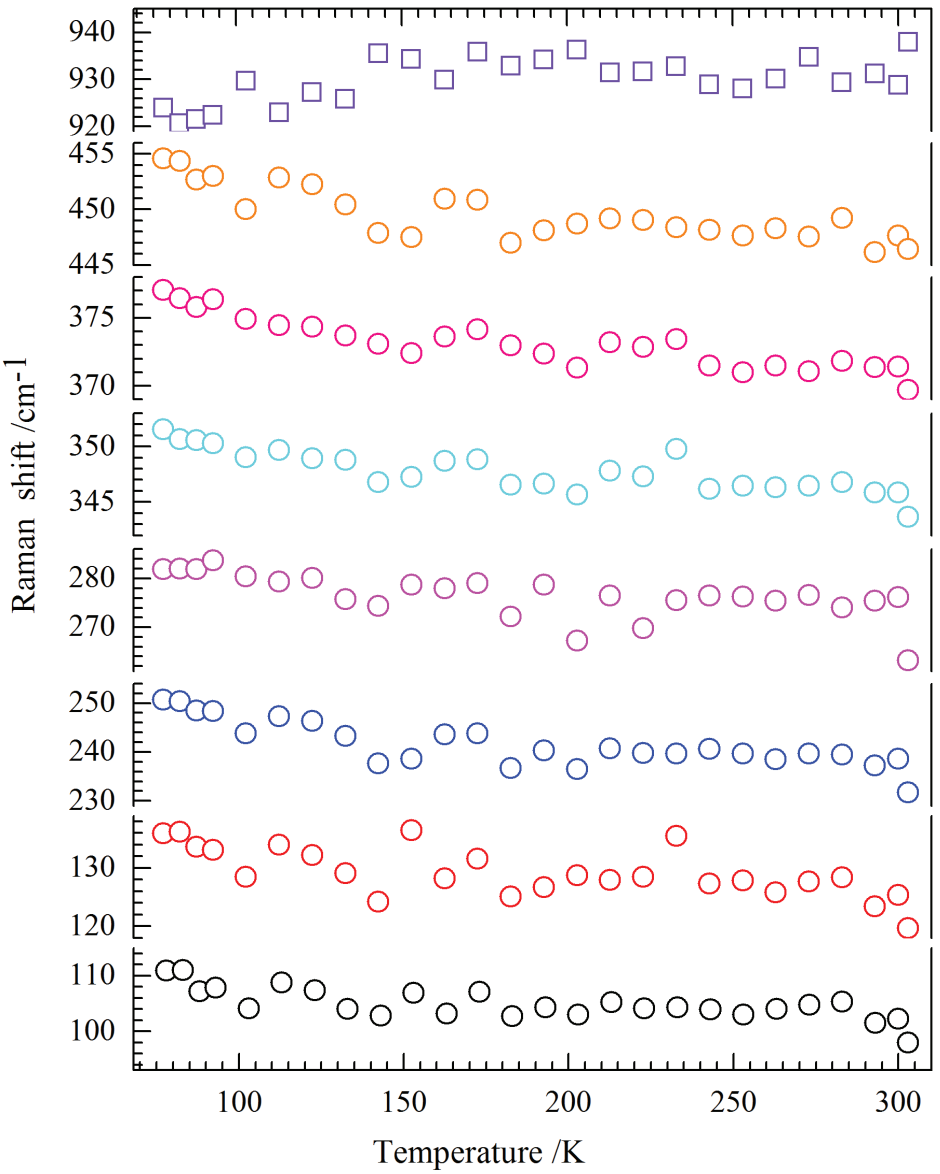

Figure 3.19. Temperature-dependent Raman shifts of selected W–O bonds in the $Li_{0.4}(W^{6+}_{0.6}W^{5+}_{0.4})O_3$ bronze measured from 78 K to 303 K.

The characteristics bands related with the modes of Li–O vibrations maybe located in the very low wavenumber range and it possibly to be found below the detection limit (≤ 80 cm^{-1}) of this instrument. The temperature-dependent measurements show most of the vibrational modes become harder at low-temperature conditions (Figure 3.19); however some modes still remain unchanged even at low-temperature. It indicates that some the bonds gained energy at room-temperature and those are gradually becoming harder during cooling from room-temperature to liquid-nitrogen temperature.

4.1. Structure of $K_{0.3}(W^{6+}_{0.7}W^{5+}_{0.3})O_3$ bronze

The crystal structure of K_xWO_3 ($0.19 \leq x \leq 33$) bronzes have been a subject of controversy. Using X-ray diffraction film technique Magnéli determined the space group of potassium hexagonal tungsten bronze (K-HTB) as $P6_3/mcm$ for x = 0.27 [54]. Opposite, Pye and Dickens [107] found that both, single crystal X-ray and powder neutron diffraction data of $K_{0.26}WO_3$ revealed the absence of the *c*-glide plane, and confirmed the space group $P6_322$. However, Schultz and Horiuchi [108] treated their neutron time-of-flight and single crystal X-ray diffraction data on $K_{0.26}WO_3$ using $P6_3$ space group; lowest symmetry of all three possibilities. The reflection conditions for both space groups, $P6_322$ and subgroup $P6_3$, are the same. Note that a slightly lower *R*-value in a subgroup $P6_3$ is not surprising due to the higher number of variable parameters compared to the supergroup $P6_322$. Therefore, Rietveld refinements of the powder X-ray diffraction data of $K_{0.3}(W^{6+}_{0.7}W^{5+}_{0.3})O_3$ were carried out in each of the three space groups $P6_3$, $P6_322$ and $P6_3/mcm$. All three trials well converged to low *R*-values, however, with small differences. A careful check on the powder X-ray diffraction revealed the presence of *011* and *021* reflections, as seen in Figure 4.1, indicating that the *c*-glide plane is not present and space group $P6_3/mcm$ is inadequate. The intensities for *011* and *021* reflections are just, respectively 0.006 % and 0.009 % of the *020* reflection which provides the highest intensity. Therefore, it may be well possible that such weak reflections were not clearly resolved from the background noise. Even the theoretical neutron diffraction intensities for the weak *011* and *021* reflections comprise of only 0.169 % and 0.438 % intensities of the most intense *044* reflection, respectively. Setting a short 2θ–range we recorded those two reflections for a long time using X-ray powder diffraction at ambient conditions. The well resolved reflections indicate that the space group conforms either to $P6_3$

or $P6_322$ (Figure 4.1, inset), which could hardly be distinguished from powder X-ray diffraction data but clearly using Raman spectroscopy.

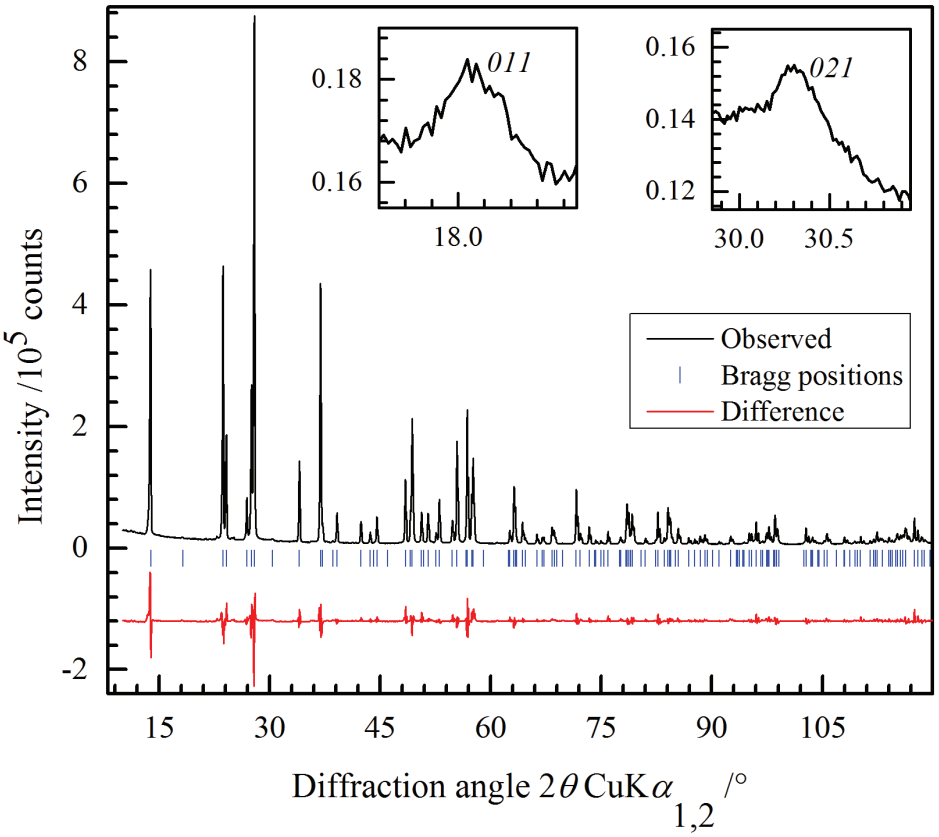

Figure 4.1. Rietveld refinement plot of room-temperature X-ray powder diffraction data of $K_{0.3}(W^{6+}_{0.7}W^{5+}_{0.3})O_3$ bronze ($P6_322$). Presence of weak reflections at *011* and *021* are shown inside view.

Table 4.1. Details of the crystal structure of $K_{0.3}(W^{6+}_{0.7}W^{5+}_{0.3})O_3$ bronze obtained from X-ray powder diffraction data Rietveld refinement.

Space group: $P6_322$, a = 738.67(3) pm, c = 751.98(3) pm, V = 355.34(3) •10^6 pm^3, R_{wp} = 5%						
Atom	Wyckoff	x	y	z	Occupancy	$B_{eq}/10^4$ • pm^2
W	6*g*	0.47796(6)	0	0	1	0.10(3)
O1	6*h*	0.4951(26)	0.9902(53)	0.25	1	0.9(2) [a]
O2	12*i*	0.42874(59)	0.21642(72)	0.0229(14)	1	0.9[a]
K	4*e*	0	0	0.1909(11)	0.45	6.7(4)

[a] Values were constrained to each other during the refinements.

The factor group analysis predicts 65 ($13A + 13^2E_2 + 13^1E_1 + 13^2E_1$), 34 ($6A_1 + 14E_2 + 14E_1$) and 23 ($6A_{1g} + 10E_{2g} + 7E_{1g}$) Raman active modes for the space groups $P6_3$, $P6_322$ and $P6_3/mcm$, respectively. The observed Raman spectrum of $K_{0.3}(W^{6+}_{0.7}W^{5+}_{0.3})O_3$ powder sample recorded at ambient condition was fitted using 31 bands in the range between 80 cm^{-1} and 1200 cm^{-1} as shown in Figure 4.2. The remaining three bands were assumed to be found in the low frequency range based on the low-temperature spectroscopic observation reported by Sagar et al. [109]. Note that these theoretical calculations did not take the possibility of additional (doubled) modes because of W^{6+}–O and W^{5+}–O bonds into account. The presence of observable weak reflections forbidden for a *c*-glide plane in the powder X-ray diffraction data and the total number of observed Raman bands suggests that $P6_322$ is the correct space group for $K_{0.3}(W^{6+}_{0.7}W^{5+}_{0.3})O_3$ bronze, thus agrees well with the previous report of Pye and Dickens [107]. The refined structural parameters are given in Table 4.1.

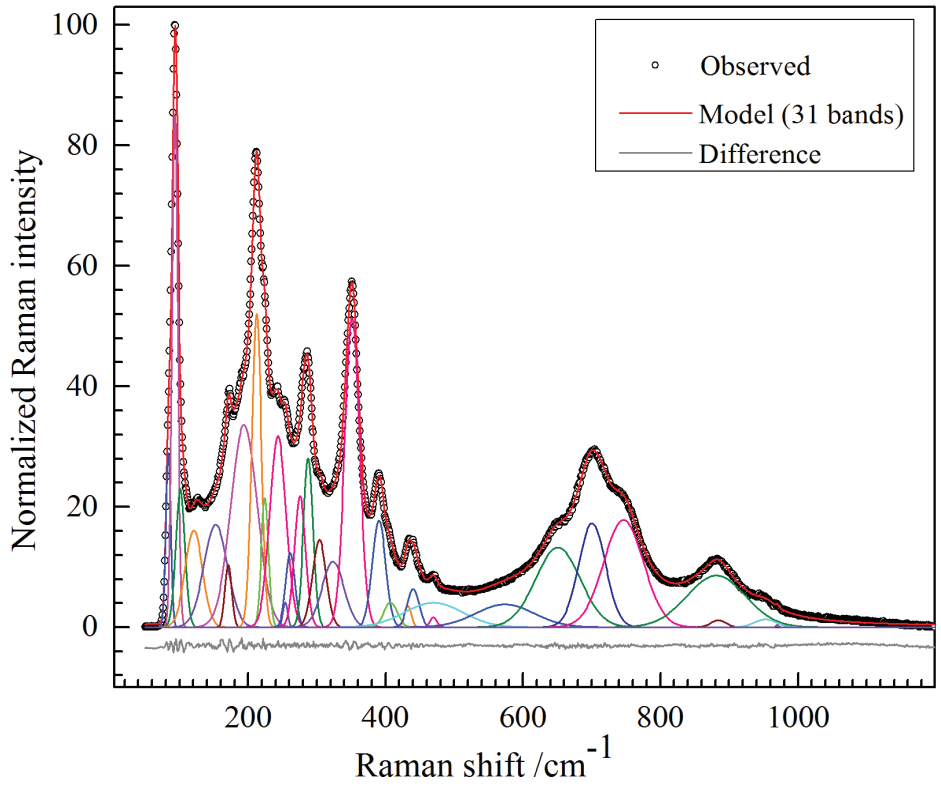

Figure 4.2. Observed and fitted Raman spectrum of $K_{0.3}(W^{6+}_{0.7}W^{5+}_{0.3})O_3$ powder sample showing respective band components. The difference curve justifies the quality of the fit.

Temperature-dependent Raman spectra were also recorded from 78 K to 300 K. The low-temperature measurement was chosen to better resolve the modes and to avoid higher background due to thermal and free carrier (K^+) effects. There are same numbers of bands in the low-temperature regions like room-temperature data. It indicates there is no structural phase transition in the temperature range of 78 K to 300 K.

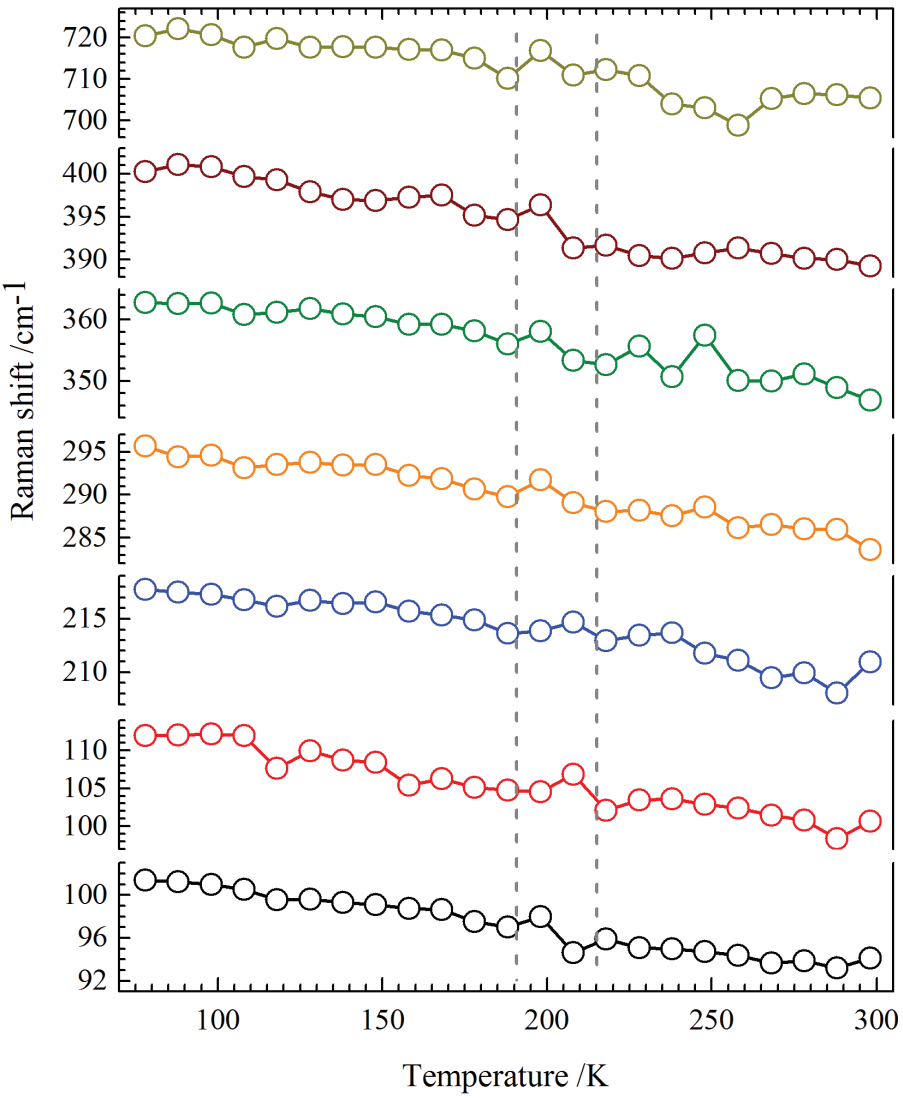

Figure 4.3. Temperature-dependent Raman shift for selected bonds in the $K_{0.3}(W^{6+}_{0.7}W^{5+}_{0.3})O_3$ bronze from 78K to 300 K. The vertical dotted lines showed the possible anomaly region.

Some of the bands are broad and overlapped with others because of closely related vibrational frequencies of different modes at a given temperature. With increasing temperature most of

the bands become softer, the positions of the Raman bands changed to lower values as shown in Figure 4.3. Notably, there is no report on a phase transition at 78 K. Temperature-dependent Raman shift showed a slight anomaly in the temperature range of 190 K – 215 K. Sagar et al. [109] proposed for phase transition at around 200 K which is not discernable in this study. However, Sagar et al. did not provide the structural details of the parent and the newly formed phases. It is only mentioned that some of the bands were disappeared at that temperature in his study. It could be due to the thermal phonon decay. Moreover, the sample contains lots of free carriers (K^+) into the tunnels those also could make a local structural changes. Temperature-dependent powder X-ray diffraction data were collected and analyzed them to make sure that there is no phase transition at around 200 K. Rietveld refinements were performed for low-temperature (100 K – 300 K) powder X-ray diffraction data and all the reflections were indexed in the space group $P6_322$. Temperature-dependent XRD data show similar diffraction patterns and all the reflections are appeared in each diffraction data set. There is no peculiarity of the results or disappearance of reflections in some given temperature range. The lattice parameter *a*- and *c* successively decreased with decreasing temperature leading to a contraction of the cell volume as shown in Figure 4.4.

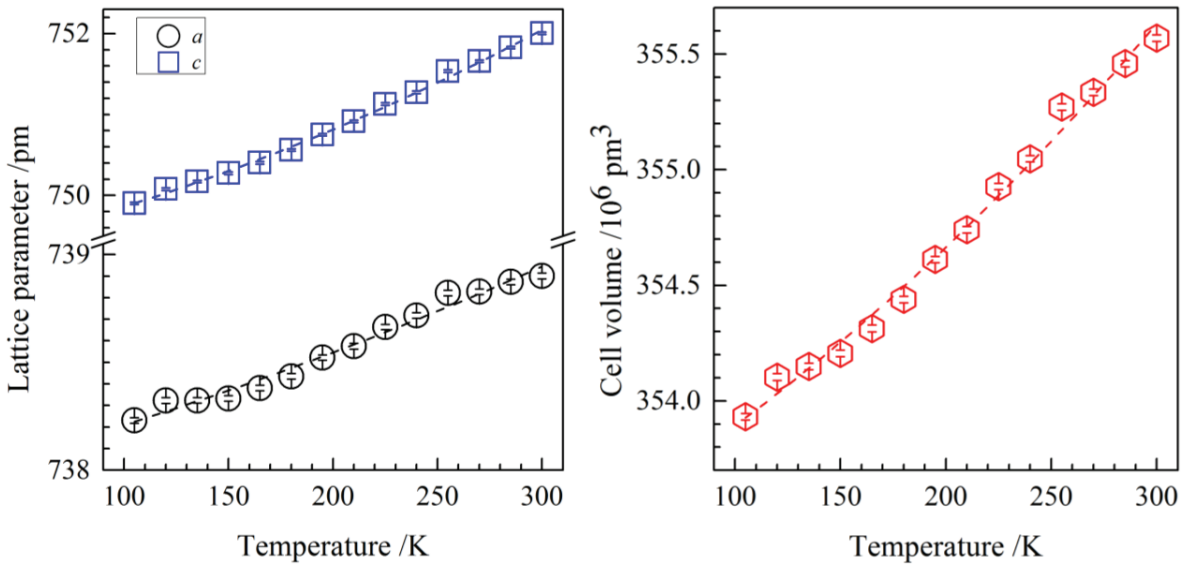

Figure 4.4 Change of lattice parameters (left) and cell volume (right) with respect to temperature of $K_{0.3}(W^{6+}_{0.7}W^{5+}_{0.3})O_3$ bronze obtained from low-temperature powder X-ray diffraction data Rietveld refinements. Dotted lines are for eye-guide.

There is no anomaly or stepdown for matric parameters change. The cell volume expanded nonlinearly with respect to temperature. The synthesized $K_{0.3}(W^{6+}_{0.7}W^{5+}_{0.3})O_3$ bronze sample is stable even at low-temperature conditions. Temperature-dependent Raman and X-ray powder diffraction data clearly show there is no phase transition around 200 K.

4.2. $K_{0.3}(W^{6+}_{0.7}W^{5+}_{0.3-y}Ta^{5+}_{y})O_3$ solid solution series

Polycrystalline powder samples of the $K_{0.3}(W^{6+}_{0.7}W^{5+}_{0.3-y}Ta^{5+}_{y})O_3$ series were characterized by powder X-ray diffraction, SEM/EDX, Raman and Fourier transform infrared (FTIR) spectroscopy.

4.2.1. SEM/EDX analysis

Scanning electron microscopy (SEM) images show the crystallinity of the materials of $K_{0.3}(W^{6+}_{0.7}W^{5+}_{0.3-y}Ta^{5+}_{y})O_3$ series is very poor, as seen in the Figure 4.5. Agglomeration of the polycrystalline materials is observed and it is more distinct for more oxidized phases due to successive dilution of W^{5+} by Ta^{5+} cations. The EDX results show the potassium content is very close to the used nominal compositions. Tantalum is statistically distributed along with tungsten in the polycrystalline products. The averaged K:W, and Ta:W ratios are in good agreement with used nominal composition. The observed EDX results are given in Table 4.2.

Table 4.2. SEM/EDX results of $K_{0.3}(W^{6+}_{0.7}W^{5+}_{0.3-y}Ta^{5+}_{y})O_3$ solid solution series.

y	K/W		Ta/W	
	Used	Observed	Used	Observed
0.05	0.316	0.312(20)	0.053	0.066(4)
0.10	0.333	0.313(21)	0.111	0.108(12)
0.15	0.353	0.346(28)	0.176	0.175(20)
0.20	0.375	0.376(23)	0.250	0.240(14)
0.25	0.400	0.381(20)	0.333	0.326(9)
0.30	0.428	0.421(27)	0.428	0.405(5)

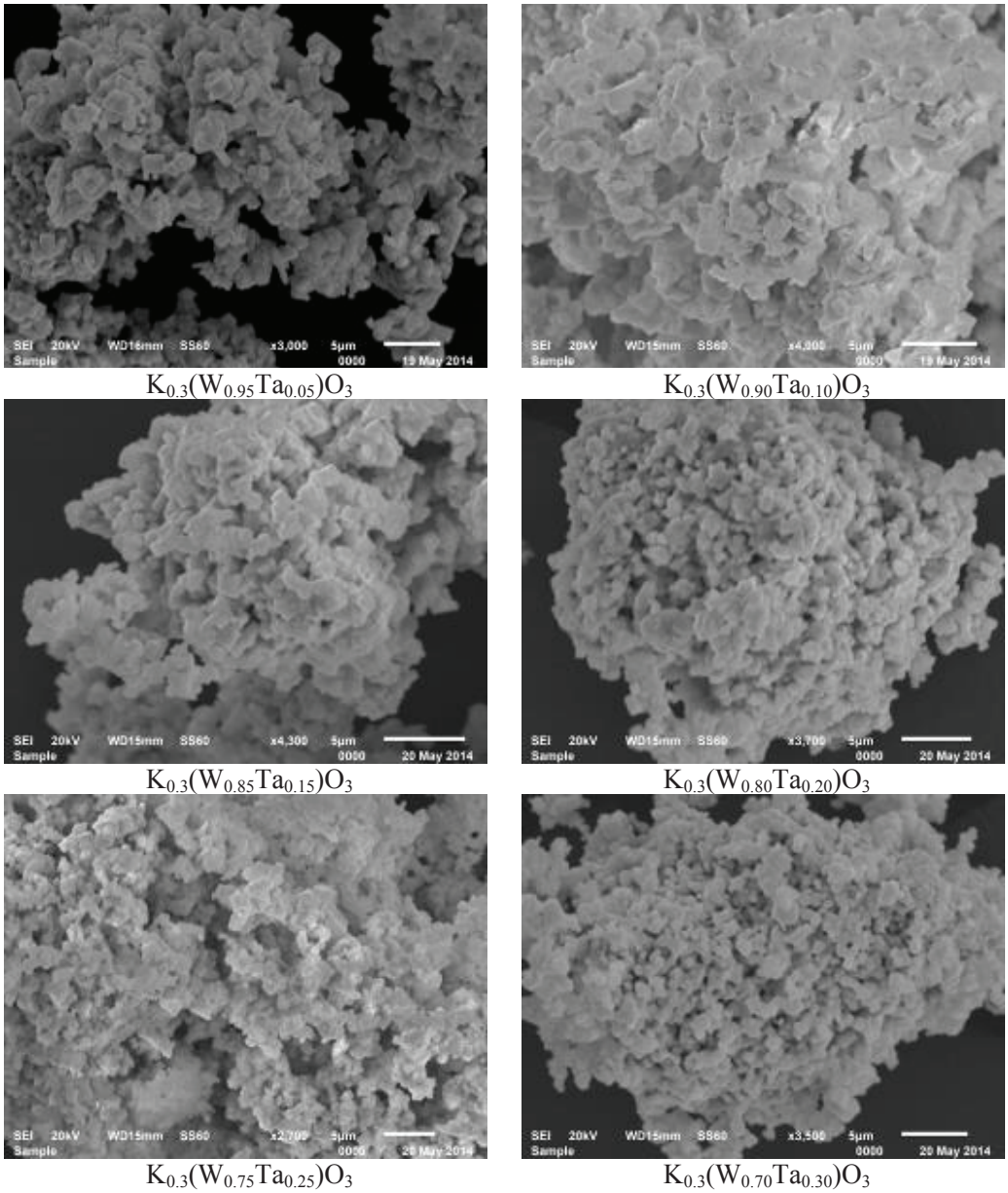

Figure 4.5. SEM micrographs of Ta^{5+} substituted $K_{0.3}(W^{6+}_{0.7}W^{5+}_{0.3-y}Ta^{5+}_{y})O_3$ solid solution series.

4.2.2. Powder X-ray diffraction data investigation

Powder X-ray diffraction data Rietveld refinement confirmed that the solid solution $K_{0.3}(W^{6+}_{0.7}W^{5+}_{0.3-y}Ta^{5+}_{y})O_3$ follows the parent (as $K_{0.3}WO_3$) space group $P6_322$. Figure 4.6 and Table 4.3 show the powder XRD patterns and the Rietveld refinements results, respectively. Our repeated attempts showed that W^{5+} can only be partially replaced by Ta^{5+} in the HTB phase for $y < 0.1$, producing a pure single phase. This finding clearly contradicts to a

recent report [39], where pure phases were reported for up to y = 0.3, nevertheless the given reflection profiles of the diffraction patterns are comparable to the one of the samples reported here. The deviations of lattice parameters are small and there are only Pawley-fit refinements, structure refinements were not carried out. It is well possible that the single phase refinements were done using broader reflections and slightly different lattice parameters. Samples synthesized with nominal compositions of $y \geq 0.1$ showed a mixture of two phases, namely, HTB-I (W^{5+} is partially replaced) and HTB-II^{m} (W^{5+} is more or less fully replaced, oxidized phase, m = mixed phase appearance), both of which conform the space group $P6_322$. The phase fraction of the HTB-II^{m} increased with increasing nominal Ta^{5+} composition till reached a fully oxidized bronzoid phase, that is, $K_{0.3}(W^{6+}_{0.7}Ta^{5+}_{0.3})O_3$. Details of the structural features of both HTB-I and HTB-II^{m} are given in Table 4.4. Selected bond distances and angles are given in Table 4.5. The deep-blue color $K_{0.3}(W^{6+}_{0.7}W^{5+}_{0.3})O_3$ bronze has been faded up to a cream-colored $K_{0.3}(W^{6+}_{0.7}Ta^{5+}_{0.3})O_3$ upon successive dilution of W^{5+} by Ta^{5+} cation in the $K_{0.3}(W^{6+}_{0.7}W^{5+}_{0.3-y}Ta^{5+}_{y})O_3$ solid solution series. In the tungsten bronze systems W^{5+} cations could be the color centers whose concentrations ultimately determine the various colors of tungsten oxides bronzes.

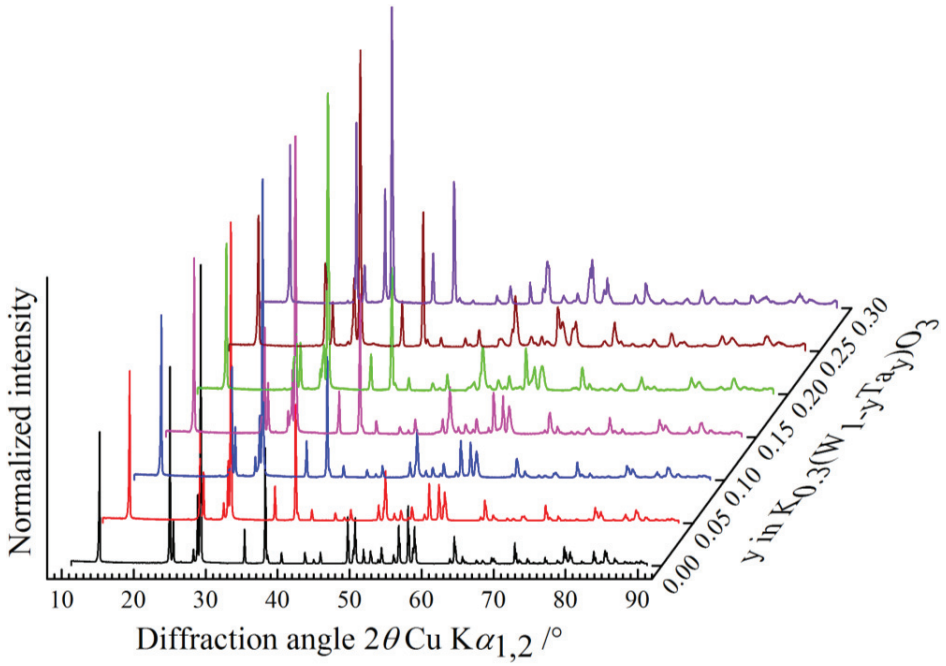

Figure 4.6. Powder X-ray diffraction patterns of $K_{0.3}(W^{6+}_{0.7}W^{5+}_{0.3-y}Ta^{5+}_{y})O_3$ solid solution series.

Table 4.3. X-ray diffraction data Rietveld refinements results of $K_{0.3}(W^{6+}_{0.7}W^{5+}_{0.3-y}Ta^{5+}_{y})O_3$ series.

y	HTB-I			HTB-II^m		
	wt-%	*a* /pm	*c* /pm	wt-%	*a* /pm	*c* /pm
0.00	100	738.67(3)	751.99(3)	-	-	-
0.05	100	738.37(1)	751.65(1)	-	-	-
0.10	89.9(3)	737.99(1)	752.11(1)	10.1(3)	734.49(8)	762.39(10)
0.15	79.3(4)	737.62(2)	752.98(2)	20.7(4)	734.27(4)	763.27(5)
0.20	61.1(6)	736.62(2)	754.47(2)	38.9(6)	733.96(3)	763.21(4)
0.25	46.1(7)	735.17(3)	758.76(3)	53.9(7)	733.18(3)	765.18(3)
0.30	-	-	-	100	732.66(2)	767.50(3)

For the reduced phases, the discoloration is due the replacement of W^{5+} by Ta^{5+} cations. However, for the mixed phase, the amount of bronzoid phase ultimately determined the color. In an early study of Doumerc et al. [110] using different synthesis conditions, the existence of mixed phases (HTB-I and HTB-II) was not reported for $K_{0.33}(W^{6+}_{0.7}W^{5+}_{0.3-y}Ta^{5+}_{y})O_3$ ($0.2 \leq y \leq 0.33$). On the other hand Dey et al. [111] observed mixed phases when W^{5+} was substituted by Nb^{5+} during the preparation of $Cs_{0.3}(W_{1-y}Nb_y)O_3$ and $Rb_{0.3}(W_{1-y}Nb_y)O_3$ series. Note, that the fully oxidized HTB-II^m bronzoid phases are reproducible in separate single phase synthesis. The observed metric parameters of these directly synthesized HTB-II phases (HTB-II^s, s = single phase appearance) in this study are close to those of the HTB-II^m phases identified in the mixed phase samples. The effect of lattice parameters observed for the reduced phases is well separated from the effects of potassium variation in the oxidized samples. Additionally, it could be seen that a single phase treatment as carried out by Shakil et al. [39] only slightly affects the lattice parameters as shown in Figure 4.7(a) in the range of higher Ta^{5+} content. With increasing Ta^{5+} concentration in the HTB-I phase the *a*- and *c*-cell parameters change anisotropically, that is, the *a*-cell parameter decreases while the *c*-parameter increases as shown in Figure 4.7(a) followed by non-linear increase of the anisotropy factor ($A = |a - c|$) for HTB-I, HTB-II^m and HTB-II^s phases (Figure 4.7(b)). The observed cell volumes are comparable with the results reported by Shakil et al. [39] as shown in Figure 4.7(c). For an analogy, the similar behavior was also observed for some relevant oxides such as $KTaW_2O_9$ [112 & ref. therein].

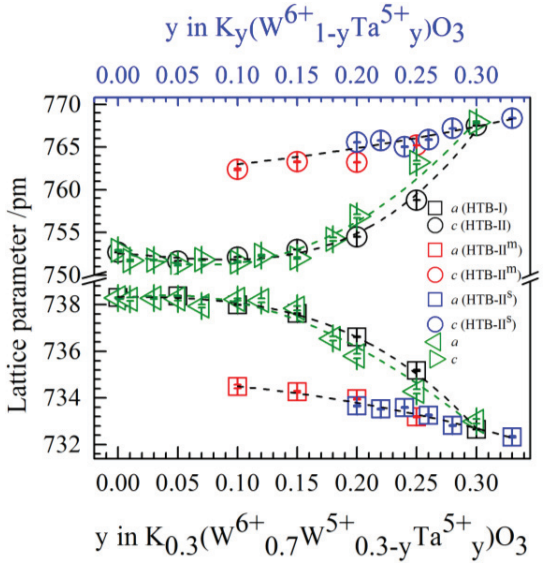

Figure 4.7(a). Change of the lattice parameters with respect to tantalum composition (y) in the $K_{0.3}(W^{6+}_{0.7}W^{5+}_{0.3-y}Ta^{5+}_y)O_3$ bronzes (HTB-I) and $K_y(W^{6+}_{1-y}Ta^{5+}_y)O_3$ bronzoids produced as an additional phase (HTB-II^m), and produced as a pure phase (HTB-II^s). For more details see text. Data from ref. [39] (triangle) are plotted.

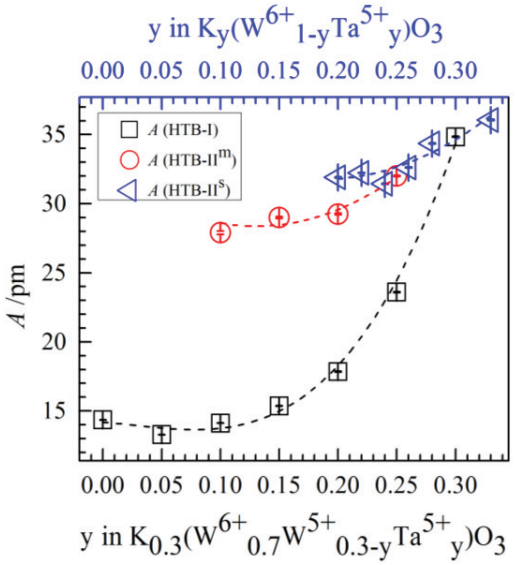

Figure 4.7(b). Change of the anisotropy factor (A) of the HTB-I, HTB-II^m and HTB-II^s phases with respect to tantalum composition (y) in the $K_{0.3}(W^{6+}_{0.7}W^{5+}_{0.3-y}Ta^{5+}_y)O_3$ bronzes and $K_y(W_{1-y}Ta_y)O_3$ bronzoids.

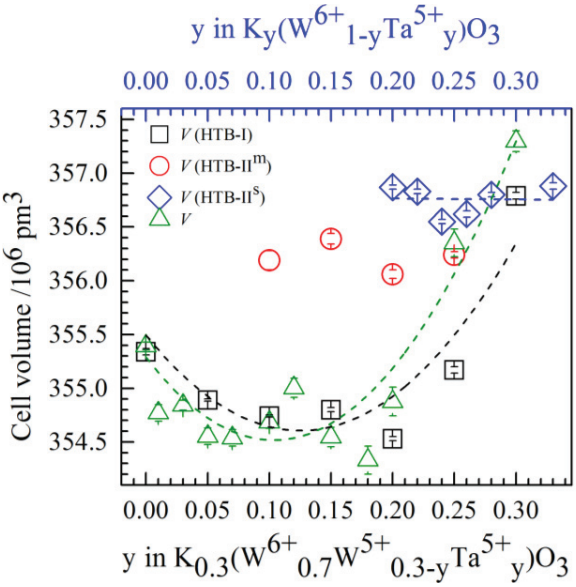

Figure 4.7(c). Change of the cell volume of the HTB-I, HTB-II^m and HTB-II^s phases with respect to tantalum composition (y) in the $K_{0.3}(W^{6+}_{0.7}W^{5+}_{0.3-y}Ta^{5+}_y)O_3$ bronzes and $K_y(W^{6+}_{1-y}Ta^{5+}_y)O_3$ bronzoids. Data from ref. [39] (triangle) are plotted for comparison.

Table 4.4. Details of the structural parameters of $K_{0.3}(W^{6+}_{0.7}W^{5+}_{0.3-y}Ta^{5+}_{y})O_3$, HTB-I and HTB-II^m (*italics*) obtained from powder X-ray diffraction data Rietveld refinements.

y	W(*x*)	O1(*x*)	O2(*x*)	O2(*y*)	O2(*z*)	K(*z*)
0.00	0.47796(6)	0.4951(26)	0.42874(59)	0.21642(72)	0.0229(14)	0.1909(11)
0.05	0.47774(8)	0.5040(28)	0.4361(14)	0.2237(11)	0.9731(17)	0.1855(15)
0.10	0.47782(11)	0.5123(25)	0.42656(95)	0.2161(12)	0.9716(16)	0.1948(12)
0.15	0.47828(15)	0.5194(17)	0.4266(13)	0.2156(16)	0.9694(18)	0.2019(18)
0.20	0.47825(26)	0.5241(20)	0.4256(19)	0.2156(26)	0.9694(25)	0.2019(27)
0.25	0.48093(45)	0.5138(77)	0.4259(29)	0.2168(44)	0.9727(46)	0.2117(56)
0.30	0.48882(30)	0.5210(18)	0.4246(14)	0.2082(27)	0.9590(17)	0.198(2)
0.10	*0.4820(13)*	*0.507(24)*	*0.4116(76)*	*0.189(12)*	*0.9519(64)*	*0.1535(76)*
0.15	*0.48429(75)*	*0.5402(40)*	*0.4244(45)*	*0.205(8)*	*0.9697(54)*	*0.1702(45)*
0.20	*0.48351(64)*	*0.5113(55)*	*0.4049(39)*	*0.1841(60)*	*0.9466(28)*	*0.1805(28)*
0.25	*0.48433(58)*	*0.5151(49)*	*0.4120(34)*	*0.1918(53)*	*0.9470(25)*	*0.1832(23)*

Replacing W^{5+} (r = 62 pm [98]) by slightly larger Ta^{5+} (r = 64 pm [98]) the W–O1 bond distance, subtending a narrow angle of 4.2(9)° with the **c**-axis vector gradually increased. The W–O2a bond distance fluctuates close to the mean value of 183.0(8) pm, however, W–O2b is 200(2) pm, and their non-leaner trend is different, leading to almost a linear increase of the averaged W–O bond distance as a direct consequence of the larger Ta^{5+} incorporation into the $K_{0.3}(W^{6+}_{0.7}W^{5+}_{0.3})O_3$ bronze. Both the inter-octahedral W–O1–W and W–O2–W angles decrease (Table 4.5). Robinson et al. [113] introduced octahedral mean quadratic elongation (λ_{oct}) for distorted octahedra. It measures the polyhedral distortion which is independent of the polyhedral effective size. The octahedral mean quadratic elongations for $K_{0.3}(W^{6+}_{0.7}W^{5+}_{0.3-y}Ta^{5+}_{y})O_3$ series decreases with successive dilution of W^{5+} by Ta^{5+} as seen in Table 4.5. The gradual expansion of the averaged W–O bond lengths and decrease of the W–O–W angles result in change of the magnitude and direction of the out-of-center distortion of the MO_6 octahedra.

Table 4.5. Selected bond distances, angles, octahedral mean quadratic elongation and out-of-center octahedral distortion of $K_{0.3}(W^{6+}_{0.7}W^{5+}_{0.3-y}Ta^{5+}_{y})O_3$, HTB-I and HTB-II^{m} (*italics*) obtained from powder X-ray diffraction data Rietveld refinements.

y	W–O1 /pm	W–O2a /pm	W–O2b /pm	W–O1–W /°	W–O2–W/°	λ_{oct}	Δ_d /10^{-10} m
0.00	188.8(3)	181.6(5)	201.1(7)	176.19(1)	150.8(3)	1.0119	0.39
0.05	189(4)	183.6(9)	197.6(9)	176.93(1)	152.5(4)	1.0145	0.28
0.10	189.4(3)	182.6(8)	201.3(8)	170.49(1)	149.1(5)	1.0091	0.38
0.15	190.5(3)	183(1)	201(1)	165.05(1)	148.7(6)	1.0076	0.38
0.20	191.8(4)	183(2)	201(2)	161.57(1)	148.3(9)	1.0069	0.37
0.25	191.0(9)	184(3)	198(3)	169.29(1)	149(2)	1.0055	0.33
0.30	193.90(32)	183(2)	201(2)	164.163(2)	145.38(94)	1.0058	0.34
0.10	*191(2)*	*175(7)*	*217(7)*	*174.663(9)*	*140(4)*	*1.0284*	*0.85*
0.15	*198(1)*	*178(4)*	*204(4)*	*150.054(5)*	*148(3)*	*1.0087*	*0.53*
0.20	*191.73(61)*	*176(3)*	*219(3)*	*171.254(4)*	*137(2)*	*1.0295*	*0.86*
0.25	*192.49(55)*	*179(3)*	*212(3)*	*169.249(3)*	*139(2)*	*1.0191*	*0.65*

Halasyamani [114] quantified the magnitude of such distortions by taking into account six intra-octahedral M–O bond lengths as well as deviations three trans O–M–O bond angles from 180°. He coined intra-octahedral distortion index (Δ_d) to describe the acentric displacement of the central M-cation toward edge, face or corner, respectively possesses local C_2, C_3 or C_4 symmetry of the MO_6 octahedron. Based on a statistical survey Halasyamani [114] categorized Δ_d as weak (Δ_d = 0.05 – 0.40), moderate (Δ_d = 0.40 – 0.80) and strong (Δ_d > 0.8) distortions, and some second-order Jahn-Teller (SOJT) distortion susceptible cations follow an average order of $Mo^{6+} > V^{5+} > W^{6+} > Nb^{5+} > Ta^{5+} > Ti^{4+}$. The absolute magnitude of Δ_d of the reported d^0 cations may change (reduce) without the influence of the neighboring lone electron pair cations. As such the WO_6 octahedra of the parent $K_{0.3}(W^{6+}_{0.7}W^{5+}_{0.3})O_3$ bronze possesses Δ_d = 0.39, indicating to a weak distortion. Due to SOJT distortion, W^{6+} has equal possibility of showing distortions either C_2 or C_3 directions. Since 30 % of the W-position is occupied by $W^{5+}(d^1)$, which is not SOJT susceptible rather a pseudo-first-order Jahn-Teller (FOJT) distortion [115] leading to C_4 distortion, WO_6 octahedra prefers C_2 distortion. Thus substitution of W^{5+} with SOJT susceptible $Ta^{5+}(d^0)$ is assumed to incorporate

additional distortion to MO_6 octahedra (Table 4.5). Since Ta^{5+} is also a weak distorter, the Δ_d fluctuates within a narrow range between 0.4 and 0.3 (Table 4.5). The bond valence parameter [116] for W^{6+}–O (192.1 pm) and Ta^{5+}–O (192.0 pm) distances are almost identical, both of which are 3 pm greater than that of W^{5+}–O distance (189 pm). Therefore, the system prefers the Ta^{5+} cation substitution by the expense of SOJT distortion leading to release the bond valence sum (BVS) discrepancy [117] from the theoretical BVS of W (5.7 v.u.) in the $K_{0.3}(W^{6+}_{0.7}W^{5+}_{0.3})O_3$ bronze.

4.2.3. Raman spectra analysis

The Raman spectra of composition (y) dependent Ta^{5+} substituted K-HTB bronzes at room-temperature are given in Figure 4.8. For the direct comparison, the Raman spectrum of $K_{0.3}(W^{6+}_{0.7}W^{5+}_{0.3})O_3$ bronze recorded at room temperature is also included in the Figure 4.8. In spite of their different chemical compositions, considerable influences on the crystal structure, all the products of this series have similar Raman spectra. In particularly, the vibrational properties depend on the variation of Ta composition; some of the lower-wavenumbers modes disappear due to overlapping vibration with the change of chemical composition. A significant shifting of the higher-wavenumber modes were observed because of Ta substitution instead of tungsten. The common feature for each sample is the presence of the 850 cm^{-1} – 1050 cm^{-1} bands, an indication of terminal W=O bonds. Raman peaks observed in the range of 80 cm^{-1} to 1050 cm^{-1} Raman shift given in Figure 4.8 can be divided into three parts; 850 cm^{-1} – 1050 cm^{-1}, 530 cm^{-1} – 820 cm^{-1} and below 500 cm^{-1}. In the first range the Raman peaks appeared due to the stretching vibrations of the terminal M=O (M = W, Ta) bonds [112]. The numbers of observed bands are two or three and strongly dependent on the W^{6+}/W^{5+} and Ta^{5+} composition. These bands are successively becoming broad due to incorporation of Ta. It suggests that Ta and W are statistically distributed in the same chemical compound. The broadening of the terminal Raman bands is an indication of the presence of both W=O and Ta=O groups. In the second region (530 cm^{-1} – 820 cm^{-1}), the Raman peaks were observed due to the stretching modes of W–O bonds [112]. There are four/five observable bands in this region. They are broad and diffuse bands but successively becoming intense. Such broadness is an indication of compound peaks formed from all possible stretching vibrations of W–O–M (M = $W^{6+}/W^{5+}/Ta^{5+}$) bonds. The numbers of bands

for W–O stretching modes were increased in the 530 cm^{-1} – 820 cm^{-1} region, the Raman peaks at 696 cm^{-1} and 757 cm^{-1} are becoming more intense and gradually moved towards the higher wavenumber due successive incorporation of Ta^{5+} cation in the system.

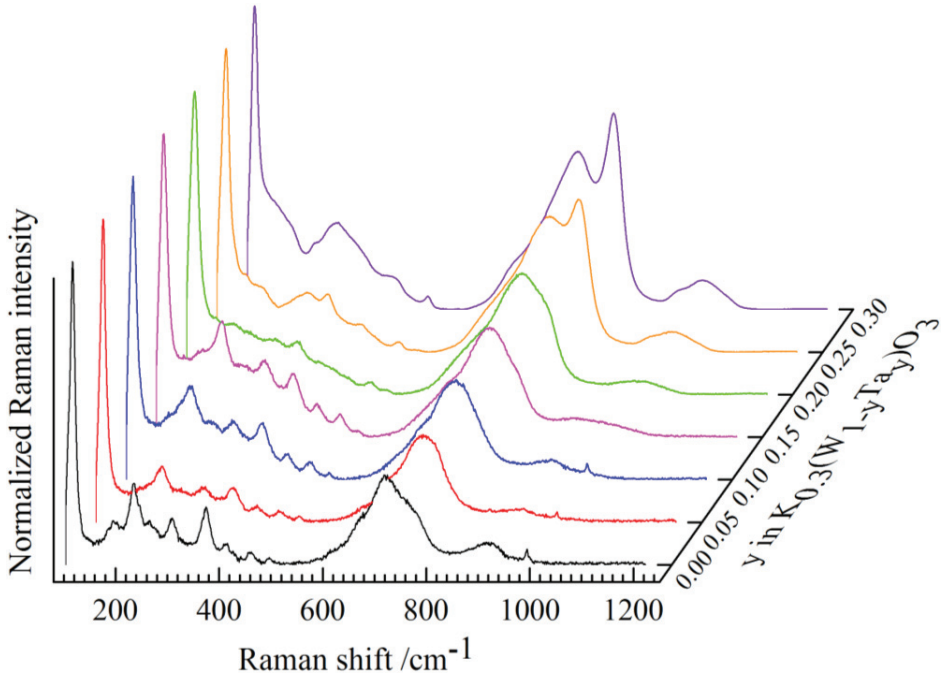

Figure 4.8. Raman spectra of polycrystalline tantalum substituted hexagonal potassium tungsten bronzes, $K_{0.3}(W^{6+}_{0.7}W^{5+}_{0.3-y}Ta^{5+}_{y})O_3$ solid solution series.

There are four observable strong bands (627 cm^{-1}, 700 cm^{-1}, 845 cm^{-1} and 906 cm^{-1}) for different stretching modes of vibrations of Ta_2O_5. on the other hand, $K_{0.3}(W^{6+}_{0.7}W^{5+}_{0.3})O_3$ bronze shows seven bands at 614 cm^{-1}, 645 cm^{-1}, 696 cm^{-1}, 753 cm^{-1}, 879 cm^{-1}, 902 cm^{-1} and 970 cm^{-1} for different stretching modes. The Ta–O stretching bands along with the W–O stretching vibrational bands maybe led to more number of bands in the second region. In the third region, the bending and lattice modes are to be found. The phonon modes with frequencies < 500 cm^{-1} are due to bending modes of vibrations of O–W/Ta–O bonds and those which are below 200 cm^{-1} due to W/Ta–O–W/Ta bending modes of vibrations [106]. The characteristics bands of K–O bonds are located in the very low wavenumber region because the K–O bonds are larger than usual K–O bond distances. Previously it was found at 60 cm^{-1} and 97 cm^{-1} [109] in the $K_{0.3}WO_3$ bronze, below the detection limit (≤ 80 cm^{-1}) of this instrument.

4.2.4. MIR spectra analysis

The mid-infrared (MIR) spectra of the $K_{0.3}(W^{6+}_{0.7}W^{5+}_{0.3-y}Ta^{5+}_{y})O_3$ solid solution series are given in Figure 4.9. For direct comparison, the MIR spectrum of $K_{0.3}(W^{6+}_{0.7}W^{5+}_{0.3})O_3$ bronze is also included in the Figure 4.9. The spectrum of $K_{0.3}(W^{6+}_{0.7}W^{5+}_{0.3})O_3$ bronze consists of a weak broad phonon absorption band below 1000 cm^{-1}, which is related to the surface effects of the tungsten oxide containing compounds.

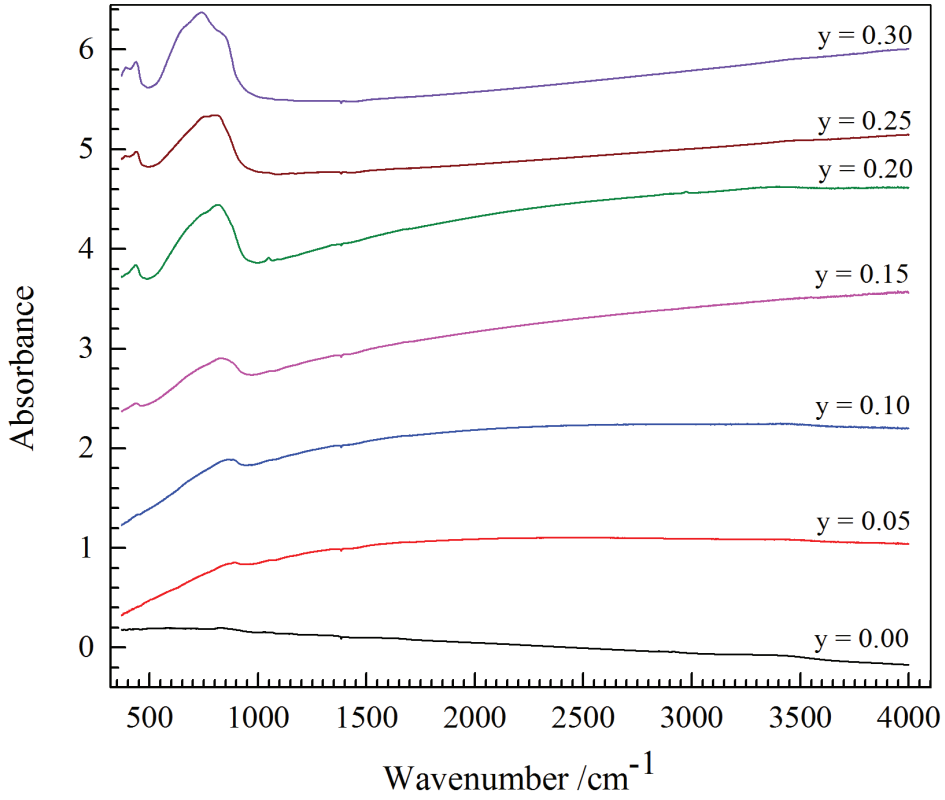

Figure 4.9. MIR spectra of tantalum substituted hexagonal potassium tungsten bronzes, $K_{0.3}(W^{6+}_{0.7}W^{5+}_{0.3-y}Ta^{5+}_{y})O_3$ solid solution series.

The broad MIR absorption peaks in the region of 500 cm^{-1} – 980 cm^{-1} were appeared as a result of the stretching modes of MO_6 (M = W, Ta) octahedra. The absorption peaks below 480 cm^{-1} is likely to be due to the bending mode of M–O–M groups. The intensity of absorption bands have been increased with increasing Ta concentration in the materials. It indicates that the number of free carrier in the system decreases due to the replacement of $W^{5+}(d^1)$ cations by $Ta^{5+}(d^0)$ cations. The observed MIR spectra are similar with the data

reported by Dey et al. [111] for the $Cs_{0.25}(W_{1-y}Nb_y)O_3$ and $Cs_{0.3}(W_{1-y}Nb_y)O_3$ series. There is no absorption peak above 1000 cm^{-1} till 4000 cm^{-1} wavenumbers. It indicates that all these compounds in the $K_{0.3}(W^{6+}_{0.7}W^{5+}_{0.3-y}Ta^{5+}_{y})O_3$ solid solution series are transparent for MIR radiation in the range of 1000 cm^{-1} to 4000 cm^{-1} wavenumbers.

4.3. $K_{0.3}(W^{6+}_{0.7}W^{5+}_{0.3-y}V^{5+}_{y})O_3$ solid solution series

Polycrystalline powder samples of $K_{0.3}(W^{6+}_{0.7}W^{5+}_{0.3-y}V^{5+}_{y})O_3$ solid solution series were characterized by powder X-ray diffraction, SEM/EDX, Raman and Fourier transform infrared (FTIR) spectroscopy.

4.3.1. SEM/EDX analysis

The scanning electron microscopy (SEM) photographs of all the samples were recorded; it shows that the crystallinity of the products is poor as shown in Figure 4.10. The crystallinity of V^{5+} substituted $K_{0.3}(W^{6+}_{0.7}W^{5+}_{0.3-y}V^{5+}_{y})O_3$ series is better than that of $K_{0.3}(W^{6+}_{0.7}W^{5+}_{0.3-y}Ta^{5+}_{y})O_3$ series, though there was no good quality crystals, suitable for collecting single crystal X-ray diffraction data. The observed EDX results are given in Table 4.6. The EDX results show the potassium content is close to the nominal compositions for all these samples. The V^{5+} cations are statistically distributed in the polycrystalline products. The averaged K:W and V:W ratios of this series are also in good agreement with nominal compositions.

Table 4.6. SEM/EDX results of $K_{0.3}(W^{6+}_{0.7}W^{5+}_{0.3-y}V^{5+}_{y})O_3$ solid solution series.

y	K/W		V/W	
	Used	Observed	Used	Observed
0.00	0.300	0.374(42)	-	-
0.05	0.316	0.296(20)	0.053	0.053(3)
0.08	0.326	0.314(8)	0.087	0.086(2)
0.10	0.333	0.333(15)	0.111	0.108(4)
0.13	0.345	0.336(19)	0.149	0.184(3)
0.15	0.353	0.337(4)	0.176	0.174(5)

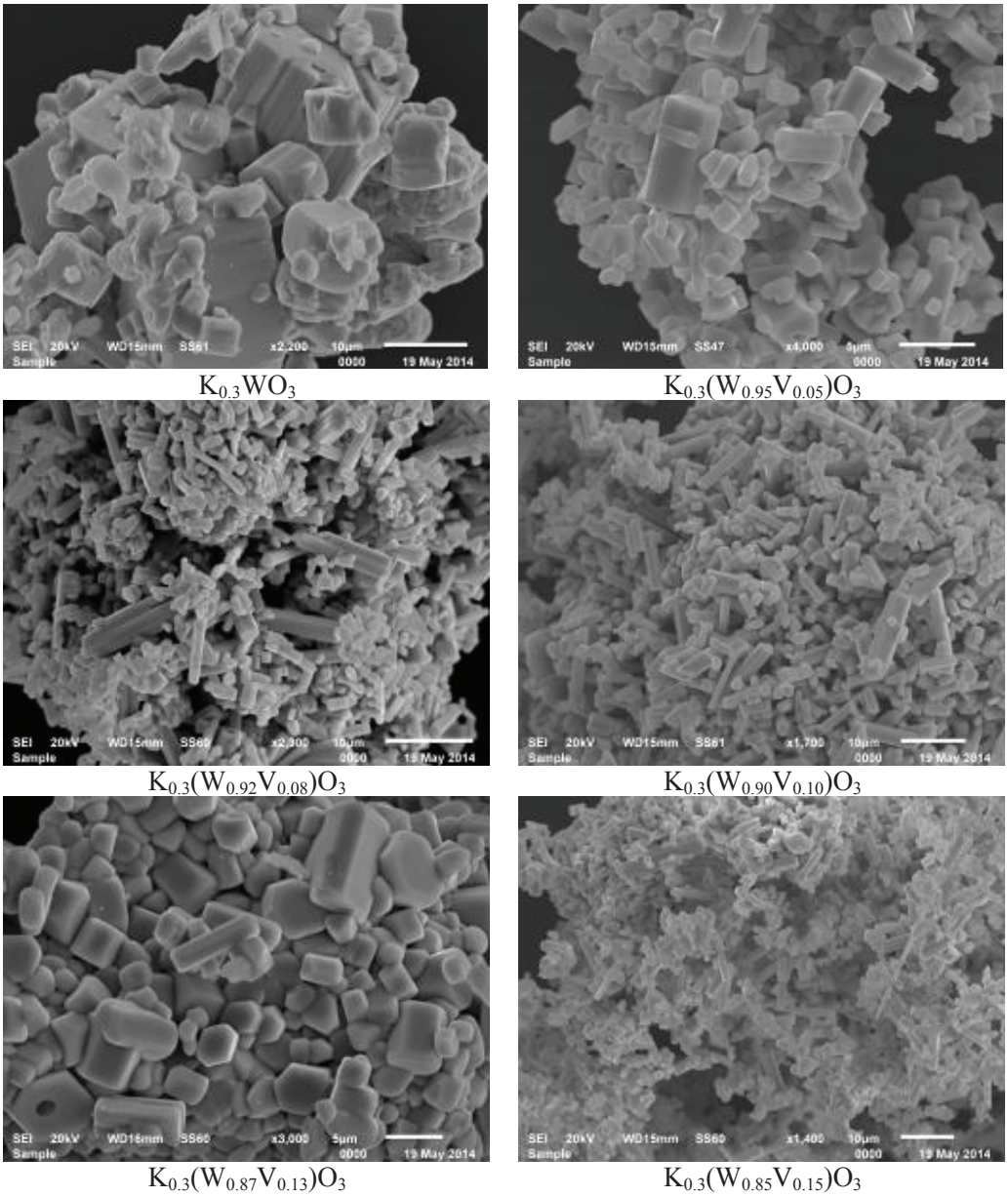

Figure 4.10. SEM micrographs of $K_{0.3}(W^{6+}_{0.7}W^{5+}_{0.3-y}V^{5+}_{y})O_3$ solid solution series.

4.3.2. Powder X-ray diffraction data investigation

Additional attempts were made for the successive replacement of W^{5+} by V^{5+} cations in the $K_{0.3}(W^{6+}_{0.7}W^{5+}_{0.3-y}V^{5+}_{y})O_3$ solid solution series up to the limit of the miscibility range. The parent $K_{0.3}(W^{6+}_{0.7}W^{5+}_{0.3})O_3$ bronze is deep blue colored due to W^{5+} cations in the structure. Successive dilution of W^{5+} by V^{5+} cations changed the color in the order: deep blue (y = 0) → light blue (y = 0.05 – 0.08) → brownish-blue (y = 0.1) → brown (y = 0.15) for the decreasing

amount of W^{5+} (blue) color centers with a subsequent dominance of V^{5+} (yellow). Powder X-ray diffraction data Rietveld refinements confirmed that $K_{0.3}(W^{6+}_{0.7}W^{5+}_{0.3-y}V^{5+}_{y})O_3$ bronze produce pure HTB-type phase in the space group $P6_322$ up to y = 0.15. For y > 0.15 a mixture of two phases was observed; V^{5+} substituted potassium tungsten bronze phase along with non-bronze impurity phases (mainly vanadium oxides). Figure 4.11 shows the powder XRD patterns of $K_{0.3}(W^{6+}_{0.7}W^{5+}_{0.3-y}V^{5+}_{y})O_3$ solid solution series.

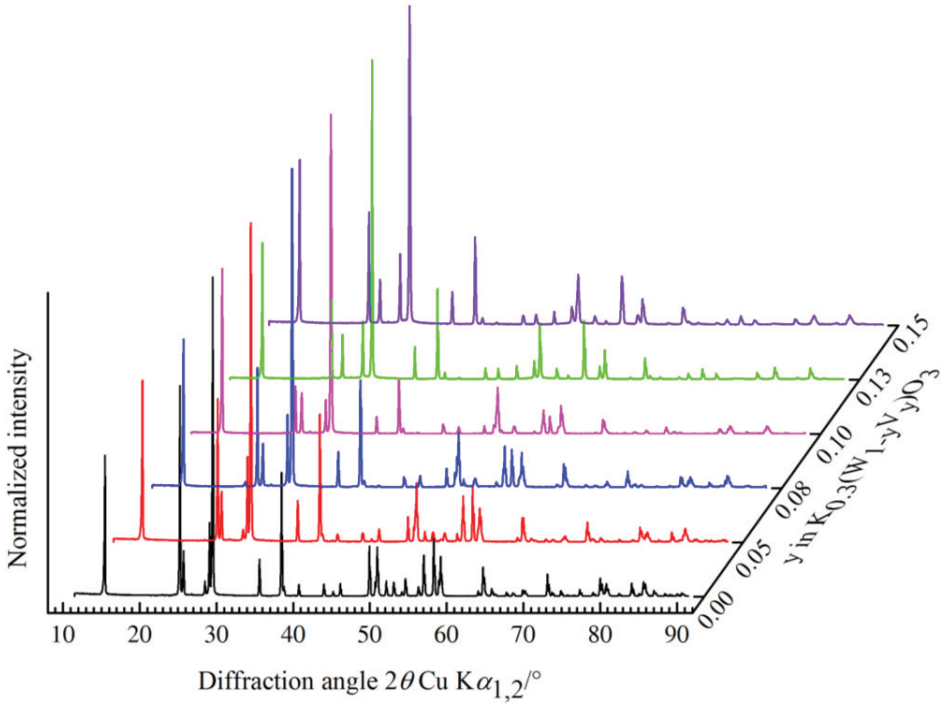

Figure 4.11. Powder X-ray diffraction patterns of $K_{0.3}(W^{6+}_{0.7}W^{5+}_{0.3-y}V^{5+}_{y})O_3$ solid solutions series.

Detailed structural parameters of vanadium substituted K-HTB is given in Table 4.7. Selected interatomic distances and angles, octahedral mean quadratic elongation (λ_{oct}) [113, 118] and out-of-center octahedral distortion (Δ_d) [114] are given in Table 4.8. An anisotropic behavior of the lattice parameters is observed with an increase of vanadium concentration as shown in Figure 4.12(a). That is, the *a*-cell parameter decreased followed by increase of the *c*-cell parameter with increasing vanadium concentration in the system, leading to an overall contraction of the cell volume. The anisotropy factor $A = |a - c|$, shown in Figure 4.12(b), increases with a steep slope at y = 0.15. The smaller ionic radius of V^{5+} (r = 54 pm [98]) compare to that of W^{5+} (r = 62 pm [98]) might limit the substitution to y = 0.15. Substitution

of W^{5+} by much smaller V^{5+} cations leads to the massive contraction of the cell volume as shown in Figure 4.12(c). This observation supports the results observed by Abdullah et al. [40] who reported a pure single phase solid solution up to y = 0.15. The W–O1 bond distances along the **c**-axis increase up to y = 0.15.

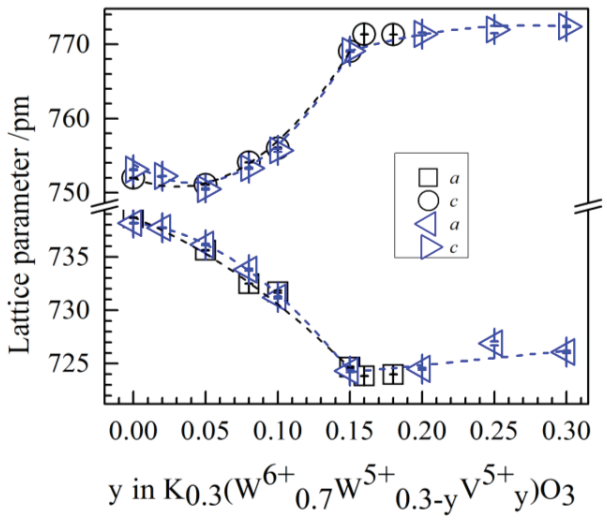

Figure 4.12(a). Change of lattice parameters with respect to vanadium composition (y) in the $K_{0.3}(W^{6+}_{0.7}W^{5+}_{0.3-y}V^{5+}_{y})O_3$ bronzes. Data from ref. [40] (triangle) are plotted for comparison.

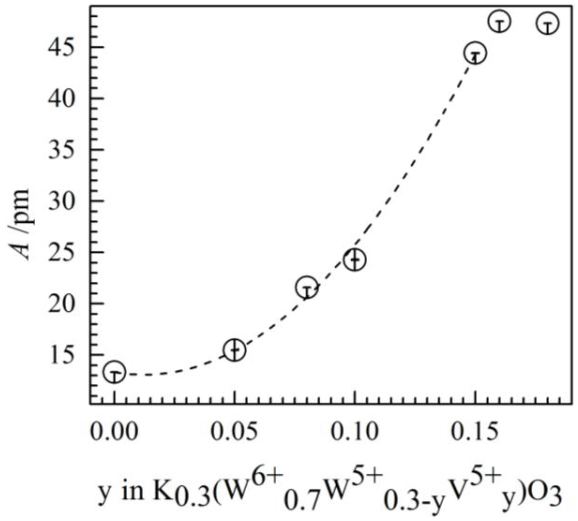

Figure 4.12(b). Change of anisotropy factor (*A*) with respect to vanadium composition (y) of $K_{0.3}(W^{6+}_{0.7}W^{5+}_{0.3-y}V^{5+}_{y})O_3$ bronzes.

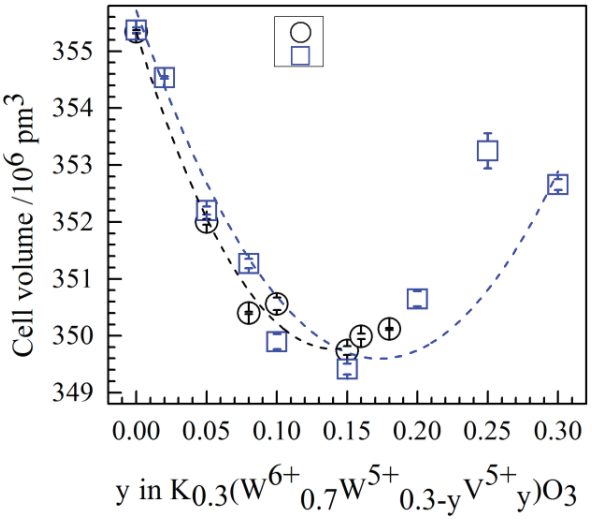

Figure 4.12(c). Change of cell volume with respect to vanadium composition (y) of $K_{0.3}(W^{6+}_{0.7}W^{5+}_{0.3-y}V^{5+}_{y})O_3$ bronzes. Data from ref. [40] are plotted for comparison. Circle and square refer to this study and ref. [40], respectively.

Table 4.7. Details of the crystal structure of $K_{0.3}(W^{6+}_{0.7}W^{5+}_{0.3-y}V^{5+}_{y})O_3$ bronzes obtained from powder X-ray diffraction data Rietveld refinements.

y	*a* /pm	*c* /pm	W(*x*)	O1(*x*)	O2(*x*)	O2(*y*)	O2(*z*)	K(*z*)
0.00	738.67(3)	751.99(3)	0.4780(1)	0.4951(26)	0.4287(6)	0.2164(7)	0.0229(14)	0.1909(11)
0.05	735.62(4)	751.10(5)	0.4828(1)	0.5041(46)	0.4255(9)	0.2173(12)	0.9682(15)	0.2048(20)
0.08	732.49(2)	754.09(3)	0.4939(4)	0.5102(49)	0.4197(35)	0.2100(37)	0.9769(53)	0.2222(75)
0.10	731.73(11)	756.01(11)	0.4998(22)	0.5035(69)	0.4267(20)	0.1974(78)	0.9604(26)	0.1951(21)
0.13	725.79(4)	769.37(4)	0.4992(13)	0.5048(34)	0.4338(11)	0.2001(38)	0.9625(13)	0.1971(13)
0.15	724.65(7)	769.06(8)	0.5004(11)	0.5039(50)	0.4373(15)	0.1854(27)	0.9588(17)	0.1938(16)
0.16	723.83(2)	771.34(3)	0.4967(11)	0.5263(29)	0.4505(27)	0.2020(41)	0.9637(34)	0.2083(54)
0.18	723.98(1)	771.31(2)	0.4973(8)	0.5217(26)	0.4487(23)	0.1971(28)	0.9670(31)	0.2039(43)

Table 4.8. Selected bond distances, angles, octahedral mean quadratic elongation and out-of-center octahedral distortion of $K_{0.3}(W^{6+}_{0.7}W^{5+}_{0.3-y}V^{5+}_{y})O_3$ bronzes obtained from powder X-ray diffraction data Rietveld refinements.

y	W–O1 /pm	W–O2a /pm	W–O2b /pm	W–O1–W /°	W–O2–W /°	λ_{oct}	Δ_d /10^{-10} m
0.00	188.8(3)	181.6(5)	201.1(7)	176.19(1)	150.8(3)	1.0119	0.39
0.05	188.3(4)	186.1(8)	197.3(8)	176.82(1)	147.9(5)	1.0116	0.22
0.08)	189.0(4)	188(3)	194(3)	172.15(1)	147(1)	1.0019	0.12
0.10	189.1(2)	180(4)	202(4)	177.31(1)	146(2)	1.0162	0.45
0.13	192.4(1)	176(2)	201(2)	176.44(4)	149(1)	1.0168	0.49
0.15	192.3(2)	165(2)	211(2)	177.01(1)	148.3(9)	1.0295	0.92
0.16	195.7(6)	168(3)	204(3)	160.60(1)	154(2)	1.0217	0.72
0.18	194.8(5)	165(2)	206(2)	163.90(1)	154(1)	1.0217	0.82

The difference between two types of W–O2 distances, lying almost in the *ab*-plane, increased, that is, two shorter W–O2a distances contracted and two longer W–O2b distances further increased with respect to the degree of substitution with V^{5+} cations (Table 4.8). The W–O1–W and W–O2–W angles changed in a cooperative manner leading to increase the *c*-cell parameter and decrease the *a*-cell parameter. Since V^{5+} is a strong distorter, even stronger than W^{6+}, it is therefore clear that the MO_6 octahedra in the $K_{0.3}(W^{6+}_{0.7}W^{5+}_{0.3-y}V^{5+}_{y})O_3$ system

develops the magnitude of Δ_d with increasing y; the weakly distorted parent system transformed into a HTB containing strongly distorted MO_6 octahedra for y = 0.15 (Table 4.8). A further V^{5+} substitution led to forming HTB bronze, however, together with V_2O_5 where V^{5+} is five coordinated [119] – a consequence of very high Δ_d of 1.48 considering a long V–O distance of 279 pm for VO_6 octahedron.

4.3.3. Raman spectra analysis

The Raman spectra of $K_{0.3}(W^{6+}_{0.7}W^{5+}_{0.3-y}V^{5+}_{y})O_3$ (y = 0 – 0.15) solid solution series are given in Figure 4.13. It shows that the observed Raman spectra of vanadium containing bronzes are different than that of the parent $K_{0.3}(W^{6+}_{0.7}W^{5+}_{0.3})O_3$ bronze. Especially, the vibrational bands depend on the variation of y-composition; some of the lower-wavenumbers modes disappeared due to overlapping vibration which strongly dependent on the chemical composition. A significant shifting of the higher-wavenumber modes were observed because of successive incorporation of V into the system. Each sample shows a general feature in the 850 cm^{-1} – 1050 cm^{-1} Raman shift region, the existence of a numbers of bands due to possible stretching modes of vibrations within MO_6 octahedra. The observed Raman peaks in the range of 80 cm^{-1} to 1100 cm^{-1} Raman shift given in the Figure 4.13 can be divided into two broad regions; 525 cm^{-1} – 1100 cm^{-1} and below 500 cm^{-1} Raman shift. In the first range only the stretching vibrations from all possible modes (M=O and M–O where M = W, V) are observed. The numbers of bands are five to seven in this region and strongly dependent on the concentration of the W^{6+}/W^{5+}, V^{5+} cations. These bands are broad and gradually becoming intense due to the dilution of W^{5+} cations in the system. This indicates that V and W are statistically distributed in the same chemical species. The observed Raman peaks originated from the stretching modes of vibrations have been shifted towards higher Raman shift due to successive incorporation of V. In the second region, the Raman peaks are observed because of bending vibrations of W/V–O–W/V and O–W/V–O bridging bonds. The phonon modes with frequencies < 500 cm^{-1} are due to bending modes of vibrations of O–W/V–O bonds and those which are below 200 cm^{-1} because of W/V–O–W/V bridging bonds. The characteristics peaks associated with the mode of K–O bonds are located in the very low wavenumber region as earlier report proposed at 60 cm^{-1} and 97 cm^{-1} [109] for $K_{0.3}WO_3$ bronze. Since in the tungsten

bronzes, the K–O interatomic distances are larger than typical K–O bond distance, it is expected that the bands related to K–O bond to be found in the very low Raman shift region.

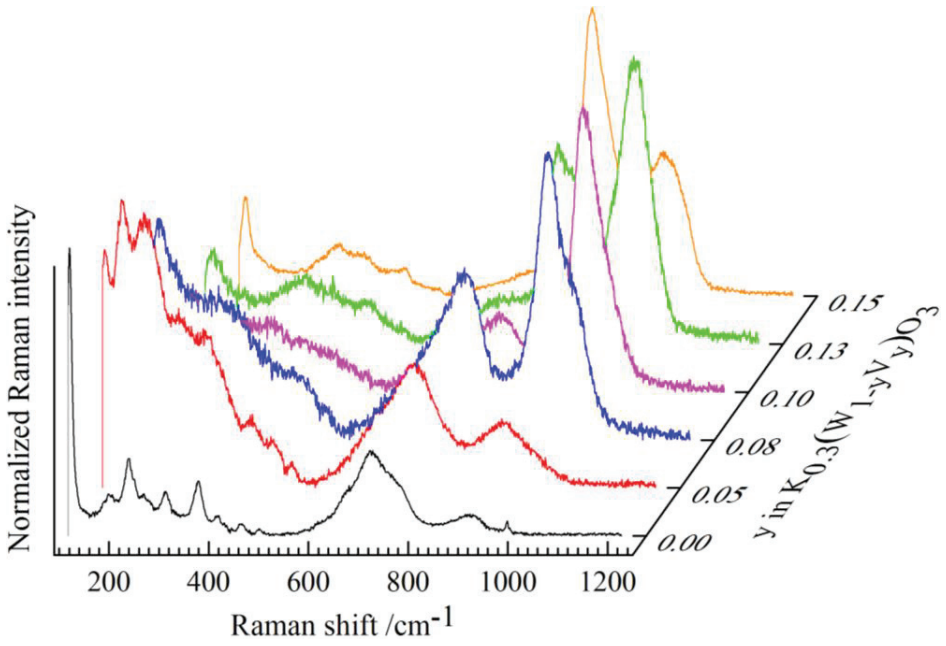

Figure 4.13. Raman spectra of vanadium substituted hexagonal potassium tungsten bronzes, $K_{0.3}(W^{6+}_{0.7}W^{5+}_{0.3-y}V^{5+}_{y})O_3$ series.

4.3.4. MIR spectra analysis

The mid-infrared (MIR) spectra of $K_{0.3}(W^{6+}_{0.7}W^{5+}_{0.3-y}V^{5+}_{y})O_3$ solid solution series were also recorded at room-temperature. Figure 4.14 shows the MIR spectra of these solid solution series. The spectrum of $K_{0.3}(W^{6+}_{0.7}W^{5+}_{0.3})O_3$ bronze is also included in the Figure 4.14. The spectrum of $K_{0.3}(W^{6+}_{0.7}W^{5+}_{0.3})O_3$ bronze consists of weak broad phonon absorption band below 1000 cm^{-1} wavenumber, which is usually found due to the surface effects of the tungsten oxide containing compounds. The broad MIR absorption peaks in the region of 500 cm^{-1} – 1050 cm^{-1} are observed because of stretching modes of MO_6 (M = W, V) octahedra present in the $K_{0.3}(W^{6+}_{0.7}W^{5+}_{0.3-y}V^{5+}_{y})O_3$ bronzes. The absorption peaks below 460 cm^{-1} is likely to be due to the bending mode of M–O–M bridging bonds. The intensity of the absorption bands gradually increased with successive dilution of W^{5+} and incorporation of V^{5+} cations in the compounds. It suggests that the numbers of free carrier decreases due to replacement of $W^{5+}(d^1)$ by $V^{5+}(d^0)$ cations. The observed MIR spectra are comparable with

the results found by Dey et al. [111] for the $Cs_{0.25}W_{1-y}Nb_yO_3$ and $Cs_{0.3}W_{1-y}Nb_yO_3$ series. In the higher wavenumbers region (> 1050 cm^{-1}) there is no absorption peak. It indicates that the synthesized products are transparent for MIR radiation in the range of 1050 cm^{-1} to 4000 cm^{-1} wavenumbers.

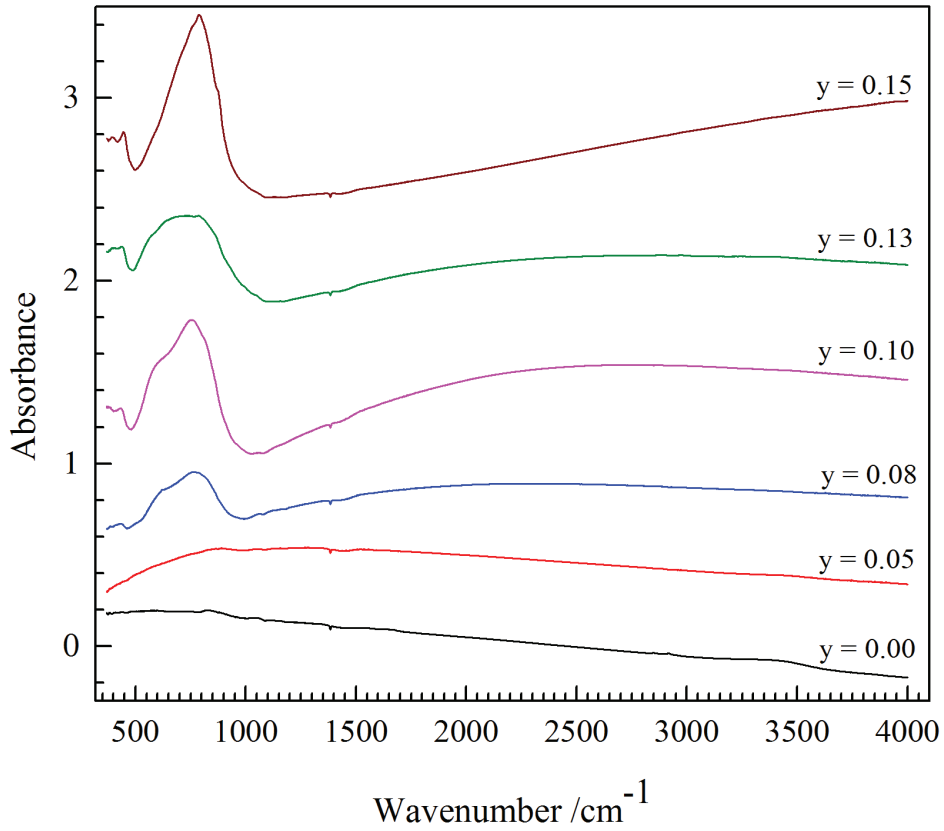

Figure 4.14. MIR spectra of vanadium substituted hexagonal potassium tungsten bronzes, $K_{0.3}(W^{6+}_{0.7}W^{5+}_{0.3-y}V^{5+}_{y})O_3$ solid solution series.

4.4. $K_{0.3}(W^{6+}_{0.7}W^{5+}_{0.3-y}Ta^{5+}_{y/2}V^{5+}_{y/2})O_3$ solid solution series

Polycrystalline powder samples of $K_{0.3}(W^{6+}_{0.7}W^{5+}_{0.3-y}Ta^{5+}_{y/2}V^{5+}_{y/2})O_3$ series were characterized by powder X-ray diffraction, SEM/EDX, Raman and FTIR spectroscopy.

4.4.1. SEM/EDX analysis

Scanning electron microscopy (SEM) images of $K_{0.3}(W^{6+}_{0.7}W^{5+}_{0.3-y}Ta^{5+}_{y/2}V_{y/2})O_3$ solid solution series show that the crystallinity of these materials is also poor as shown in Figure 4.15. Agglomerations of the polycrystalline products were observed. The EDX results showed

that the potassium content is close to the used nominal composition. Both Ta and V are statistically distributed along with tungsten in the polycrystalline products. The averaged K:W, Ta:V and (Ta+V):W ratios are also in good agreement with the nominal compositions. The observed EDX results are given in Table 4.9.

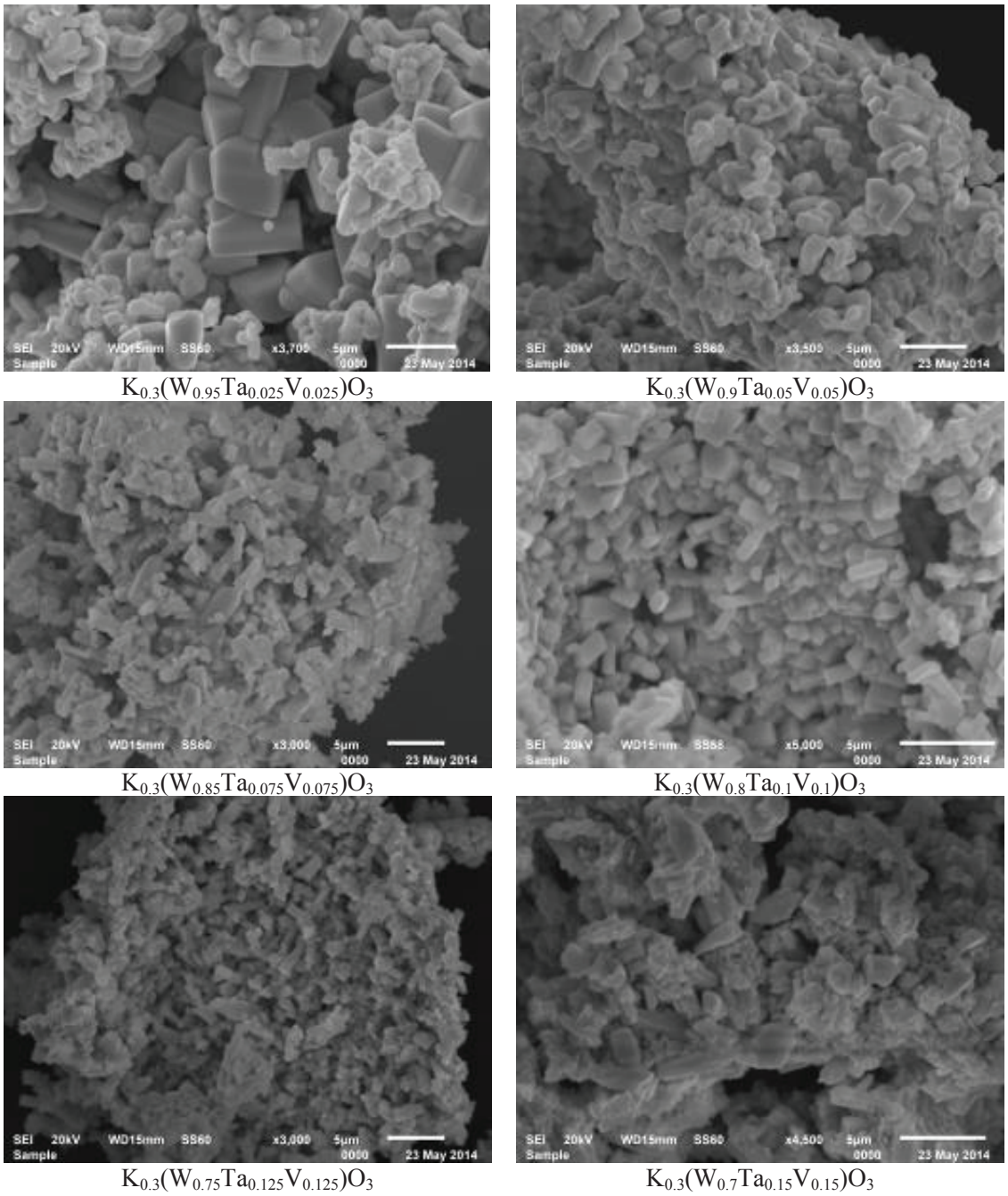

$K_{0.3}(W_{0.95}Ta_{0.025}V_{0.025})O_3$ $K_{0.3}(W_{0.9}Ta_{0.05}V_{0.05})O_3$

$K_{0.3}(W_{0.85}Ta_{0.075}V_{0.075})O_3$ $K_{0.3}(W_{0.8}Ta_{0.1}V_{0.1})O_3$

$K_{0.3}(W_{0.75}Ta_{0.125}V_{0.125})O_3$ $K_{0.3}(W_{0.7}Ta_{0.15}V_{0.15})O_3$

Figure 4.15. SEM micrographs of $K_{0.3}(W^{6+}_{0.7}W^{5+}_{0.3-y}Ta^{5+}_{y/2}V_{y/2})O_3$ solid solution series.

Table 4.9. SEM/EDX results of $K_{0.3}(W^{6+}_{0.7}W^{5+}_{0.3-y}Ta^{5+}_{y/2}V_{y/2})O_3$ solid solution series.

y	K/W		Ta/V		(Ta+V)/W	
	Used	Observed	Used	Observed	Used	Observed
0.05	0.316	0.315(11)	1	1.03(19)	0.053	0.063(13)
0.10	0.333	0.339(11)	1	1.01(11)	0.111	0.104(7)
0.15	0.353	0.334(20)	1	1.00(10)	0.176	0.171(7)
0.20	0.375	0.344(42)	1	1.09(13)	0.250	0.242(12)
0.25	0.400	0.355(41)	1	1.09(12)	0.333	0.302(5)
0.30	0.428	0.404(21)	1	1.13(15)	0.428	0.376(4)

4.4.2. Powder X-ray diffraction data investigation

A series of $K_{0.3}(W^{6+}_{0.7}W^{5+}_{0.3-y}Ta^{5+}_{y/2}V^{5+}_{y/2})O_3$ (y = 0 – 0.3) samples was prepared to investigate the co-sharing effects of larger (Ta^{5+}) and smaller (V^{5+}) cations on the metal position (M) in the MO_6 octahedral positions of the K-HTB structure. Figure 4.16 shows the XRD patterns of the $K_{0.3}(W^{6+}_{0.7}W^{5+}_{0.3-y}Ta^{5+}_{y/2}V^{5+}_{y/2})O_3$ solid solution series.

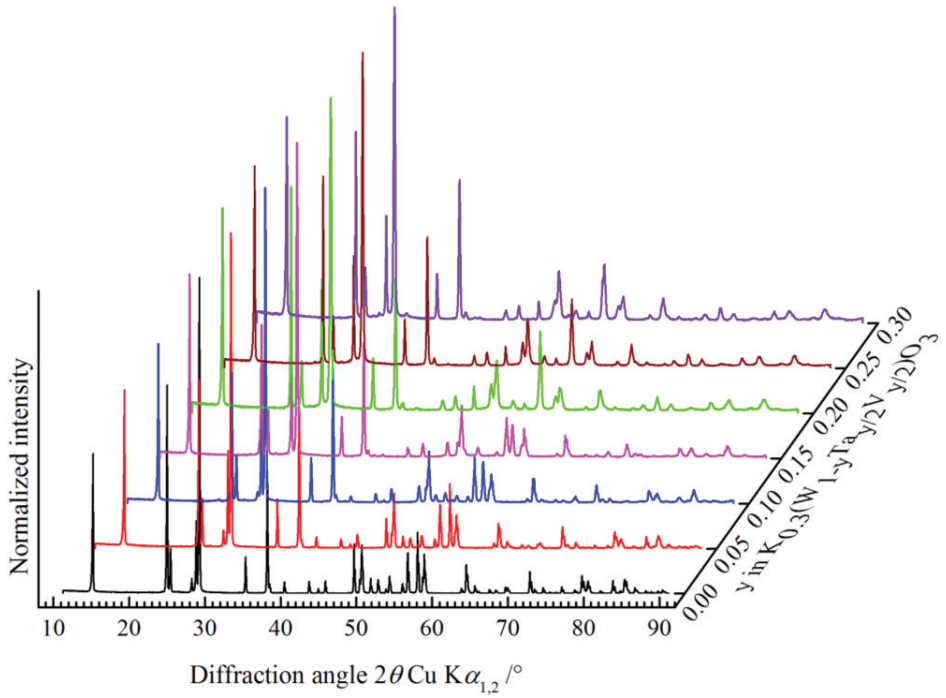

Figure 4.16. Powder X-ray diffraction patterns of $K_{0.3}(W^{6+}_{0.7}W^{5+}_{0.3-y}Ta^{5+}_{y/2}V^{5+}_{y/2})O_3$ solid solution series.

Powder X-ray diffraction data Rietveld refinements showed that each composition of this $K_{0.3}(W^{6+}_{0.7}W^{5+}_{0.3-y}Ta^{5+}_{y/2}V^{5+}_{y/2})O_3$ solid solution series also follow the space group $P6_322$ as same as the parent $K_{0.3}(W^{6+}_{0.7}W^{5+}_{0.3})O_3$ bronze. Whereas the formation of pure single phase samples during the incorporation of Ta^{5+} in the $K_{0.3}(W^{6+}_{0.7}W^{5+}_{0.3-y}Ta^{5+}_{y})O_3$ series is limited to $y < 0.1$ and that of V^{5+} to $y = 0.15$ for $K_{0.3}(W^{6+}_{0.7}W^{5+}_{0.3-y}V^{5+}_{y})O_3$ series their co-sharing on the same Wyckoff position (6*g; x, 0, 0*) allowed for a miscibility of $y = 0.3$ (Ta^{5+} and $V^{5+} = 0.15$ each) in the $K_{0.3}(W^{6+}_{0.7}W^{5+}_{0.3-y}Ta^{5+}_{y/2}V^{5+}_{y/2})O_3$ solid solution series. Therefore, co-doping with vanadium changed the limit of the Ta^{5+}-substitution in the K-HTB to $y = 0.15$ (at minimum). Details of the structural parameters, and selected interatomic distances and angles are given in Table 4.10 and Table 4.11, respectively. With an increase of y the color changes from parent deep-blue ($K_{0.3}WO_3$) to brownish-blue and finally as brown as that of the $K_{0.3}(W^{6+}_{0.7}W^{5+}_{0.15}V^{5+}_{0.15})O_3$ bronze. Alike the Ta^{5+}- and V^{5+}-substituted analogues, the cell parameters follow an anisotropic behavior with increasing y as shown in Figure 4.17(a); the *a*-decreases while the *c*-parameter increases up to $y = 0.2$. Afterward the *a*-cell parameter shows slight increasing behavior, keeping the *c*-cell parameter almost constant. As a consequence, the anisotropy factor, $A = |a - c|$ increases followed by a slight decrease above $y = 0.20$ (Figure 4.17(b)). The cell volume follows a parabolic trend with increasing y as shown in Figure 4.17(c). The average cell volume calculated from the V^{5+} or Ta^{5+} analogues (given as $(V_{Ta}+V_V)/2$ in Figure 4.17(c)) lies close to the observed values. The observation is also in good agreement with the averaged value calculated from Shakil et al. [39] and Abdullah et al. [40]; though both these reports did not mention the respective space group except to indexing the reflections as hexagonal tungsten bronzes structure. Incorporation of bigger Ta^{5+} and smaller V^{5+} cations in the W^{5+} sites in $K_{0.3}(W^{6+}_{0.7}W^{5+}_{0.3})O_3$ structure, respectively, increases and decreases the cell volume. Apparently it seems that up to $y = 0.15$ the size of vanadium and the associated factors (types of M-cations, variation of intra- and inter-octahedral angles, interatomic distances and Δ_d of the WO_6 octahedra) predominates over the respective Ta^{5+} factors which dominate the positive slope of the parabolic curve. When W^{5+} is simultaneously substituted by V^{5+} and Ta^{5+} a possibility arises to fill a single Wyckoff position by four different types of cations (V^{5+}, Ta^{5+}, W^{5+} and W^{6+}), leading to set new SOJT distortion (magnitude of Δ_d) which ultimately limits the range of chemical miscibility. To accommodate the augmented distortion (Table 4.11) exerted by moderate Ta^{5+} and strong V^{5+} SOJT

distorters the system prefers other possible low-energy cost mechanism such as tilting and twisting of the WO_6 octahedra. Such cooperative effects not only change the W–O bond distances but also the W–O–W angles. The overall consequence can be observed in the expansion-contraction behavior of the metric parameters as y increases.

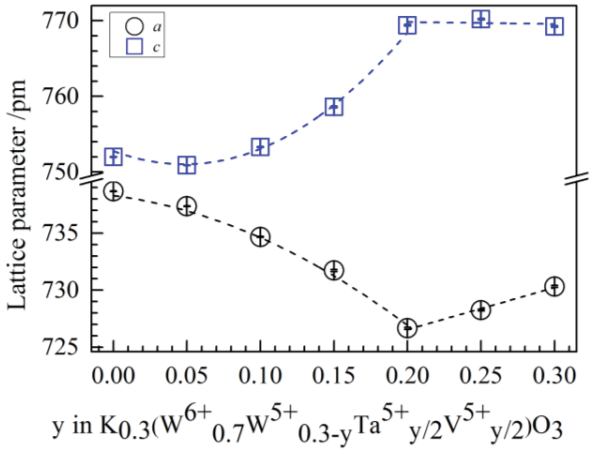

Figure 4.17(a). Change of lattice parameters with respect to Ta and V compositions (y) in the $K_{0.3}(W^{6+}_{0.7}W^{5+}_{0.3-y}Ta^{5+}_{y/2}V^{5+}_{y/2})O_3$ bronzes.

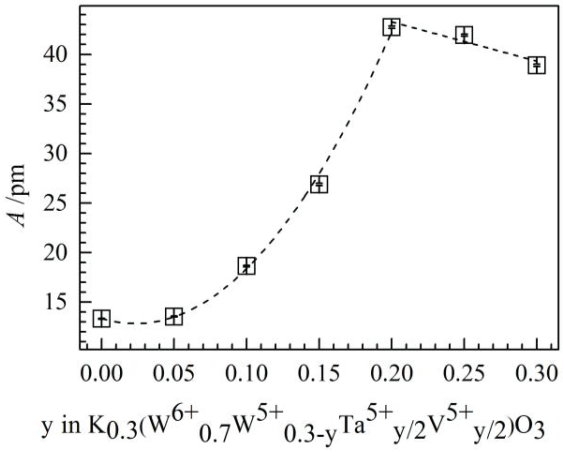

Figure 4.17(b). Anisotropy factor (*A*) of $K_{0.3}(W^{6+}_{0.7}W^{5+}_{0.3-y}Ta^{5+}_{y/2}V^{5+}_{y/2})O_3$ solid solution series.

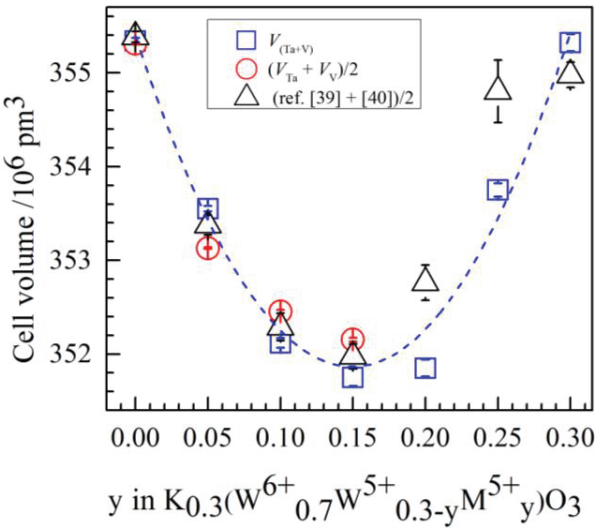

Figure 4.17(c). Change of cell volume with respect to Ta and V composition (y) in the $K_{0.3}(W^{6+}_{0.7}W^{5+}_{0.3-y}Ta^{5+}_{y/2}V^{5+}_{y/2})O_3$ bronzes. The square, circle and triangle refer to simultaneous Ta and V substitution, averaged calculated from individual Ta or V incorporation and the data from ref. [39, 40], respectively.

Table 4.10. Details of the crystal structure of $K_{0.3}(W^{6+}_{0.7}W^{5+}_{0.3-y}Ta^{5+}_{y/2}V^{5}+_{y/2})O_3$ solid solution series obtained from powder X-ray diffraction data Rietveld refinements.

y	*a* /pm	*c* /pm	W(*x*)	O1(*x*)	O2(*x*)	O2(*y*)	O2(*z*)	K(*z*)
0.00	738.67(3)	751.99(3)	0.4780(1)	0.4951(26)	0.4287(6)	0.2164(7)	0.0229(14)	0.1909(11)
0.05	737.35(3)	750.88(3)	0.4785(1)	0.4958(35)	0.4255(6)	0.2154(7)	0.0261(12)	0.2044(15)
0.10	734.67(5)	753.31(5)	0.4843(1)	0.4924(29)	0.4232(8)	0.2160(11)	0.0342(12)	0.2098(20)
0.15	731.71(9)	758.60(9)	0.5000(19)	0.4930(44)	0.4190(12)	0.2224(61)	0.0395(16)	0.2013(21)
0.20	726.66(9)	769.41(9)	0.4992(16)	0.4905(36)	0.4304(11)	0.1964(41)	0.0415(14)	0.2006(18)
0.25	728.25(7)	770.20(7)	0.4993(9)	0.4901(28)	0.4323(11)	0.1884(23)	0.0419(12)	0.1920(15)
0.30	730.33(8)	769.23(8)	0.4994(7)	0.4763(13)	0.4354(11)	0.1788(18)	0.0385(15)	0.1789(15)

Table 4.11. Selected bond distances, angles, octahedral mean quadratic elongation and out-of-center octahedral distortion of $K_{0.3}(W^{6+}_{0.7}W^{5+}_{0.3-y}Ta^{5+}_{y/2}V^{5+}_{y/2})O_3$ solid solution series obtained from powder X-ray diffraction data Rietveld refinements.

y	W–O1 /pm	W–O2a /pm	W–O2b /pm	W–O1–W /°	W–O2–W /°	λ_{oct}	Δ_d /10^{-10} m
0.00	188.8(3)	181.6(5)	201.1(7)	176.19(1)	150.8(3)	1.0119	0.39
0.05	188.5(3)	182.6(5)	200.9(5)	176.78(1)	149.1(3)	1.0113	0.37
0.10	188.9(2)	187.0(7)	197.0(7)	174.13(1)	146.7(4)	1.0098	0.20
0.15	189.9(3)	183(3)	201(3)	174.64(1)	144(2)	1.0121	0.36
0.20	192.7(3)	176(2)	203(2)	172.92(1)	147(1)	1.0155	0.54
0.25	193.0(2)	170(1)	210(1)	172.62(1)	146.9(8)	1.0201	0.79
0.30	194.6(3)	162(1)	217(1)	162.32(1)	148.4(7)	1.0202	1.11

Powder X-ray diffraction data also showed successive broadening of the reflections due to heterotypic atoms (W, Ta, V) present in the same solid solution. The three /four possible atoms of different ionic radii occupy on the same crystallographic sites are producing massive internal distortion among the polyhedra. The resulting materials have poor crystallinity and additional higher internal strain compared to that of $K_{0.3}(W^{6+}_{0.7}W^{5+}_{0.3})O_3$ bronze. The average crystallite sizes are successively decreased, conversely the internal microstrain of the

materials are increased because of Ta^{5+} and V^{5+} cations doping into the parent bronze compound.

Bronzes (reduced phases) are some of a few compounds to study the crystal-chemistry of W^{5+} cations. They share the similar Wyckoff position as of W^{6+} holding octahedral coordination. Incorporating alkali or higher valence cations in the respective channels of the bronzes prevails the opportunity to increase the W^{5+} concentration in the phases. Since W^{5+} is not SOJT distortion susceptible, it is expected that increasing the concentration of W^{5+} cation in the structure would decrease the SOJT distortion, thus decrease the magnitude of Δ_d.

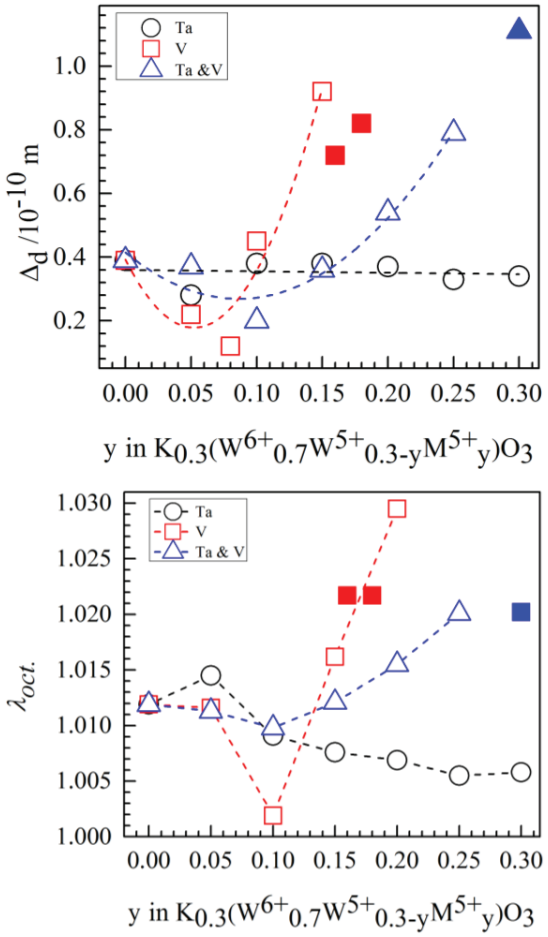

Figure 4.18(a). Out-of-center distortion (top) and octahedral mean quadratic elongation (bottom) of Ta^{5+} and V^{5+} substituted K-HTB (filled symbols represent samples with minor additional phases). The dotted lines are for eye-guide.

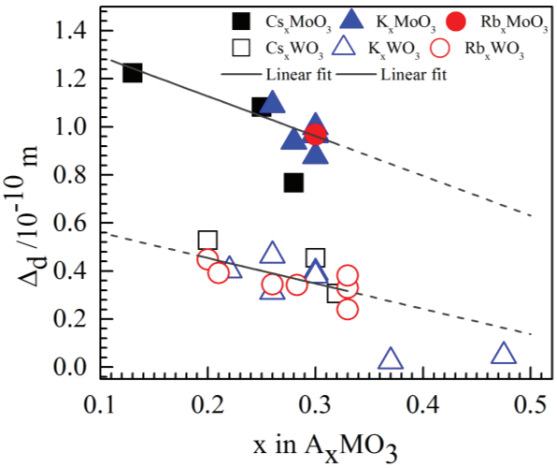

Figure 4.18(b). Out-of-center distortion of some alkali metal molybdenum and tungsten bronzes. Data are given of K_xWO_3 for x = 0.183 [120], 0.2167 [120], 0.22 [this study], 0.26 [this study], 0.26 [107], 0.3 [this study], 0.37 [52] and 0.475 [51], Rb_xWO_3 for x = 0.20 [121], 0.21 [121], 0.26 [121], 0.28 [122] 0.33 [123], Cs_xWO_3 for x = 0.2 [120], 0.3 [124] and 0.32 [120], K_xMoO_3 for x = 0.26 [125], 0.28 [126], 0.3 [127], 0.3 [128] and 0.3 [129], Rb_xMoO_3 for x = 0.3 [130] and Cs_xMoO_3 for x = 0.13 [131], 0.25 [132] and 0.28 [133].

Taking some tungsten (K_xWO_3, Rb_xWO_3 and Cs_xWO_3) and molybdenum (K_xMoO_3, Rb_xMoO_3 and Cs_xMoO_3) bronzes into account, for instance, the Δ_d shows a linear inverse relationship with compositional x as shown in Figure 4.18(b). The higher Δ_d value of the molybdenum series clearly demonstrates that Mo^{6+} cation is a stronger SOJT distorter than W^{6+} in the respective bronzes. $K_{0.37}WO_3$ and $K_{0.48}WO_3$ with high W^{5+} cation contents show almost no SOJT distortion; the respective small Δ_d values are due to pseudo-first-order Jahn-Teller distortion. Substitution of W^{5+} cation with strong SOJT distorter may therefore be difficult as observed in the vanadium substituted bronze solid solution as well as on the V^{5+}/Ta^{5+} mixed substitution system where vanadium only dominates the distortion in the bronzes. Because tantalum did not change the distortion it simply dilutes it in the double substituted series which leads to a total higher substitution rate, shifting the distortion curve (Figure 4.18(a)) to higher y values. Proposing for example a substitution of ⅔ vanadium- and ⅓ tantalum cations for pentavalent tungsten would lead to a total substitution of y to be around 0.2, whereas ⅔ Ta^{5+} and ⅓ V^{5+} should lead to a full substitution possibility. As such slightly a higher potassium containing $K_{0.33}(W^{6+}_{0.67}W^{5+}_{0.33-y}V^{5+}_{y})O_3$ bronze, as the maximum potassium concentration in a HTB structure type, did not allow for substitution of W^{5+} cation more than y = 0.16.

4.4.3. Raman spectra analysis

The Raman spectra recorded for powder samples of $K_{0.3}(W^{6+}_{0.7}W^{5+}_{0.3-y}Ta^{5+}_{y/2}V^{5+}_{y/2})O_3$ solid solution series are given in Figure 4.19. For their direct comparison, the Raman spectrum of $K_{0.3}(W^{6+}_{0.7}W^{5+}_{0.3})O_3$ bronze is also included in the Figure 4.19. It shows that the vibrational properties strongly dependent on the Ta and V composition. Some of the Raman bands in the lower-wavenumbers region disappeared due to overlapping vibrational modes. A significant shifting of the higher-wavenumber modes are observed because of successive incorporation of Ta and V in these materials. The common feature is the presence of bands in the 850 cm^{-1} – 1050 cm^{-1} Raman shift region due to terminal M=O bonds. The Raman peaks which are observed in the range of 80 cm^{-1} to 1100 cm^{-1} Raman shift region given in Figure 4.19 can be divided into two parts; 500 cm^{-1} – 1050 cm^{-1} and below 500 cm^{-1}. In the first range the stretching vibrations of the terminal M=O (M = W, Ta, V) bonds to be observed with higher Raman shift values. These bands are strongly dependent on the co-sharing cations, W^{6+}/W^{5+},

Ta^{5+} and V^{5+} present in these compounds. The Raman shifts due to the other possible stretching vibrations of M–O bonds are also located in the first region. There are four or five bands which were found in the first region. Some of the bands are broad and diffuse due to the effects of all possible M–O (M = $W^{6+}/W^{5+}/Ta^{5+}/V^{5+}$) stretching bonds. In the second region, the bending and lattice modes are situated. The phonon modes with frequencies < 500 cm^{-1} are due to bending vibrations of O–W/Ta/V–O bonds and those which are below 200 cm^{-1} are due to bending vibrations of M–O–W bridging bonds. The characteristics Raman shift related to K–O bonds to be located in the very low wavenumbers region; elsewhere it is reported that it could be found at 60 cm^{-1} and 97 cm^{-1} Raman shift [109] in the $K_{0.3}WO_3$ bronze sample.

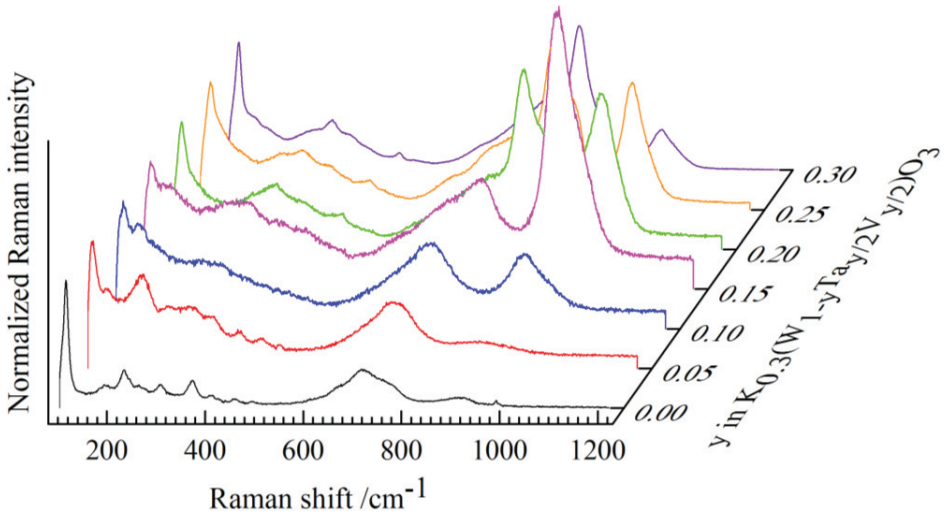

Figure 4.19. Raman spectra of tantalum and vanadium substituted hexagonal potassium tungsten bronzes, $K_{0.3}(W^{6+}_{0.7}W^{5+}_{0.3-y}Ta^{5+}_{y/2}V^{5+}_{y/2})O_3$ solid solution series.

Figure 4.19 also shows that the terminal Raman peaks (originated from M=O bond) have been shifted towards left and the intensities of these peaks gradually increased, however the peaks originated from M–O stretching vibrations gradually shifted towards higher Raman shift values. In the $K_{0.3}(W^{6+}_{0.7}W^{5+}_{0.3-y}Ta^{5+}_{y})O_3$ series the M–O stretching bands are dominating over M=O bands due to successive incorporation of Ta, whereas in the $K_{0.3}(W^{6+}_{0.7}W^{5+}_{0.3-y2}V^{5+}_{y})O_3$ bronzes both types of stretching bands have cooperative influence on the peak positions, intensities and their respective peak shapes. The co-doping effect of Ta^{5+} and V^{5+} instead of W^{5+} cations is clearly observed in the $K_{0.3}(W^{6+}_{0.7}W^{5+}_{0.3-y}Ta^{5+}_{y/2}V^{5+}_{y/2})O_3$ solid solution series from the given Raman spectra (Figure 4.19).

4.4.4. MIR spectra analysis

The mid-infrared spectra of $K_{0.3}(W6^{+}_{0.7}W^{5+}_{0.3-y}Ta^{5+}_{y/2}V^{5+}_{y/2})O_3$ solid solution series are given in Figure 4.20. The spectrum of $K_{0.3}(W^{6+}_{0.7}W^{5+}_{0.3})O_3$ bronze consists of a weak broad phonon absorption band below 1000 cm^{-1}, which could be related to the surface effects of the tungsten oxide compounds. The broad MIR absorption peaks in the region of 500 cm^{-1} – 1100 cm^{-1} are originated from the stretching modes within MO_6 (M = W, Ta, V) octahedra. The peaks appear below 480 cm^{-1} due to the bending modes of M–O–M bridging bonds. The intensity of the absorption band has been increased with successive incorporation of Ta^{5+} and V^{5+}. It indicates that the numbers of free carriers in the system successively decreased due to replacement of $W^{5+}(d^1)$ by both $Ta^{5+}(d^0)$ and $V^{5+}(d^0)$ cations. Dey et al. [111] also reported similar absorption spectra for $Nb^{5+}(d^0)$ substituted $Cs_{0.25}(W_{1-y}Nb_y)O_3$ and $Cs_{0.3}(W_{1-y}Nb_y)O_3$ bronzes. Above 1100 cm^{-1} there is no absorption peak which indicates that the materials are transparent for MIR radiation in the range of 1100 cm^{-1} to 4000 cm^{-1} wavenumbers.

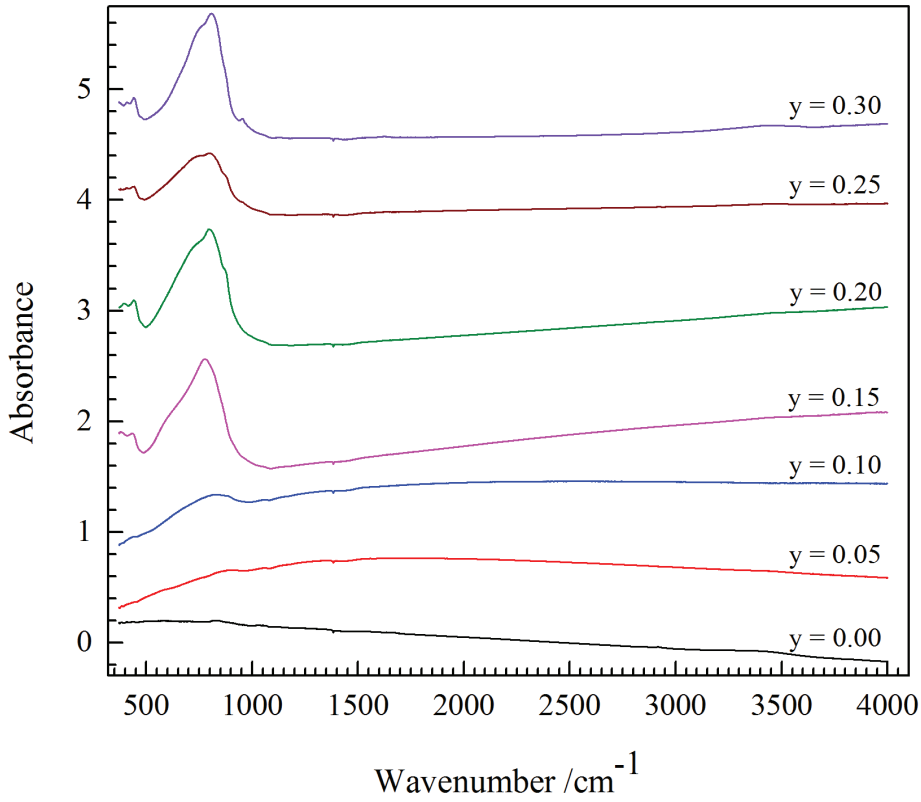

Figure 4.20. MIR spectra of polycrystalline tantalum and vanadium substituted hexagonal potassium tungsten bronzes, $K_{0.3}(W^{6+}_{0.7}W^{5+}_{0.3-y}Ta^{5+}_{y/2}V^{5+}_{y/2})O_3$ solid solution series.

5.1. Structure of $Rb_{0.3}(W^{6+}_{0.7}W^{5+}_{0.3})O_3$ bronze

Powder X-ray diffraction data of $Rb_{0.3}(W^{6+}_{0.7}W^{5+}_{0.3})O_3$ bronze is refined using HTB structure of space group $P6_3/mcm$. Figure 5.1 shows the Rietveld refinement plot of powder X-ray diffraction data of $Rb_{0.3}(W^{6+}_{0.7}W^{5+}_{0.3})O_3$ bronze and the details of the structural parameters are given in Table 5.1. HTB structure of $Rb_{0.27}WO_3$ bronze was reported by Magnéli [54], the XRD data was recorded by film technique and treated the data in the space group $P6_3/mcm$ for x = 0.27. Sato et al. [134] investigated a series of samples with various x-compositions and single crystal of $Rb_{0.33}WO_3$ bronze from neutron powder diffraction data. It is reported that at room-temperature all these bronzes crystallized in the space group $P6_3/mcm$ though the Rb content is different for each sample.

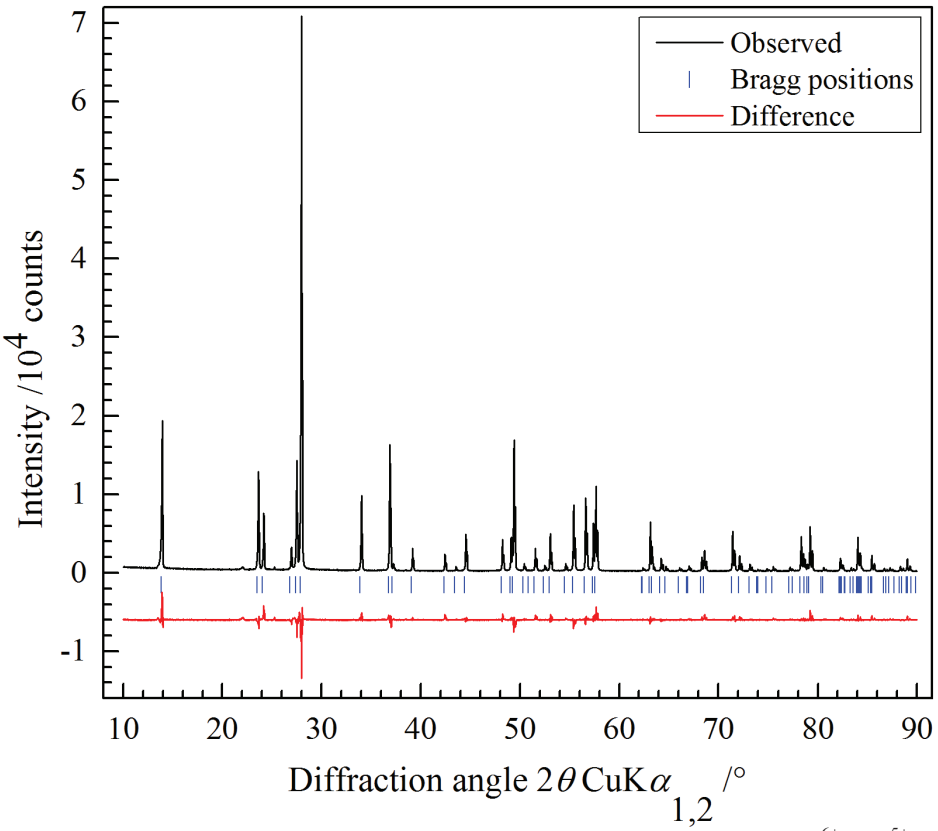

Figure 5.1. Rietveld refinement plot of powder X-ray diffraction data of $Rb_{0.3}(W^{6+}_{0.7}W^{5+}_{0.3})O_3$ bronze ($P6_3/mcm$) measured at ambient conditions.

Guo et al. [121] also prepared a series of Rb_xWO_3 (x = 0.21 – 0.33) bronzes by hybrid microwave technique. The XRD data were also treated using the space group $P6_3/mcm$. The

composition-dependent lattice parameters were found; the *a*-cell parameter decreased and the *c*-cell parameter increased with increasing x-compositions. Brusetti et al. [123, 135] also investigated the x-dependent single phase region of hexagonal Rb_xWO_3 bronzes for x = 0.215 – 0.33 and reported that the metric parameters were changed with respect to Rb content. So far the available crystal structural information found for the hexagonal Rb_xWO_3 bronzes, there is no disputation about the space group at ambient conditions. The observed lattice parameters, positions of atoms, interatomic distances and angles are consistent with earlier several reports [121, 123]. Additionally, Raman spectrum of $Rb_{0.3}(W^{6+}_{0.7}W^{5+}_{0.3})O_3$ bronze is recorded to correlate the crystal structural information with Raman spectroscopy as a complementary method. The factor group analysis predicts 12 ($3A_{1g} + 6E_{2g} + 3E_{1g}$) Raman active modes for the space group $P6_3/mcm$. The Raman spectrum of $Rb_{0.3}WO_3$ powder sample shows 12 bands in the range of 80 cm^{-1} – 1200 cm^{-1} at 300 K as shown in Figure 5.2.

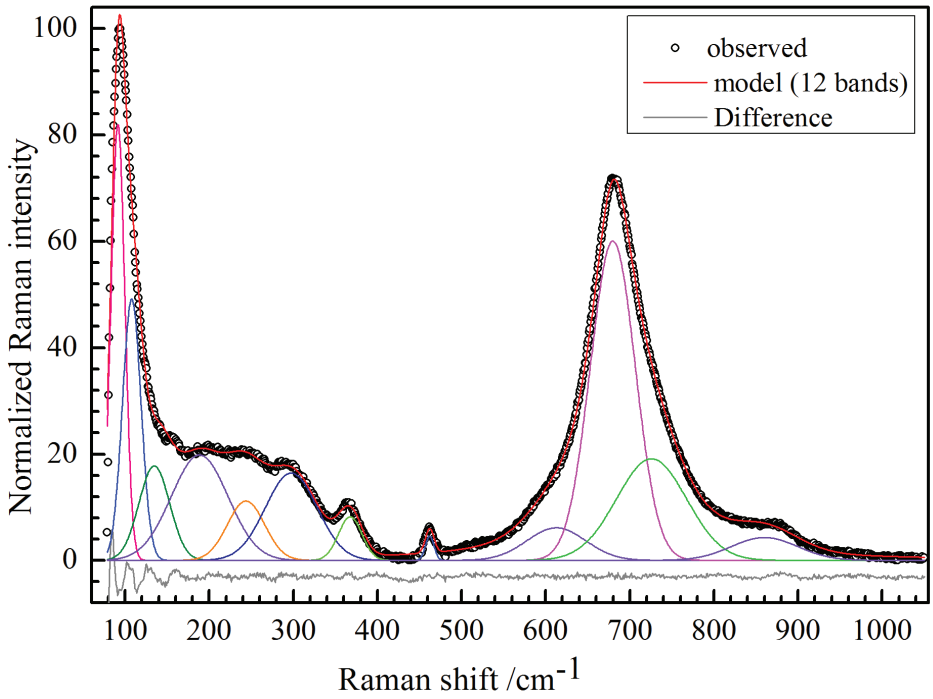

Figure 5.2. Observed and fitted Raman spectrum of $Rb_{0.3}(W^{6+}_{0.7}W^{5+}_{0.3})O_3$ powder sample showing respective band components. The difference curve justifies the quality of the fit.

Scott et al. [136] reported a single broad feature at 655 cm^{-1} for hexagonal $Rb_{0.3}WO_3$ bronze. This author investigated the comparative Raman spectra of cubic $Na_{0.61}WO_3$, tetragonal

$Na_{0.28}WO_3$ and hexagonal $Rb_{0.3}WO_3$ bronzes so there is no clear hint about the total number of bands expected as well as observed. There is no available data for systematic Raman study of Rb_xWO_3 bronzes. The total number of Raman bands observed at room-temperature also suggests that the space group $P6_3/mcm$ is appropriate for $Rb_{0.3}(W^{6+}_{0.7}W^{5+}_{0.3})O_3$ bronze.

Table 5.1. Details of the crystal structure of $Rb_{0.3}(W^{6+}_{0.7}W^{5+}_{0.3})O_3$ bronze obtained from powder X-ray diffraction data Rietveld refinement.

Space group: $P6_3/mcm$, a = 739.07(1) pm, c = 755.79(1) pm, V = 357.52(1) •10^6 pm^3, Z = 6, R_{wp} = 7 %						
Atom	Wyckoff	x	y	z	Occupancy	B_{eq} /10^4 • pm^2
W	6*g*	0.47960(9)	0	¼	1	0.200(42)
O1	12*j*	0.2237(11)	0.4379(13)	¼	1	0.20(14)[a]
O2	6*f*	0	½	0	1	0.20[a]
Rb	2*b*	0	0	0	0.9	4.26(12)

[a] Values were constrained to each other during the refinements.

5.2. $Rb_{0.3}(W^{6+}_{0.7}W^{5+}_{0.3-y}Ta^{5+}_{y})O_3$ solid solution series

Polycrystalline powder samples of $Rb_{0.3}(W^{6+}_{0.7}W^{5+}_{0.3-y}Ta^{5+}_{y})O_3$ solid solution series were characterized using powder X-ray diffraction, SEM/EDX and Raman spectroscopy.

5.2.1. SEM/EDX analysis

The scanning electron microscopy (SEM) images of $Rb_{0.3}(W^{6+}_{0.7}W^{5+}_{0.3-y}Ta^{5+}_{y})O_3$ solid solution series were recorded, the crystallinity of the products is also poor (Figure 5.3); same as $K_{0.3}(W^{6+}_{0.7}W^{5+}_{0.3-y}Ta^{5+}_{y})O_3$ solid solution series. The polycrystalline powder materials are formed as agglomeration products and such effect is more obvious when all the W^{5+} are replaced by Ta^{5+} cations; that is in the fully oxidized analogue $Rb_{0.3}(W^{6+}_{0.7}Ta^{5+}_{0.3})O_3$. The EDX results of each member of this series showed less rubidium content than the nominal compositions. Quantitative determination of Rb content showed an error in this instrument. Tantalum is statistically distributed along with W in the polycrystalline products. The averaged Rb:W, and Ta:W ratios also showed incongruity with respect to nominal compositions. Both W and Ta have nearly same X-ray scattering power which might be one of the reasons for such inconsistent results. The observed EDX results are given in Table 5.2.

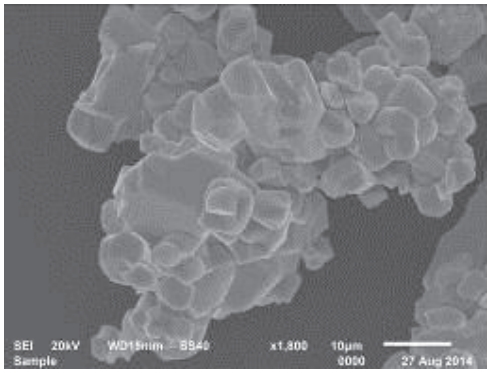

$Rb_{0.3}WO_3$

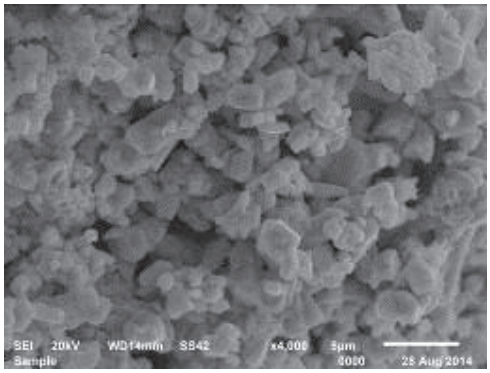

$Rb_{0.3}(W_{0.95}Ta_{0.05})O_3$

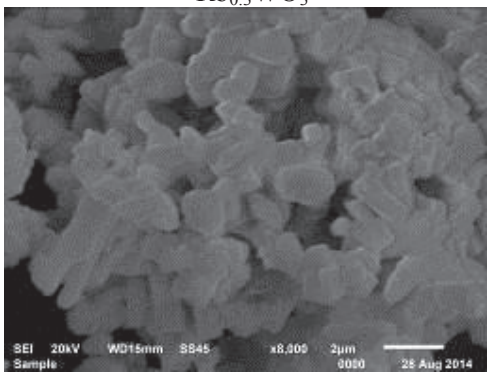

$Rb_{0.3}(W_{0.90}Ta_{0.10})O_3$

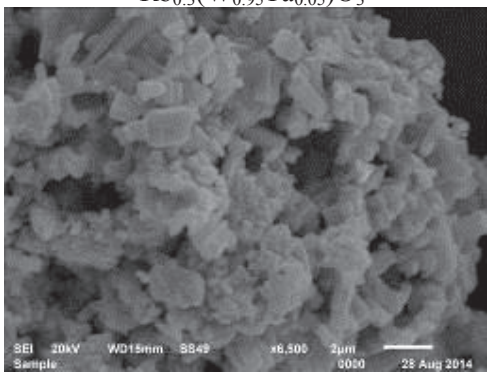

$Rb_{0.3}(W_{0.85}Ta_{0.15})O_3$

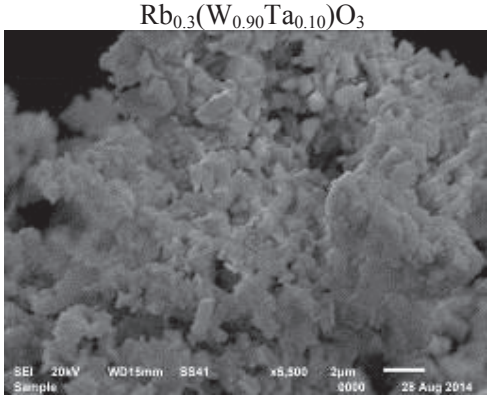

$Rb_{0.3}(W_{0.80}Ta_{0.20})O_3$

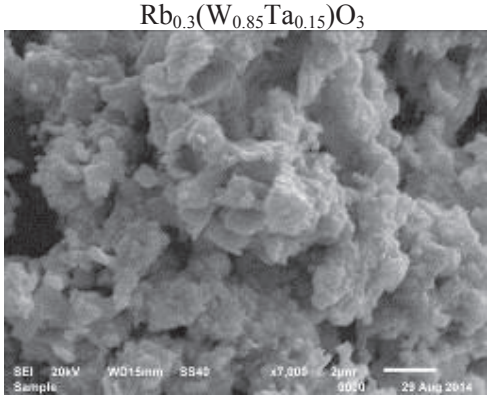

$Rb_{0.3}(W_{0.75}Ta_{0.25})O_3$

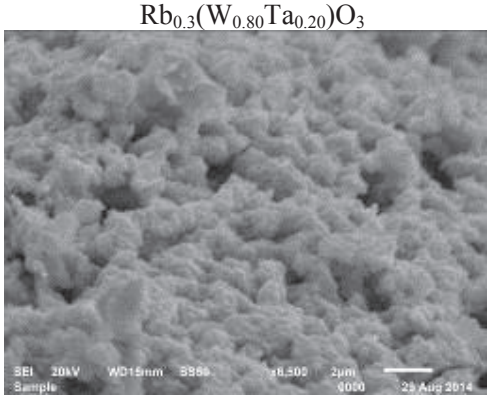

$Rb_{0.3}(W_{0.70}Ta_{0.30})O_3$

Figure 5.3. SEM images of Ta^{5+} substituted Rb-HTB of compositions $Rb_{0.3}(W^{6+}_{0.7}W^{5+}_{0.3-y}Ta^{5+}_{y})O_3$.

Table 5.2. SEM/EDX results of $Rb_{0.3}(W^{6+}_{0.7}W^{5+}_{0.3-y}Ta^{5+}_{y})O_3$ solid solution series.

y	Rb/W		Ta/W	
	Used	Observed	Used	Observed
0.00	0.300	0.209(55)	-	-
0.05	0.316	0.239(75)	0.053	0.114(7)
0.10	0.333	0.295(33)	0.111	0.133(19)
0.15	0.353	0.319(62)	0.176	0.170(23)
0.20	0.375	0.336(43)	0.250	0.249(18)
0.25	0.400	0.352(93)	0.333	0.304(24)
0.30	0.428	0.419(67)	0.428	0.409(48)

5.2.2. Powder X-ray diffraction data investigation

Powder X-ray diffraction data Rietveld refinement confirmed that each sample of $Rb_{0.3}(W^{6+}_{0.7}W^{5+}_{0.3-y}Ta^{5+}_{y})O_3$ solid solution series follows the space group $P6_3/mcm$ as like as the parent $Rb_{0.3}(W^{6+}_{0.7}W^{5+}_{0.3})O_3$ bronze. Figure 5.4 shows the powder XRD patterns of $Rb_{0.3}(W^{6+}_{0.7}W^{5+}_{0.3-y}Ta^{5+}_{y})O_3$ solid solution series, and the Rietveld refinements results are given in Table 5.3.

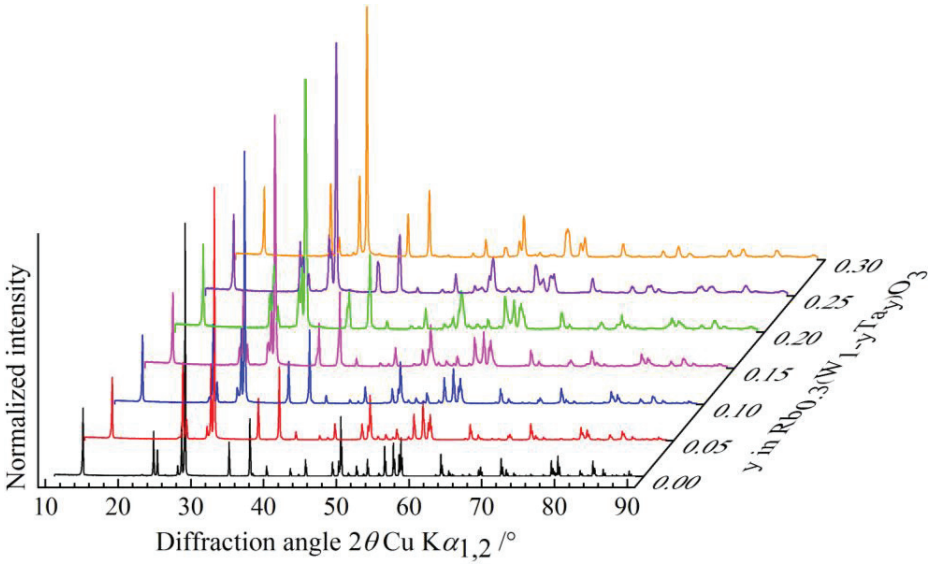

Figure 5.4. Powder X-ray diffraction patterns of $Rb_{0.3}(W^{6+}_{0.7}W^{5+}_{0.3-y}Ta^{5+}_{y})O_3$ solid solution series measured at ambient conditions.

Successive efforts demonstrated that W^{5+} can only be partially replaced by Ta^{5+} in the Rb-HTB structure for $y < 0.1$, producing a pure single phase. Samples prepared with nominal compositions of $y \geq 0.1$ showed a mixture of two phases, namely, HTB-I (W^{5+} is partially replaced) and HTB-II (W^{5+} is more or less fully replaced, oxidized phase containing elements with their highest oxidation state), both of which conform the space group $P6_3/mcm$. The phase fractions of the HTB-II increased with increasing nominal Ta^{5+} composition till reaching a fully oxidized bronzoid phase, that is, $Rb_{0.3}(W^{6+}_{0.7}Ta^{5+}_{0.3})O_3$. Similar results are also found for $K_{0.3}(W^{6+}_{0.7}W^{5+}_{0.3-y}Ta^{5+}_{y})O_3$ solid solution series though those were crystallized in the space group $P6_322$. Details of the structural features of both HTB-I and HTB-II phases are given in Table 5.4. Selected interatomic bond distances and angles are given in Table 5.5. The deep-blue color of the parent $Rb_{0.3}(W^{6+}_{0.7}W^{5+}_{0.3})O_3$ bronze has been changed to a cream-colored $Rb_{0.3}(W^{6+}_{0.7}Ta^{5+}_{0.3})O_3$ upon successive dilution of W^{5+} by Ta^{5+} cations in the $Rb_{0.3}(W^{6+}_{0.7}W^{5+}_{0.3-y}Ta^{5+}_{y})O_3$ solid solution series. For the reduced phase (HTB-I), the discoloration is due the replacement of W^{5+} by Ta^{5+} cations. However, for the mixed phase, the amount of bronzoid phase ultimately determined the color of the products.

Table 5.3. Powder X-ray diffraction data Rietveld refinements results of $Rb_{0.3}(W^{6+}_{0.7}W^{5+}_{0.3-y}Ta^{5+}_{y})O_3$.

y	HTB-I			HTB-II		
	wt-%	*a* /pm	*c* /pm	wt-%	*a* /pm	*c* /pm
0.00	100	739.07(1)	755.79(1)	-	-	-
0.05	100	739.05(1)	755.40(1)	-	-	-
0.10	84.1(8)	738.98(1)	755.15(1)	15.9(8)	736.17(7)	769.17(9)
0.15	70.6(8)	738.85(2)	755.10(2)	29.4(8)	735.38(4)	770.95(5)
0.20	61.2(9)	738.32(3)	755.75(3)	38.8(9)	735.11(4)	770.86(5)
0.25	49.3(1)	737.14(4)	759.43(4)	50.7(1)	734.67(3)	771.34(4)
0.30	-	-	-	100	734.67(2)	771.31(2)

Galasso et al. [137] reported the cream-white color product of $Rb_{0.3}(W^{6+}_{0.7}Ta^{5+}_{0.3})O_3$, a bronzoid analogue oxide. Dey et al. [111] found mixed phase compounds when W^{5+} was substituted by Nb^{5+} during the preparation of $Cs_{0.3}(W_{1-y}Nb_y)O_3$ and $Rb_{0.3}(W_{1-y}Nb_y)O_3$ powder samples using solid state synthesis method. With increasing Ta^{5+} concentration in the HTB-I

phase the *a*- and *c*-cell parameters change anisotropically, that is, the *a*-cell parameter decreases while the *c*-parameter increases as shown in Figure 5.5(a) followed by non-linear increase of the anisotropy factor ($A = |a - c|$) for HTB-I and HTB-II phases (Figure 5.5(b)). The non-linear trend of their cell volumes are shown in Figure 5.5(c).

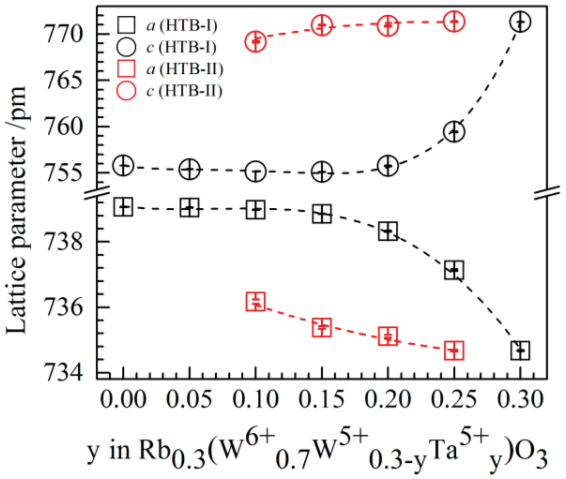

Figure 5.5(a). Lattice parameter change with respect to tantalum composition (y) in the $Rb_{0.3}(W^{6+}_{0.7}W^{5+}_{0.3-y}Ta^{5+}_{y})O_3$ series.

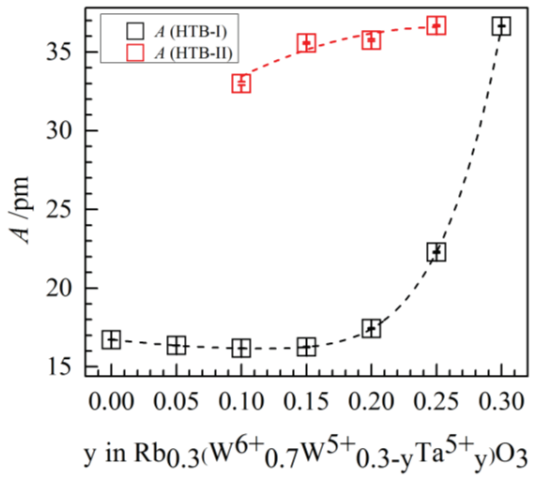

Figure 5.5(b). Change of anisotropy parameter *A* of the HTB-I and HTB-II phases.

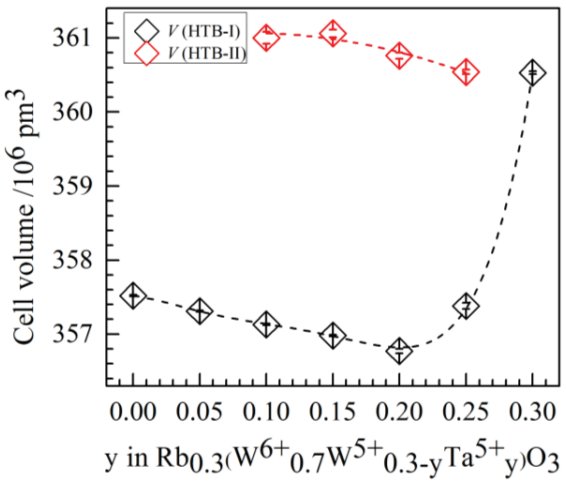

Figure 5.5(c). Cell volume change with respect to tantalum composition (y) of HTB-I and HTB-II in the $Rb_{0.3}(W^{6+}_{0.7}W^{5+}_{0.3-y}Ta^{5+}_{y})O_3$ series.

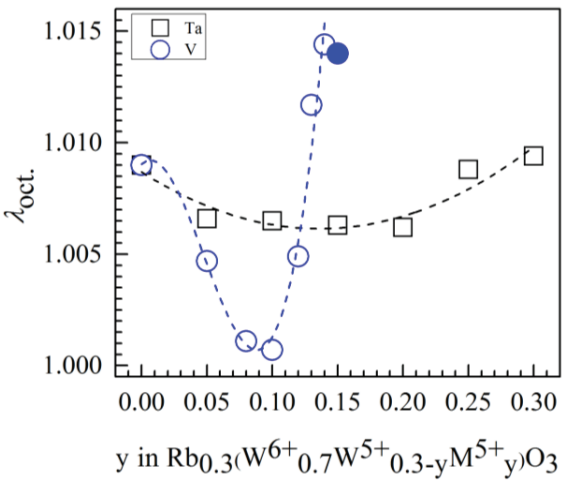

Figure 5.5(d). Octahedral mean quadratic elongation of Ta^{5+} or V^{5+} substituted Rb-HTB (filled symbol represent sample with minor additional phase).

The dotted lines are for eye-guide.

For an analogy, the similar behavior was also observed for some relevant oxides such as $RbTaW_2O_9$ [112 & ref. therein]. Replacing W^{5+} (r = 62 pm [98]) by a slightly larger Ta^{5+} (r = 64 pm [98]) the W–O1a interatomic distance lying in the *ab*-plane varies to the mean value of 182(1) pm up to y = 0.2 and further decreased for y > 0.2. Conversely, W–O1b bond distance gradually increased, that is two shorter W–O1a distances contracted and two longer W–O1b distances further increased with respect to the degree of substitution with Ta^{5+} (Table 5.5). The W–O2 bond distance, subtending a narrow angle of 4.6(2)° with the **c**-axis vector fluctuates close to the mean value 190(1) pm. The non-linear trend of the W–O bond distances is different, leading to a gradual increase of the averaged W–O bond distance as a straight consequence of larger Ta^{5+} cations incorporation into the $Rb_{0.3}(W^{6+}_{0.7}W^{5+}_{0.3})O_3$ bronze. The inter-octahedral W–O1–W angle also changed for few degrees. The gradual expansion of the averaged W–O bond lengths and decrease of the W–O–W angles result in a change of the magnitude and direction of the out-of-center distortion (Δ_d) of the MO_6 octahedra [114] as well as octahedral mean quadratic elongation (λ_{oct}) [113].

Table 5.4. Details of the structural parameters of $Rb_{0.3}(W^{6+}_{0.7}W^{5+}_{0.3-y}Ta^{5+}_{y})O_3$, HTB-I and HTB-II (*italics*) obtained from powder X-ray diffraction data Rietveld refinements.

y	*a* /pm	*c* /pm	$V/10^6 \cdot pm^3$	W(*x*)	O1(*x*)	O1(*y*)
0.00	739.07(1)	755.79(1)	357.52(1)	0.47960(9)	0.2237(11)	0.4379(13)
0.05	739.05(1)	755.40(1)	357.31(1)	0.47970(9)	0.21066(94)	0.42416(98)
0.10	738.98(1)	755.15(1)	357.13(1)	0.47922(12)	0.2159(12)	0.4275(13)
0.15	738.85(1)	755.10(2)	356.98(1)	0.47925(16)	0.2171(16)	0.4274(18)
0.20	738.32(2)	755.75(3)	356.77(3)	0.47923(25)	0.2127(22)	0.4221(27)
0.25	737.14(3)	759.43(4)	357.38(4)	0.47957(37)	0.2161(34)	0.4350(37)
0.30	734.67(2)	771.31(2)	360.53(2)	0.49140(27)	0.1927(17)	0.4309(11)
0.10	*736.17(7)*	*769.17(9)*	*361.00(8)*	*0.5118(17)*	*0.2453(84)*	*0.4088(73)*
0.15	*735.38(4)*	*770.95(5)*	*361.06(5)*	*0.5090(12)*	*0.2358(74)*	*0.4227(43)*
0.20	*735.11(4)*	*770.86(5)*	*360.76(4)*	*0.5054(18)*	*0.2457(76)*	*0.4330(40)*
0.25	*734.67(3)*	*771.34(4)*	*360.54(3)*	*0.5031(19)*	*0.2434(50)*	*0.4268(34)*

The scale Δ_d given by Halasyamani [114] categorized as weak (Δ_d = 0.05 – 0.40), moderate (Δ_d = 0.40 – 0.80) and strong (Δ_d > 0.8) distortions. The author also stated that some cations follow an average order of $Mo^{6+} > V^{5+} > W^{6+} > Nb^{5+} > Ta^{5+} > Ti^{4+}$, all these cations are susceptible for SOJT distortion. The neighboring lone electron pair cations can influence the absolute values of Δ_d for these d^0 cations. In the parent phase $Rb_{0.3}(W^{6+}_{0.7}W^{5+}_{0.3})O_3$, the WO_6 octahedra has Δ_d = 0.27, weakly distorted octahedron. Since 70 % of W position is occupied by $W^{6+}(d^0)$ which is susceptible for SOJT distortion and 30 % with $W^{5+}(d^1)$ which is susceptible for pseudo-FOJT distortion. Thus substitution of W^{5+} with SOJT susceptible $Ta^{5+}(d^0)$ cation is assumed to incorporate additional distortion to MO_6 octahedra (Table 5.5).

Table 5.5. Selected bond distances, angles, octahedral mean quadratic elongation and out-of-center octahedral distortion of $Rb_{0.3}(W^{6+}_{0.7}W^{5+}_{0.3-y}Ta^{5+}_{y})O_3$, HTB-I and HTB-II (*italics*) obtained from powder X-ray diffraction data Rietveld refinements.

y	W–O1a /pm	W–O1b /pm	W–O2 /pm	W–O1–W /°	λ_{oct}	Δ_d /10^{-10} m
0.00	182.70(62)	196.04(63)	189.55(1)	155.97(56)	1.0090	0.27
0.05	179.76(68)	202.87(70)	189.44(1)	150.94(46)	1.0066	0.46
0.10	181.70(88)	199.95(91)	189.41(1)	152.13(59)	1.0065	0.37
0.15	183(1)	199(1)	189.40(1)	152.07(79)	1.0063	0.33
0.20	182(2)	201(2)	189.56(2)	150(1)	1.0062	0.39
0.25	178(2)	200(3)	190.45(2)	155(2)	1.0088	0.45
0.30	168(1)	209(1)	192.93(1)	153.12(79)	1.0094	0.82
0.10	*158(6)*	*228(6)*	*192.49(6)*	*145(4)*	*1.0257*	*1.40*
0.15	*168(4)*	*212(4)*	*192.85(3)*	*150(2)*	*1.0093*	*0.88*
0.20	*165(4)*	*212(4)*	*192.76(3)*	*154(4)*	*1.0123*	*0.94*
0.25	*166(3)*	*212(3)*	*192.85(2)*	*151(2)*	*1.0104*	*0.92*

Since Ta^{5+} is also a weak distorter, the Δ_d fluctuates within a narrow range up to y = 0.25. The Δ_d value is very high for the end member because there is no additional octahedral distortion from W^{5+} cation in the bronzoid analogue $Rb_{0.3}(W^{6+}_{0.7}Ta^{5+}_{0.3})O_3$ oxide. The bond valence parameter [116] of W^{5+}–O (189 pm) is about 3 pm less than that of Ta^{5+}–O (192 pm) distance which also allowed the system for the substitution of W^{5+} by Ta^{5+}cation. Theoretical bond

valence sum (BVS) [117] of W in the parent $Rb_{0.3}(W^{6+}_{0.7}W^{5+}_{0.3})O_3$ bronze is 5.7 v.u. Substitution of W^{5+} with Ta^{5+} optimize the effect of FOJT distortion by adding SOJT distortion as well as reduce the BVS difference, successively.

5.2.3. Raman spectra analysis

The Raman spectra of Ta^{5+} containing $Rb_{0.3}(W^{6+}_{0.7}W^{5+}_{0.3-y}Ta^{5+}_{y})O_3$ solid solution series are given in Figure 5.6, recorded at room-temperature. For the direct comparison, the Raman spectrum of hexagonal $Rb_{0.3}(W^{6+}_{0.7}W^{5+}_{0.3})O_3$ bronze is also included in the Figure 5.6. It is observed that in spite of their different chemical compositions, considerable influences on the crystal structure, each sample of this series has comparable Raman spectrum. Particularly, the vibrational spectra do not change extensively due to the incorporation of Ta^{5+}. Some of the lower-wavenumbers modes were disappeared due to overlapping vibration with successive change of y-composition. A shift of the higher-wavenumber modes is observed with successive dilution of W^{5+} cations. The general feature for each sample is the presence of 850 cm^{-1} – 1000 cm^{-1} bands due to terminal M=O bonds.

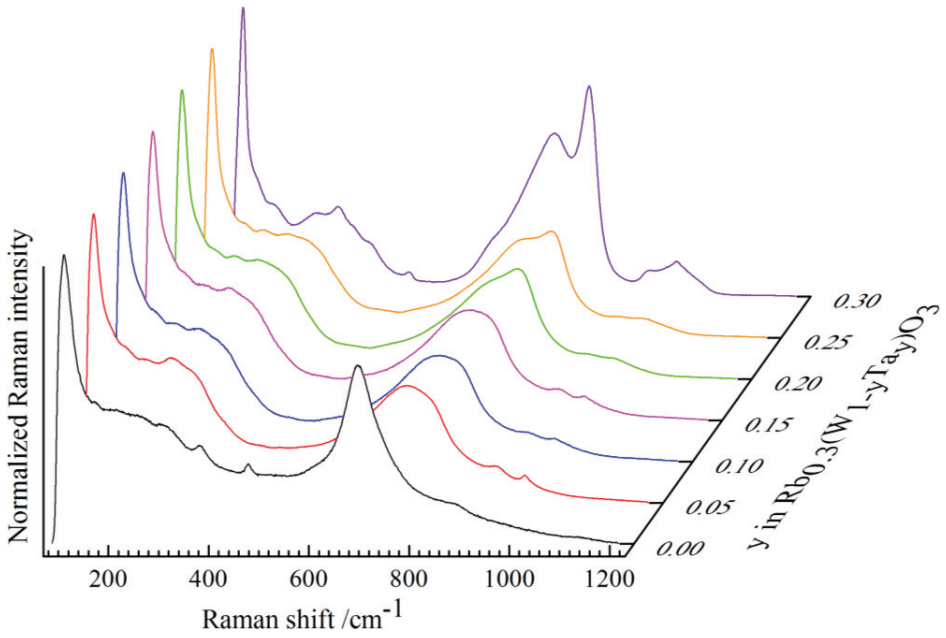

Figure 5.6. Raman spectra of polycrystalline $Rb_{0.3}(W^{6+}_{0.7}W^{5+}_{0.3-y}Ta^{5+}_{y})O_3$ solid solution series recorded on a smooth surface of pressed pellet powder sample at room-temperature.

The total Raman peaks in the range of 80 cm^{-1} to 1000 cm^{-1} as shown in Figure 5.6, can be divided into three subgroups; 850 cm^{-1} – 1050 cm^{-1}, 850 cm^{-1} – 500 cm^{-1} and below 500 cm^{-1}. In the first range only the stretching vibrations of the terminal M=O (M = W, Ta) bonds are observed. The number of bands is two or three in the first range. They are strongly dependent on the W^{6+}/W^{5+} and Ta^{5+} concentration. These bands are weak and broad, an indication that the Ta and W are statistically distributed as M=O dangle bonds at the crystal surface. The broadening of the terminal peaks is the co-sharing effect of both W=O (972 cm^{-1}) and Ta=O (906 cm^{-1}) groups. In the second range, the stretching modes of W–O bonds are responsible for the observed Raman peaks. There are three broad and diffuse Raman peaks in this region. It may well possible that such broadness of the peaks happened due to the all possible M–O (M = $W^{6+}/W^{5+}/Ta^{5+}$) stretching modes. There are four Raman peaks (627 cm^{-1}, 700 cm^{-1}, 845 cm^{-1} and 906 cm^{-1}) in Ta_2O_5 due to Ta–O stretching modes of vibrations. Whereas, $Rb_{0.3}(W^{6+}_{0.7}W^{5+}_{0.3})O_3$ bronze shows three bands at 612 cm^{-1}, 679 $cm^{-1}$and 725 cm^{-1} for W–O stretching vibrations. The combined Raman peaks from all possible W/Ta–O stretching bands may be observed for $Rb_{0.3}(W^{6+}_{0.7}W^{5+}_{0.3-y}Ta^{5+}_{y})O_3$ series. The Raman peaks at about 679 cm^{-1} and 725 cm^{-1} found in the $Rb_{0.3}(W^{6+}_{0.7}W^{5+}_{0.3})O_3$ bronze are becoming more intense and gradually moving towards the higher Raman shift region because of successive incorporation of Ta^{5+} in the $Rb_{0.3}(W^{6+}_{0.7}W^{5+}_{0.3-y}Ta^{5+}_{y})O_3$ series. In the third region, the bending and lattice modes are located. The phonon modes with frequencies < 500 cm^{-1} are due to the bending modes vibrations of O–W–O and those which are below 200 cm^{-1} because of W–O–W bending modes of vibrations. The characteristics Raman bands which are associated with the vibrations of Rb–O bonds may be located in the very low Raman shift region since Rb–O distances in these bronze samples are too long compared to normal Rb–O bond distance.

5.3. $Rb_{0.3}(W^{6+}_{0.7}W^{5+}_{0.3-y}V^{5+}_{y})O_3$ solid solution series

Polycrystalline powder samples of $Rb_{0.3}(W^{6+}_{0.7}W^{5+}_{0.3-y}V^{5+}_{y})O_3$ solid solution series were also characterized by powder X-ray diffraction, SEM/EDX and Raman spectroscopy.

5.3.1. SEM/EDX analysis

SEM micrographs of $Rb_{0.3}(W^{6+}_{0.7}W^{5+}_{0.3-y}V^{5+}_{y})O_3$ solid solution series were recorded; the crystallinity of this series is better than that of the $Rb_{0.3}(W^{6+}_{0.7}W^{5+}_{0.3-y}Ta^{5+}_{y})O_3$ solid solution

series. Nonetheless, the crystals are not suitable enough for collecting single crystal X-ray diffraction data (Figure 5.7). The EDX results show the rubidium content in each sample is very low with respect to the used nominal compositions. The instrument used for this study always shows such differences for Rb compound. The vanadium is statistically distributed in the polycrystalline products. The averaged Rb:W and V:W ratios are inconsistent with nominal composition. The observed EDX results are given in Table 5.6.

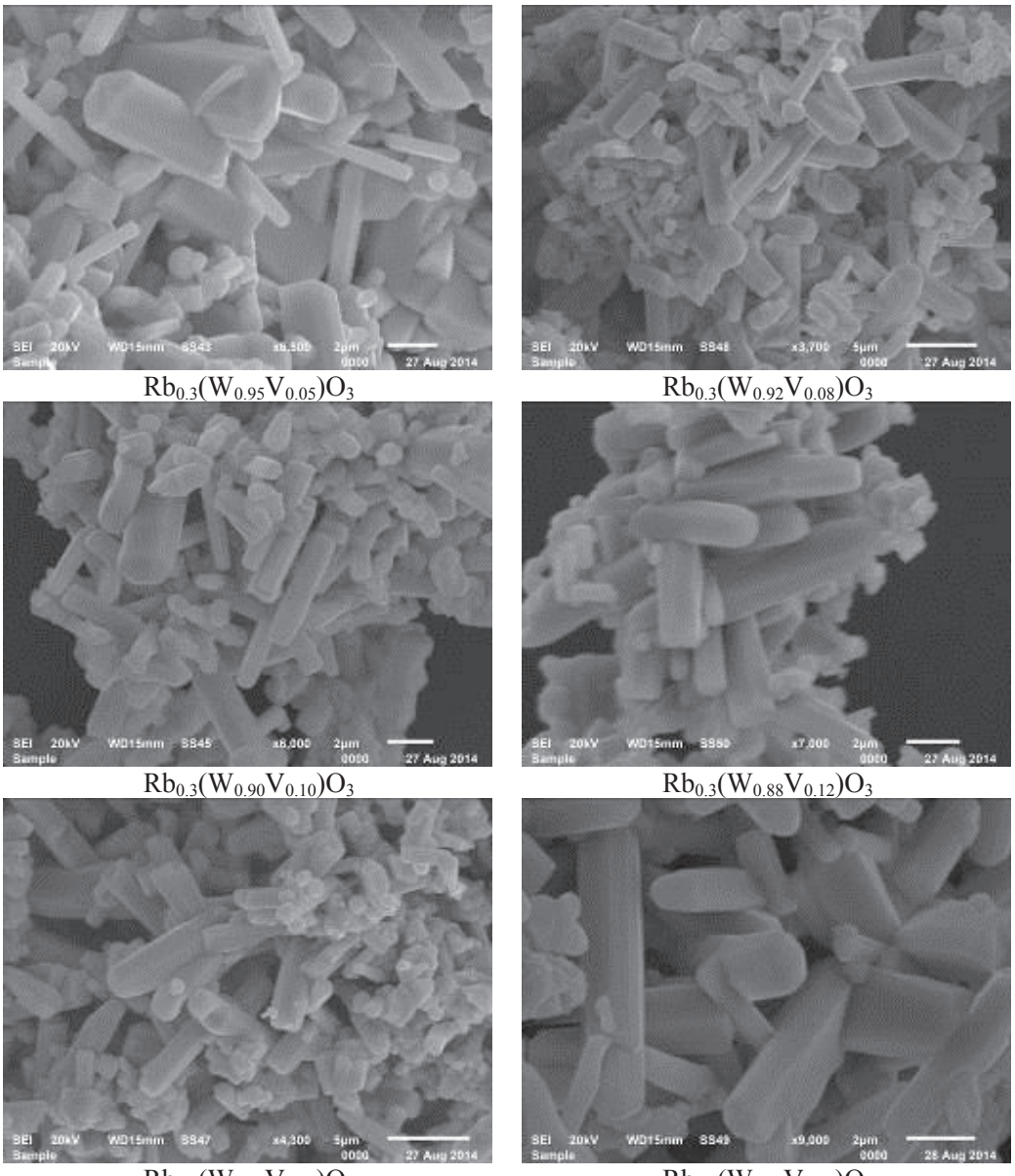

Figure 5.7. SEM micrographs of $Rb_{0.3}(W^{6+}_{0.7}W^{5+}_{0.3-y}V^{5+}_{y})O_3$ solid solution series.

Table 5.6. SEM/EDX results of $Rb_{0.3}(W^{6+}_{0.7}W^{5+}_{0.3-y}V^{5+}_{y})O_3$ solid solution series.

y	Rb/W		V/W	
	Used	Observed	Used	Observed
0.05	0.316	0.172(35)	0.053	0.036(2)
0.08	0.326	0.192(79)	0.087	0.057(9)
0.10	0.333	0.203(23)	0.111	0.079(5)
0.12	0.341	0.220(30)	0.136	0.100(7)
0.13	0.345	0.220(45)	0.149	0.107(12)
0.14	0.357	0.238(4)	0.167	0.119(6)

5.3.2. Powder X-ray diffraction data investigation

Additional attempts were made for successive replacement of W^{5+} by V^{5+} cations in the $Rb_{0.3}(W^{6+}_{0.7}W^{5+}_{0.3-y}V^{5+}_{y})O_3$ solid solution series up to the limit of miscibility range. The parent $Rb_{0.3}(W^{6+}_{0.7}W^{5+}_{0.3})O_3$ bronze is deep-blue whereas successive incorporation of V^{5+} the color changed to brown due to subsequent dominance of V^{5+}(yellow) over W^{5+} (blue) responsible for the color in the visible range. The color changed in the order: deep-blue (y = 0) → light blue (y = 0.05 – 0.08) → brownish-blue (y = 0.1) → brown (y = 0.14), similar to $K_{0.3}(W^{6+}_{0.7}W^{5+}_{0.3-y}V^{5+}_{y})O_3$ bronzes. Rietveld refinement of powder X-ray diffraction data confirmed that $Rb_{0.3}(W^{6+}_{0.7}W^{5+}_{0.3-y}V^{5+}_{y})O_3$ produce pure HTB-type phase in the space group $P6_3/mcm$ up to y = 0.14, slightly less than that of the $K_{0.3}(W^{6+}_{0.7}W^{5+}_{0.3-y}V^{5+}_{y})O_3$ series. Figure 5.8 shows the XRD patterns of $Rb_{0.3}(W^{6+}_{0.7}W^{5+}_{0.3-y}V^{5+}_{y})O_3$ solid solution series. For $y \geq 0.15$ a mixture of two phase products was observed; V^{5+} substituted Rb-HTB along with non-bronze impurity phase of vanadium oxide. Detailed structural parameters of vanadium substituted $Rb_{0.3}(W^{6+}_{0.7}W^{5+}_{0.3-y}V^{5+}_{y})O_3$ solid solution series are given in Table 5.7. Selected interatomic bond distances and angles, octahedral mean quadratic elongation and out-of-center octahedral distortion are given in Table 5.8. An anisotropic behavior of the lattice parameters is observed with an increase of vanadium concentration as shown in Figure 5.9(a). That is, the *a*-cell parameter decreased followed by increase of the *c*-cell parameter with increasing of vanadium concentration (y) in the system, leading to an overall contraction of the cell volume.

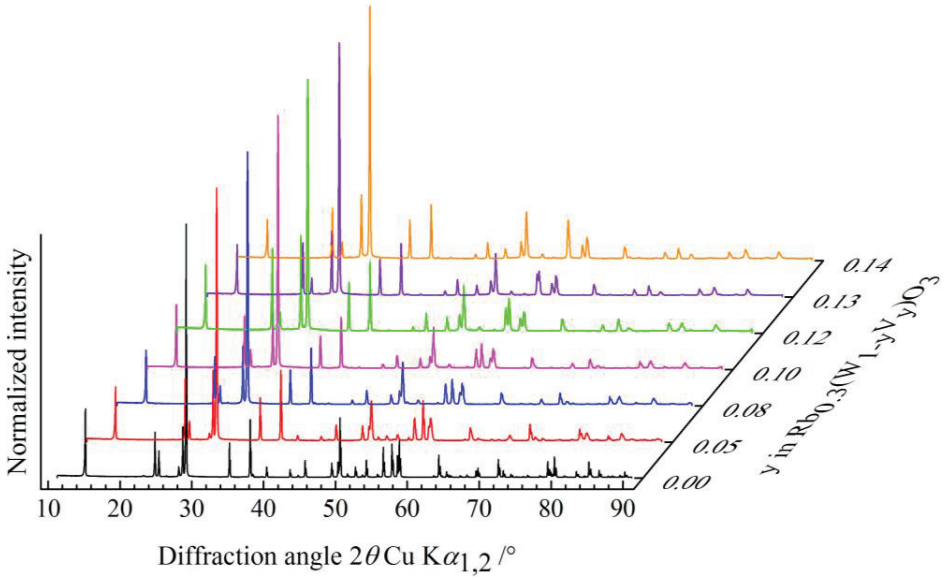

Figure 5.8. Powder X-ray diffraction patterns of $Rb_{0.3}(W^{6+}_{0.7}W^{5+}_{0.3-y}V^{5+}_{y})O_3$ solid solution series.

Table 5.7. Details of the crystal structure of $Rb_{0.3}(W^{6+}_{0.7}W^{5+}_{0.3-y}V^{5+}_{y})O_3$ solid solution series obtained from powder X-ray diffraction data Rietveld refinements.

y	*a* /pm	*c* /pm	$V/10^6 \cdot pm^3$	W(*x*)	O1(*x*)	O1(*y*)
0.05	736.59(1)	754.00(1)	354.29(1)	0.48385(11)	0.2084(12)	0.4151(15)
0.08	734.44(1)	757.30(1)	353.76(1)	0.49361(22)	0.2068(18)	0.4191(16)
0.10	733.13(1)	759.32(1)	353.45(1)	0.49533(33)	0.2067(25)	0.4222(17)
0.12	730.69(1)	764.02(1)	353.26(1)	0.49632(54)	0.2011(30)	0.4332(15)
0.13	729.40(1)	767.22(1)	353.49(1)	0.49669(44)	0.1910(19)	0.4367(13)
0.14	728.01(1)	770.44(1)	353.63(1)	0.49497(38)	0.1901(20)	0.4384(13)
0.15	726.38(1)	774.72(2)	353.99(1)	0.49606(65)	0.1973(33)	0.4430(17)

The anisotropy factor $A = |c - a|$, shown in Figure 5.9(b), increases with a steep slope at y = 0.14. The smaller ionic radius of V^{5+} (r = 54 pm) [98] compare to that of W^{5+} (r = 62 pm [98]) might limit the miscibility of V^{5+} up to y = 0.14. Substitution of W^{5+} by much smaller V^{5+} cation led to the significant change of the cell volume as shown in Figure 5.9(c). The W–O1 distances lying in the *ab*-plane showed opposite behavior; that is two shorter W–O1a distances reduced and two longer W–O1b distances further increased (Table 5.8). The difference between two types of W–O1 bond distances increased with respect to vanadium

composition. The W–O2 bond distance along the **c**-axis vector gradually increases up to y = 0.14. The inter-octahedral angle W–O1–W also changed with successive incorporation of V^{5+} in the $Rb_{0.3}(W^{6+}_{0.7}W^{5+}_{0.3-y})O_3$ system (Table 5.8). The bond distances and angles changed in a cooperative manner leading to increase the *c*-cell parameter and decrease the *a*-cell parameter.

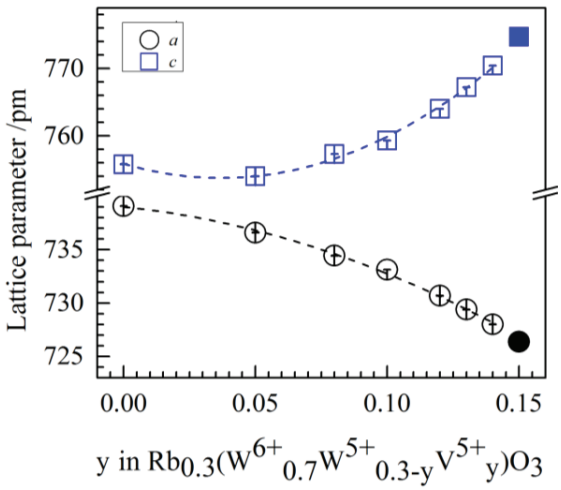

Figure 5.9(a). Lattice parameters change with respect to vanadium composition (y) of the $Rb_{0.3}(W^{6+}_{0.7}W^{5+}_{0.3-y}V^{5+}_{y})O_3$ bronzes.

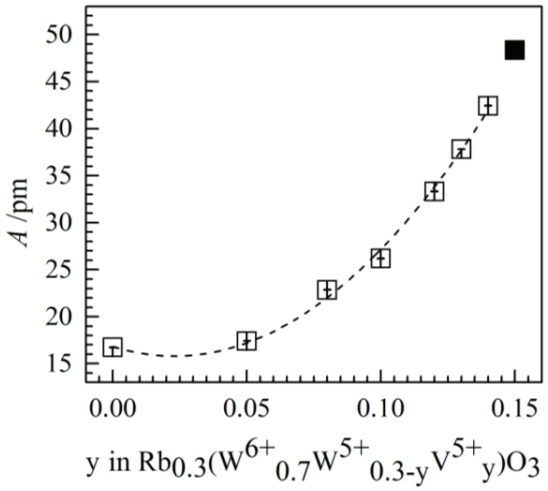

Figure 5.9(b). Change of anisotropy parameter *A* with respect to vanadium composition (y) of $Rb_{0.3}(W^{6+}_{0.7}W^{5+}_{0.3-y}V^{5+}_{y})O_3$ bronzes.

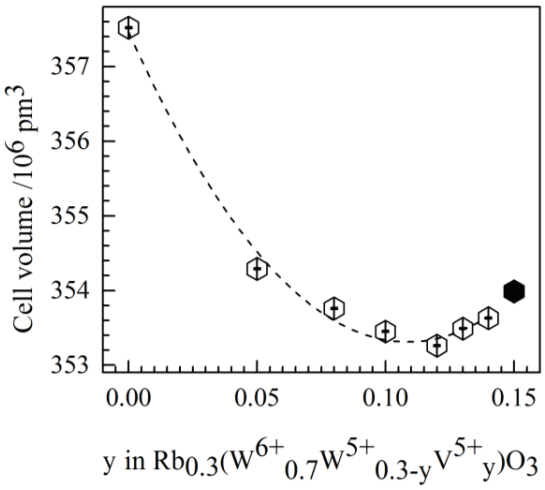

Figure 5.9(c). Cell volume change with respect to vanadium composition (y) of the $Rb_{0.3}(W^{6+}_{0.7}W^{5+}_{0.3-y}V^{5+}_{y})O_3$ bronzes.

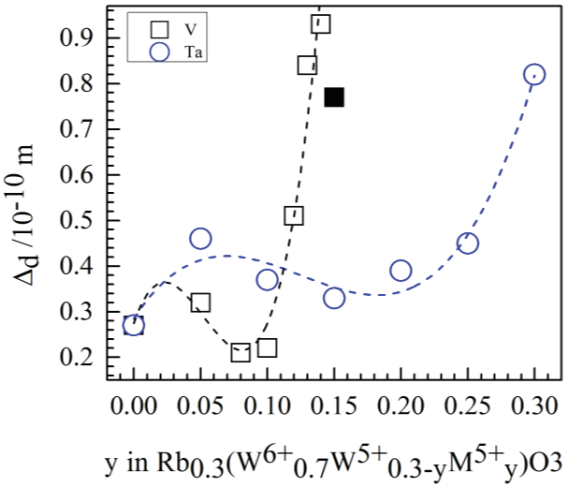

Figure 5.9(d). Out-of-center octahedral distortion of Ta^{5+} or V^{5+} substituted Rb-HTB bronzes.

Filled symbol represents sample with minor additional phase. The dotted lines are for eye-guide.

The octahedral mean quadratic elongation decreased up to y = 0.10, then significantly increased due to additional V^{5+} cation incorporation. The out-of-center octahedral distortion index also fluctuates between 0.3 – 0.2 for y = 0 – 0.10, then increased a lot for y = 0.14. Since V^{5+} is a strong distorter, even stronger than W^{6+}, it is therefore clear that the MO_6 octahedra in the $Rb_{0.3}(W^{6+}_{0.7}W^{5+}_{0.3-y}V^{5+}_{y})O_3$ system develops the magnitude of Δ_d with increasing y; the weakly distorted parent system transformed into a HTB phase containing strongly distorted MO_6 octahedra for y = 0.14 (Table 5.8). A further V^{5+} substitution led to forming HTB structure, however, together with V_2O_5 where V^{5+} is five-fold coordinated [119] – a consequence of very high Δ_d of 1.48 considering a long V–O distance of 279 pm for VO_6 octahedron.

Table 5.8. Selected bond distances, angles, octahedral mean quadratic elongation and out-of-center octahedral distortion of $Rb_{0.3}(W^{6+}_{0.7}W^{5+}_{0.3-y}V^{5+}_{y})O_3$ bronzes obtained from powder X-ray diffraction data Rietveld refinements.

y	W–O1a /pm	W–O1b /pm	W–O2 /pm	W–O1–W /°	λ_{oct}	Δ_d /10^{-10} m
0.00	182.70(62)	196.04(63)	189.55(1)	155.97(56)	1.0090	0.27
0.05	184.13(96)	200.14(97)	188.88(1)	147.43(60)	1.0047	0.32
0.08	185(1)	196.21(74)	189.38(1)	148.74(84)	1.0011	0.21
0.10	182(2)	195(2)	189.86(1)	150(1)	1.0007	0.22
0.12	175(2)	203(2)	191.02(1)	1547(1)	1.0049	0.51
0.13	166(1)	208(1)	191.82(1)	155.09(89)	1.0117	0.84
0.14	163(1)	209(1)	192.64(1)	155.78(94)	1.0144	0.93
0.15	163(1)	204(2)	193.70(1)	158(2)	1.0140	0.77

5.3.3. Raman spectra analysis

The Raman spectra of $Rb_{0.3}(W^{6+}_{0.7}W^{5+}_{0.3-y}V^{5+}_{y})O_3$ solid solution series recorded at room temperature are given in Figure 5.10. The Raman spectrum of the $Rb_{0.3}(W^{6+}_{0.7}W^{5+}_{0.3})O_3$ bronze also includes in this figure for their direct comparison. Each member of this series has different chemical compositions, considerable influence was found for their crystal structure, nonetheless each composition has nearly comparable Raman spectrum. The vibrational

spectrum depends on the variation of V compositions; some of the modes at lower-wavenumbers region were disappeared due to overlapping vibration. A significant shift of the higher-wavenumber modes is observed with respect to the degree of substitution of W^{5+} by V^{5+} cations. A collective feature for each sample is the presence of bands in the 850 cm^{-1} – 1050 cm^{-1} Raman shift region, an indication of the presence of terminal M=O bonds.

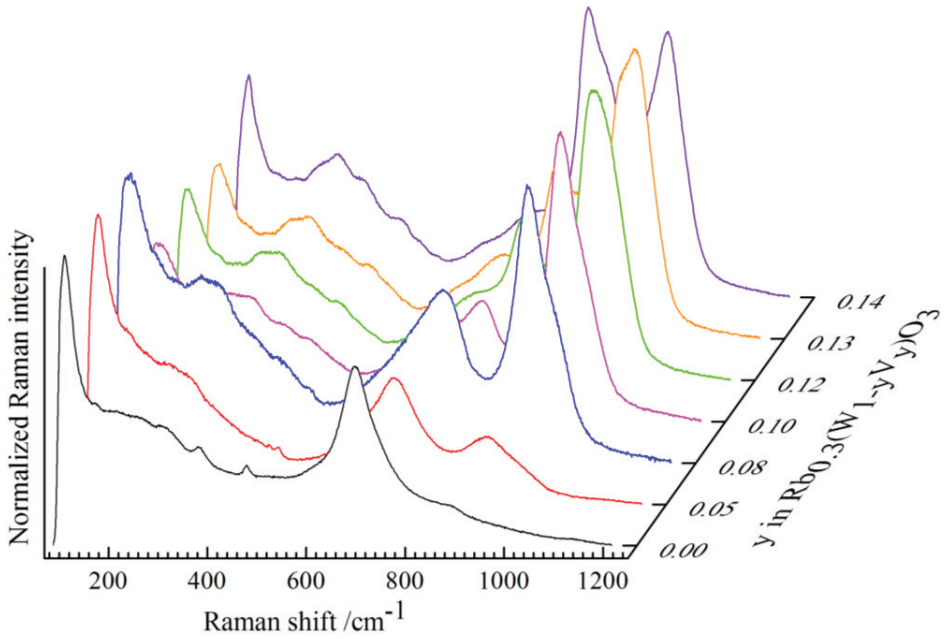

Figure 4.10. Raman spectra of polycrystalline vanadium substituted hexagonal rubidium tungsten bronzes, $Rb_{0.3}(W^{6+}_{0.7}W^{5+}_{0.3-y}V^{5+}_{y})O_3$ solid solution series.

The Raman peaks in the range of 80 cm^{-1} to 1050 cm^{-1} wavenumber given in the Figure 5.10 can be divided into two broad regions: 500 cm^{-1} – 1050 cm^{-1} and below 500 cm^{-1}. In the first part only the stretching vibrations of M–O and M=O (M = W, V) bonds are observed. The numbers of observable bands in this area are four to six. These are strongly dependent on the content of W^{6+}/W^{5+} and V^{5+} cations. Most of the bands are broad and their intensities are continually increasing. It suggests that the V^{5+} and W^{5+}/W^{6+} cations are statistically distributed in the same compound. Successive V^{5+} incorporation leads to narrow and sharp peaks. Additionally, the stretching bands show sequential positions shift with higher intensities. In the second region, the bending modes of O–W–O and W–O–W bridging bonds are observed. Some of the bands became broad and merged together with subsequent

incorporation of V^{5+} cations into the system. Such broadness of the peak is a consequences of all possible bending vibrations of W–O–M and O–M–O (M = $W^{6+}/W^{5+}/V^{5+}$) bonds. Since Rb–O bond distances are very large compared to normal Rb–O bond distance, the characteristic Raman peak could be found in the very low Raman shift region.

6.1. Structure of $Na_{0.6}(W^{6+}_{0.4}W^{5+}_{0.6})O_3$ bronze

The crystal structure of cubic perovskite-type tungsten bronze (PTB_C) of composition $Na_{0.6}(W^{6+}_{0.4}W^{5+}_{0.6})O_3$ is confirmed by the powder X-ray diffraction (XRD) data. Rietveld refinement was performed on collected powder XRD data and all the observed reflections are possible to index using single PTB_C phase of space group $Pm\bar{3}m$. This observation is in good agreement with earlier reports, describing by several authors [48, 81]. Rietveld refinement plot of powder XRD data and the details of the crystal structural feature of $Na_{0.6}(W^{6+}_{0.4}W^{5+}_{0.6})O_3$ bronze are given in Figure 6.1 and Table 6.1, respectively.

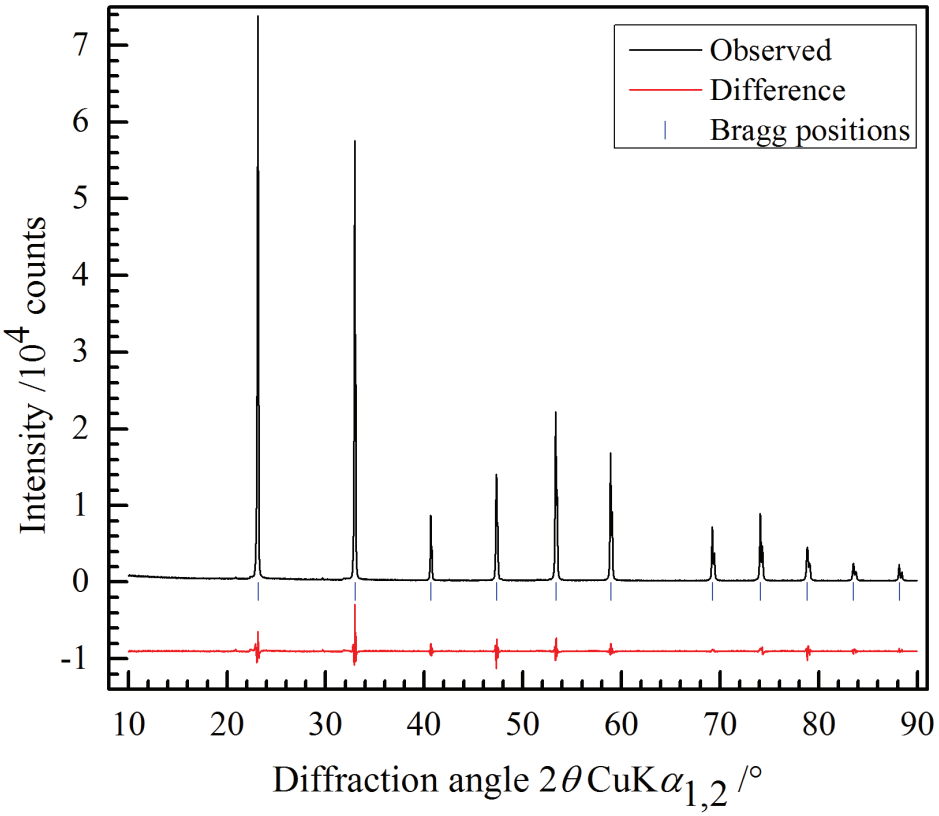

Figure 6.1. Rietveld refinement plot of powder X-ray diffraction data of $Na_{0.6}(W^{6+}_{0.4}W^{5+}_{0.6})O_3$ bronze ($Pm\bar{3}m$) measured at ambient conditions.

Table 6.1. Details of the crystal structure of $Na_{0.6}(W^{6+}_{0.4}W^{5+}_{0.6})O_3$ bronze obtained from powder X-ray diffraction data Rietveld refinement.

Space group: $Pm\bar{3}m$, a = 383.52(0) pm, V = 56.41(0)•10^6 pm^3, R_{wp} = 8 %						
Atom	Wyckoff	x	y	z	Occupancy	B_{eq} /10^4• pm^2
Na	1*a*	0	0	0	0.64(1)	1.58(25)
W	1*b*	½	½	½	1	0.18(4)
O	3*c*	½	½	0	1	0.77(9)

6.2. $Na_{0.6}(W^{6+}_{0.4}W^{5+}_{0.6-y}Ta^{5+}_{y})O_3$ solid solution series

Additional attempts were made for the preparation of $Na_{0.6}(W^{6+}_{0.4}W^{5+}_{0.6-y}Ta^{5+}_{y})O_3$ solid solution series with successive replacement of W^{5+} by Ta^{5+} cations up to the possible miscibility range using conventional solid state synthesis method. Repeated efforts always produced a mixture of two phase products. Incorporation of Ta^{5+} cation in the parent $Na_{0.6}(W^{6+}_{0.4}W^{5+}_{0.6})O_3$ bronze, there is a splitting of all reflections as a doublet of two closely related cubic phases having well separated lattice parameters as shown in Figure 6.2. The systematic development of the newly formed daughter ($Na_{0.6}(W^{6+}_{0.4}W^{5+}_{0.6-y}Ta^{5+}_{y})O_3$) phase and reduction of the parent ($Na_{0.6}(W^{6+}_{0.4}W^{5+}_{0.6})O_3$) phase is clearly shown in the enlarged view of Figure 6.2 for *211* reflection. There is a regular decrease of the intensities of all reflections for parent phase and successive development of that for the daughter phase which appeared as a shoulder in the lower 2θ-angles. This indicates the daughter phase has larger lattice parameter than that of the parent phase. With successive replacement of W^{5+} by Ta^{5+} cations the reflections which are located at lower diffraction angles (2θ) becoming more intense and clearly discernible. Both parent- and daughter phase crystallized in the same space group $Pm\bar{3}m$. The observed lattice parameters and their relative phase fractions are given in Table 6.2, obtained from Rietveld refinements. The change of the lattice parameter with respect to tantalum composition (y) of the daughter phase is shown in Figure 6.3(a). It shows that lattice parameter increases up to y = 0.3 and remain almost constant till y = 0.4, afterwards again increases to reach the maximum values for y = 0.6. There is a systematic decrease of the cell parameter of coexisting parent phase. The observed cell parameter of coexisting parent phase is plotted along with the calculated data using the equation: a [pm] =

378.46 [pm] + 8.19 [pm] • x) [90], proposed for perovskite-type cubic Na_xWO_3 (x = 0.4 - 1.0) bronzes.

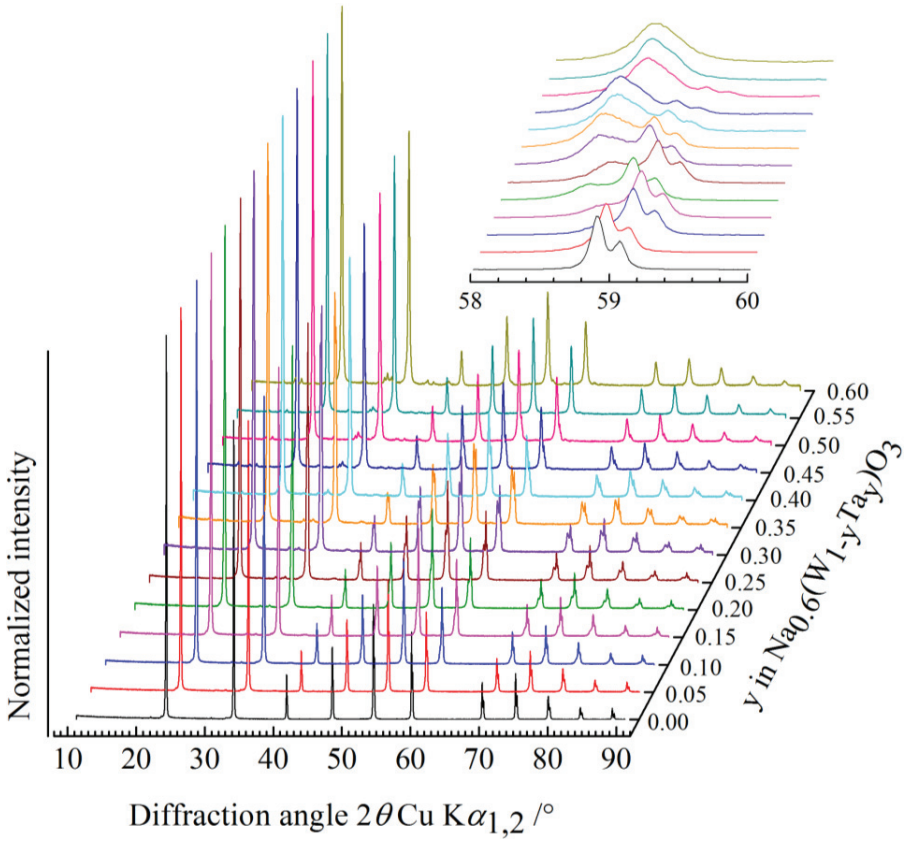

Figure 6.2. Powder X-ray diffraction patterns of $Na_{0.6}(W^{6+}_{0.4}W^{5+}_{0.6-y}Ta^{5+}_{y})O_3$ solid solution series. The enlarged view showed the splitting of *211* reflection of two cubic phases having well separated and closely related lattice parameters.

The relative x-composition of the coexisting parent phase is calculated from the observed lattice constant plotted in the Figure 6.3(b). The refined x-composition in the parent phase is reasonable up to y = 0.20, afterwards the differences ($x_{calc} - x_{obs}$) become significant and gradually increased up to y = 0.6. The refined x-compositions in the Ta^{5+}-doping phase are also given in Table 6.2. There is a huge differences between the observed x-compositions and the used nominal composition (x = 0.6) in the daughter phase as well. The systematic decrease of the lattice parameter of the coexisting parent phase is an indication of the reduction of x-composition. However, successive increase of the lattice parameter of daughter phase is a direct consequences of substitution of smaller W^{5+} (r = 62 pm [98]) by slightly

larger Ta^{5+} (r = 64 pm [98]) cations. The incorporated Ta^{5+} cations are statistically distributed in the same Wyckoff position (1*b*: ½, ½, ½), since both parent and daughter phases are crystallized in the same space group $Pm\bar{3}m$. The relative phase fractions of daughter phase are shown in Figure 6.3(c). The relative contributions of both phases showed complementary results like their lattice parameters change; that is the phase fractions of the parent phase decreased and that of the daughter phase increased with successive Ta^{5+}-doping in the system.

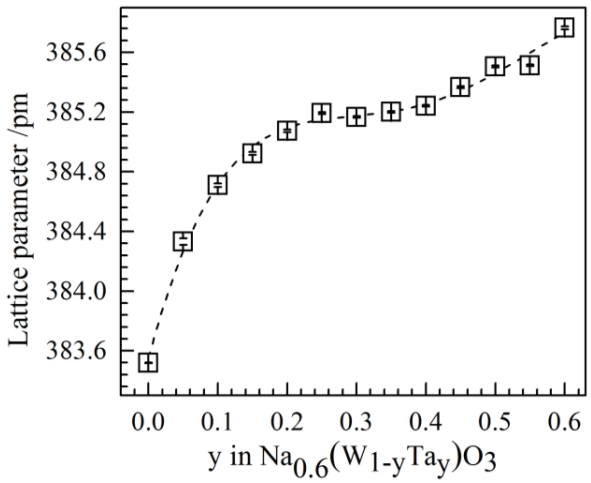

Figure 6.3(a). Lattice parameter change with respect to tantalum composition (y) in the $Na_{0.6}(W^{6+}_{0.4}W^{5+}_{0.6-y}Ta^{5+}_{y})O_3$ solid solution series. Dotted line is for eye-guide.

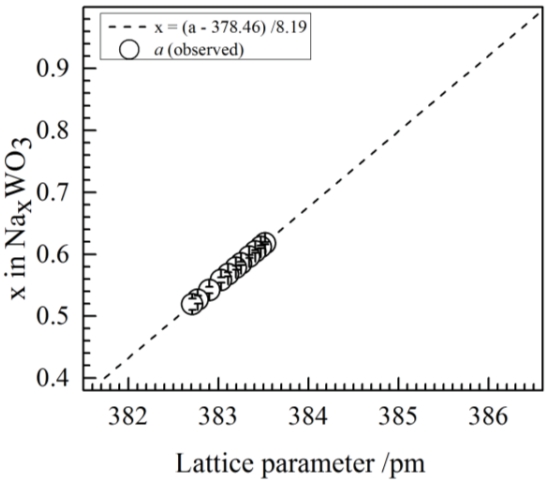

Figure 6.3(b). Observed cell parameters of the coexisting Na_xWO_3 bronzes are plotted along with the data obtained from the equation (ref [90]) given for cubic Na_xWO_3 bronze.

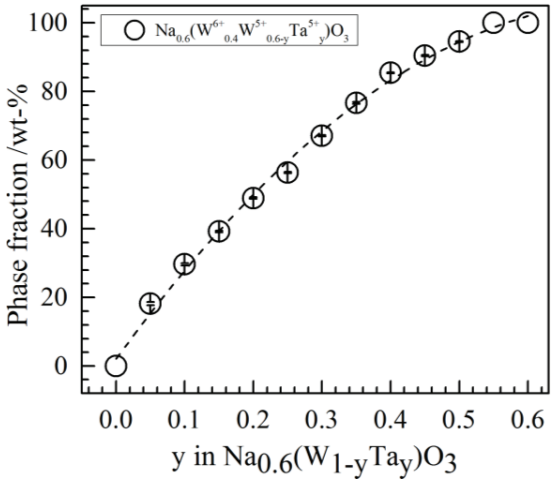

Figure 6.3(c). Phase fractions of daughter phase with respect to tantalum composition (y) for $Na_{0.6}(W^{6+}_{0.4}W^{5+}_{0.6-y}Ta^{5+}_{y})O_3$ solid solution series. Dotted line is for eye-guide.

Table 6.2. Rietveld refinements results of $Na_{0.6}(W^{6+}_{0.4}W^{5+}_{0.6-y}Ta^{5+}_{y})O_3$ solid solution series obtained from powder X-ray diffraction data.

y	$Na_x(W^{6+}_{1-x}W^{5+}_{x})O_3$				$Na_x(W^{6+}_{1-x}W^{5+}_{x--y}Ta^{5+}_{y})O_3$		
	wt-%	*a* /pm	x_{calc}	x_{obs}	wt-%	*a* /pm	x_{obs}
0.00	100	383.52(0)	0.628	0.64(1)	-	-	-
0.05	81.84(48)	383.47(0)	0.612	0.61(1)	18.16(48)	384.33(2)	0.73(3)
0.10	70.37(30)	383.41(0)	0.604	0.60(1)	29.63(30)	384.71(1)	0.77(2)
0.15	60.79(25)	383.34(0)	0.596	0.60(1)	39.21(25)	384.92(1)	0.76(1)
0.20	51.07(22)	383.25(0)	0.585	0.57(1)	48.93(22)	385.07(1)	0.69(1)
0.25	43.63(20)	383.20(0)	0.579	0.54(1)	56.37(20)	385.19(1)	0.70(1)
0.30	32.91(19)	383.11(0)	0.568	0.51(1)	67.09(19)	385.17(1)	0.69(1)
0.35	23.31(29)	383.03(0)	0.558	0.49(2)	76.69(29)	385.20(1)	0.65(1)
0.40	14.58(18)	382.90(0)	0.542	0.47(2)	85.42(18)	385.24(1)	0.64(1)
0.45	9.57(16)	382.77(0)	0.526	0.39(3)	90.43(16)	385.37(1)	0.63(1)
0.50	5.46(15)	382.71(1)	0.519	0.28(6)	94.54(15)	385.51(1)	0.66(1)
0.55	-	-	-	-	100	385.51(1)	0.64(1)
0.60	-	-	-	-	100	385.76(1)	0.65(2)

Miyamoto et al. [33] reported that the cell parameter increases in the $Na(W_{1-y}Nb_y)O_3$ series due to the substitution of Nb^{5+} instead of W^{5+} cations. Since Na_xWO_3 and $Na(W_{1-y}Nb_y)O_3$ have same crystallographic symmetry, the slightly lager Nb^{5+} (r = 64 pm [98]) cations played the role for the expansion of the lattice parameter. Recently, Debnath et al. [138] reported the results of Nb^{5+}-doping $Na_{0.8}(Nb_yW_{1-y})O_3$ series for $0 \leq y \leq 0.4$. The samples were prepared at 873 K in an evacuated silica tubes by conventional solid state synthesis method. This author found Nb^{5+}-dependent three coexisting perovskite-type cubic phases, identified as Na_xWO_3, $Na_x(Nb_yW_{1-y})O_3$ and $Na_{0.5}NbO_{2.75}$ compositions. The trend of the lattice parameter change, the variation of the x-composition and the relative contributions of the coexisting Na_xWO_3, $Na_x(Nb_yW_{1-y})O_3$ phases are in good agreement with this study. Dubson et al. [34] measured the electrical conductivity of cubic $Na_x(Ta_yW_{1-y})O_3$ bronzes from 1.6 K to 295 K for different x- and y compositions. The author prepared the single crystals of composition x = 0.60, y = 0.16 by electrolysis from the fused melt. Some sodium was diffused out by baking the

fragments of $Na_{0.6}(Ta_{0.16}W_{0.84})O_3$ single crystal at high-temperature for the preparation of $Na_x(Ta_{0.16}W_{0.84})O_3$ series for x = 0.27, 0.34, 0.35 and 0.45. Raychaudhuri [139] received the single crystals from Dubson et al. [34] and measured the low-temperature (0.1 K < T < 300 K) electrical conductivity of $Na_x(Ta_yW_{1-y})O_3$ bronzes for x = 0.35, y = 0.16 and x = 0.34, y = 0.16. Both authors studied the metal-insulator transition property of $Na_x(Ta_yW_{1-y})O_3$ bronzes with respect to x composition; however details of the crystal structural features are missing. Doumerc et al. [140] prepared single crystals of $Na_x(Ta_yW_{1-y})O_3$ from mixtures of Na_2WO_4, WO_3 and Ta_2O_5 by electrolytic reduction. The authors found that the lattice parameter of the cubic perovskite-type structure increases with respect to Ta^{5+} content. Electrical conductivity data of the $Na_x(Ta_yW_{1-y})O_3$ single crystal show metal-nonmetal transition for x – y, since the number of *d*- electrons decreases gradually. Weller et al. [32] investigated the effect of Nb^{5+} or Ta^{5+} cation incorporation into Na_xWO_3 bronzes. Polycrystalline samples of Nb^{5+} or Ta^{5+} doping $Na_{0.8}WO_3$ bronzes were prepared in air at about 998 K by electrolyzing a melt of $Na_2WO_4 \cdot 2H_2O$, WO_3, Nb_2O_5 and Ta_2O_5 contained into porcelain crucibles. It is reported that the lattice parameter increases up to 2 % of Nb^{5+} or 2.2 % of Ta^{5+} but detection of Nb^{5+} or Ta^{5+} was not possible by powder X-ray diffraction due to low dopant concentrations. Dubson et al. [34] argued that the chemical homogeneity and the mechanical quality of $Na_x(W_{1-y}Ta_y)O_3$ bronzes depend on several important parameters; e. g. the crystal growth temperature, the electrolytic current, duration of electrolysis, configuration of electrodes, materials of electrodes, crucible materials, the diffusion back temperature and time, etc. Na_xWO_3 bronze preparation is straightforward; however synthesis of pure single phase product of Ta^{5+}-doped $Na_x(W_{1-y}Ta_y)O_3$ is difficult by conventional solid state synthesis method. The WO_6 octahedra in the cubic structure of Na_xWO_3 bronzes are rigid enough. There is no possibility of out-of-center octahedral distortion; slightly larger Ta^{5+} cations leading to TaO_6 octahedral units which could not be easily compensate with the WO_6–octahedral networks.

SUMMARY

7.1 English

Keywords: Tungsten bronzes, second-order Jahn-Teller distortion, X-ray and neutron diffraction, Raman and infrared spectroscopy.

Series of Li_xWO_3 (x = 0.1 – 0.6) bronzes have been synthesized by solid state synthesis method. Samples with a composition of x = 0.1 ($Li_{0.1}WO_3$) crystallize as pure perovskite-type tungsten bronze showing orthorhombic symmetry (*Pcnb*), whereas for x = 0.4 – 0.6 single phases of cubic symmetry ($Im\bar{3}$) were found. A mixture of two phase products (*Pcnb* and $Im\bar{3}$) are observed for x = 0.2 and 0.3. With increasing lithium incorporation into the cubic phase (space group $Im\bar{3}$) the metric parameters gradually decreases which represents an opposite behavior with respect to cubic tungsten bronzes of Na, Gd and U. Polycrystalline samples of $Li_{0.4}WO_3$ bronzes produced at 973 K for 168 h using a pressure of 10^{-7} MPa resulted in pure phases showing $Im\bar{3}$ symmetry while using a pressure greater than 10^{-7} MPa always led to mixed phases showing $Im\bar{3}$ and $Pm\bar{3}m$ symmetry. Even using different reaction temperatures (973 K – 1073 K) and times (24 h to 168 h) at 10^{-7} MPa gave the same results for the formation of $Li_{0.4}WO_3$ bronze. Pure phases showing $Im\bar{3}$ symmetry (prepared at 10^{-7} MPa, 973 K, 168 h) transformed into a tetragonal phase crystallizing in space group *P*4/*nmm* when kept at ambient conditions in a glass-vial. However, samples left in the quartz tubes as synthesized at low-pressure do not change. The samples containing mixed phases after the synthesis (prepared above 10^{-7} MPa, 973 K, 168 h) transformed into $Pm\bar{3}m$ symmetry phases in a closed capillary and to phases of *P*4/*nmm* symmetry in open conditions. For the structure showing space group $Im\bar{3}$ two kinds of diffusion pathways have been proposed for Li^+: 6*b* → 6*b*, and 2*a* → 6*b* → 2*a*. Li^+ cannot move from one 2*a* to another 2*a* site without passing through the 6*b* site. We assume that once lithium hops to a 2*a* site, a 2*a* → 6*b* → 2*a* mechanism might happen leading to a $Im\bar{3}$ → *P*4/*nmm* phase transition. The transformation from $Im\bar{3}$ to $Pm\bar{3}m$ can be driven due to higher lithium content in the $Pm\bar{3}m$ phase as the lattice parameter of $Pm\bar{3}m$ is slightly smaller than that of the parent $Im\bar{3}$ phase. Temperature-dependent X-ray and neutron powder diffraction data reveal nonlinear expansions of the metric parameters for both $Li_{0.1}WO_3$ (*Pcnb*) and $Li_{0.4}WO_3$ ($Im\bar{3}$) bronzes. The temperature-

dependent NPD data Rietveld refinements allowed to explicitly locate lithium distributed on both 2*a* and 6*b* sites in the $Li_{0.4}WO_3$ bronze. With increasing temperature the loosely bonded lithium in the 6*b* site hops to the 2*a* site.

Polycrystalline samples of tantalum and vanadium substituted hexagonal tungsten bronzes of potassium or rubidium (HTB's) with nominal compositions of $A_{0.3}(W^{6+}_{0.7}W^{5+}_{0.3-y}Ta^{5+}_{y})O_3$ (A = K or Rb, y = 0 – 0.3), $A_{0.3}(W^{6+}_{0.7}W^{5+}_{0.3-y}V^{5+}_{y})O_3$ (A = K or Rb, y = 0 – 0.18), and $K_{0.3}(W^{6+}_{0.7}W^{5+}_{0.3-y}Ta^{5+}_{y/2}V^{5+}_{y/2})O_3$ (y = 0 – 0.3) were synthesized by solid state reactions in quartz tubes at 10^{-7} MPa and 1073 K. The K-HTB series samples crystallize in space group $P6_322$ while Rb-HTB could be described in space group $P6_3/mcm$. In these HTB compositions, W^{5+} could fully be replaced by Ta^{5+}, whereas V^{5+} could only be substituted up to y = 0.15. Repeated attempts showed that W^{5+} can only be partially replaced by Ta^{5+} in the HTB phase for $y < 0.1$, producing a single phase. Samples synthesized with nominal compositions of $y \geq 0.1$ showed a mixture of two phases, namely, HTB-I (W^{5+} is partially replaced) and HTB-II (W^{5+} is more or less fully replaced, oxidized phase), both of which conform the parent space group $P6_322$ for the K-HTB and $P6_3/mcm$ for the Rb-HTB series. The phase fraction of the HTB-II increased with increasing nominal Ta^{5+} composition till reaching a fully oxidized bronzoid phase, that is, $A_{0.3}(W^{6+}_{0.7}Ta^{5+}_{0.3})O_3$. The $A_{0.3}(W^{6+}_{0.7}W^{5+}_{0.3-y}V^{5+}_{y})O_3$ series could be produced with pure HTB-type phases up to y = 0.15. For $y > 0.15$ mixtures of two phases were observed; V^{5+} substituted HTB's along with additional non-bronze (impurity) phase. Whereas the formation of pure single phase samples during the incorporation of Ta^{5+} in the $A_{0.3}(W^{6+}_{0.7}W^{5+}_{0.3-y}Ta^{5+}_{y})O_3$ series is limited to $y < 0.1$ and those of V^{5+} to y = 0.15 for $A_{0.3}(W^{6+}_{0.7}W^{5+}_{0.3-y}V^{5+}_{y})O_3$ their co-doping changed the miscibility to y = 0.3 (Ta^{5+} and V^{5+} = 0.15 each) in the $K_{0.3}(W^{6+}_{0.7}W^{5+}_{0.3-y}Ta^{5+}_{y/2}V^{5+}_{y/2})O_3$ solid solution series. With increasing Ta^{5+} or V^{5+} concentration the *a*- and *c*-cell parameters change anisotropically, that is, the *a*-cell parameter decreases while the *c*-parameter increases followed by non-linear increase of the anisotropy factor ($A = |a - c|$). The degree of W^{5+} substitution is explained in terms of second-order Jahn-Teller (SOJT) distortion of the d^0 cations W^{6+}, Ta^{5+} and V^{5+}. The applied distortion index also demonstrate a complete substitution of W^{5+} in $K_{0.3}(W^{6+}W^{5+})O_3$ by a concomitant sharing of Ta^{5+} and V^{5+}, which are statistically distributed on the W^{5+}/W^{6+} sites. Since $W^{5+}(d^1)$ is not SOJT susceptible, it is also shown that the concentration of W^{5+} in tungsten bronzes plays an important role in the local

WO_6 octahedral symmetry. Substitution of W^{5+} with SOJT susceptible $Ta^{5+}(d^0)$ is assumed to incorporate additional distortion to the MO_6 octahedra. Since Ta^{5+} is a weak distorter like W^{6+}, the out-of-center octahedral distortion index (Δ_d) fluctuates within a narrow range for the $A_{0.3}(W^{6+}_{0.7}W^{5+}_{0.3-y}Ta^{5+}_{y})O_3$ series. Opposite, V^{5+} is a strong distorter, even stronger than W^{6+}. Therefore the MO_6 octahedra in the $A_{0.3}(W^{6+}_{0.7}W^{5+}_{0.3-y}V^{5+}_{y})O_3$ system develops the magnitude of Δ_d with increasing y; the weakly distorted parent system transformed into strongly distorted MO_6 octahedra for y = 0.15. W^{5+} substituted by V^{5+} and Ta^{5+} simultaneously leading to set new SOJT distortion (magnitude of Δ_d) which ultimately limits the range of chemical miscibility. To accommodate moderate Ta^{5+} and strong V^{5+} SOJT distorters the system prefers other possible low-energy cost mechanism such as tilting and twisting of the WO_6 octahedra. The overall consequence can be observed in the expansion-contraction behaviors of the metric parameters as y-compositions increases.

7.2 German

Stichwörter: Wolframbronzen, Jahn-Teller-Verzerrung zweiter Ordnung, Röntgen- und Neutronenbeugung, Raman und Infrarot Spektroskopie

Mischkristallreihen von Li_xWO_3 (x = 0.1 – 0.6) Bronzen wurden mittels Festkörpersynthese dargestellt. Bronzen mit einer Zusammensetzung von x = 0.1 ($Li_{0.1}WO_3$) kristallisierten als reiner Perovskit-Typ mit orthorhombischer Symmetry (*Pcnb*), wohingegen man für x = 0.4 – 0.6 Phasen eine kubischer Symmetrie ($Im\bar{3}$) findet. Für die Zusammensetzung x = 0.2 und 0.3 wurde ein Phasengemisch (*Pcnb* and $Im\bar{3}$) erhalten. Mit steigendem Einbau von Lithium in die kubische Phase (Raumgruppe $Im\bar{3}$) sinken die Metrikparameter graduell, was gegensätzlich zum Verhalten der kubischen Wolframbronzen, welche Na, Gd und U enthalten steht. Polykristalline $Li_{0.4}WO_3$-Bronzen, welche für 168 h bei 973 K und einem Druck von 10^{-7} MPa synthetisiert wurden, resultierten in reinphasigen Produkten mit $Im\bar{3}$ Symmetrie, wohingegen ein größerer Druck als 10^{-7} MPa immer zu einem Phasengemisch der Phasen mit $Im\bar{3}$ und $Pm\bar{3}m$ Symmetrie führte. Auch eine Variation der Reaktionstemperaturen (973 K – 1073 K) und Temperzeiten (24 h bis 168 h) bei 10^{-7} MPa resultierte in der Bildung einer $Li_{0.4}WO_3$ Bronze. Reinphasen in der Symmetrie $Im\bar{3}$ (hergestellt bei 10^{-7} MPa, 973 K, 168 h) zeigten eine Phasenumwandlung zu einer tetragonalen Phase mit der Raumgruppe *P*4/*nmm* bei Lagerung unter Standardbedingungen in einer Glasphiole. Proben welche nach der

Synthese unverändert bei niedrigem Druck im nicht geöffneten Quarzrohr belassen wurden, zeigten dagegen keine Änderung. Proben, die nach der Synthese Phasengemische beinhalteten (Druck größer 10^{-7} MPa, 973 K, 168 h) zeigten eine Phasenumwandlung zur *Pm*$\bar{3}$*m* Symmetrie in geschlossenen Kapillaren und zu einer *P*4/*nmm* Symmetrie unter Standardbedingungen. Für die Struktur in der Raumgruppe *Im*$\bar{3}$ wurden zwei Diffusionswege für das Li^+ vorgeschlagen: 6*b* → 6*b*, und 2*a* → 6*b* → 2*a*. Li^+ kann sich dabei nicht ohne Umweg über die 6*b* Lage von einer 2*b* zur anderen 2b Lage bewegen. Wir vermuten dass Lithium nach einem Sprung zur 2*a* Lage einem 2*a* → 6*b* → 2*a* Mechanismus folgt, woraus eine *Im*$\bar{3}$ → *P*4/*nmm* Phasenumwandlung resultiert. Die Transformation von *Im*$\bar{3}$ to *Pm*$\bar{3}$*m* wird durch den höheren Lithiumgehalt der *Pm*$\bar{3}$*m* Phase ermöglicht, da deren Gitterparameter geringfügig kleiner ist als jener in der *Im*$\bar{3}$ Phase. Temperaturabhängige Röntgen- und Neutronenbeugungsdaten zeigen nichtlineare Expansionen der Metrikparameter für $Li_{0.1}WO_3$ (*Pcnb*) und $Li_{0.4}WO_3$ (*Im*$\bar{3}$) Bronzen. Die Rietveld-Verfeinerungen an temperaturabhängigen Pulver-Neutronenbeugungsdaten erlaubten ein explizites lokalisieren der Lithiumatome verteilt auf den Lagen 2*a* und 6*b* in $Li_{0.4}WO_3$. Das schwach gebundene Lithium auf der 6*b* Lage migriert mit steigender Temperatur auf die Lage 2*a*.

Polykristalline Proben Tantal- und Vanadium-substituierter hexagonaler Wolframbronzen mit Kalium oder Rubidium (HTB's) der nominalen Zusammensetzungen $A_{0.3}(W^{6+}_{0.7}W^{5+}_{0.3-y}Ta^{5+}_{y})O_3$ (A = K oder Rb, y = 0 – 0.3), $A_{0.3}(W^{6+}_{0.7}W^{5+}_{0.3-y}V^{5+}_{y})O_3$ (A = K oder Rb, y = 0 – 0.18), und $K_{0.3}(W^{6+}_{0.7}W^{5+}_{0.3-y}Ta^{5+}_{y/2}V^{5+}_{y/2})O_3$ (y = 0 – 0.3) wurden mittels Festkörpersynthese in Quarzröhrchen bei 10^{-7} MPa und 1073 K synthetisiert. Die K-HTB-Serie kristallisiert in der Raumgruppe *P*$6_3$22 wohingegen die Rb-HTB-Serie in der Raumgruppe *P*6_3/*mcm* beschrieben werden kann. In diesen HTB-Zusammensetzungen konnte W^{5+} vollständig durch Ta^{5+} substituiert werden, mit V^{5+} nur bis zu y = 0.15. Wiederholte Versuche zeigten, dass zum Erhalt eines reinphasigen Produkts W^{5+} in der HTB-Phase nur partiell bis $y < 0.1$ durch Ta^{5+} substituiert werden kann. Proben welche mit nominalen Zusammensetzungen von $y \geq 0.1$ synthetisiert wurden zeigten eine Mischung aus zwei Phasen, bestehend aus HTB-I (W^{5+} partiell ausgetauscht) und HTB-II (W^{5+} mehr oder weniger komplett ausgetauscht, oxidierte Phase), beide entsprechend beschreibbar in der Raumgruppe *P*$6_3$22 für die K-HTB und *P*6_3/*mcm* für die Rb-HTB-Serie. Der Anteil der HTB-II-Phase steigt mit einem größer werdenden nominalen Ta^{5+} Gehalt bis zum Erreichen der voll oxidierten Phase

$A_{0.3}(W^{6+}_{0.7}Ta^{5+}_{0.3})O_3$. Die Synthese der Serie $A_{0.3}(W^{6+}_{0.7}W^{5+}_{0.3-y}V^{5+}_{y})O_3$ führte bis y = 0.15 zu reinphasigen Produkten des HTB-Typs. Für y > 0.15 wurden zweiphasige Mischungen bestehend aus V^{5+} substituierten HTB's und Phasen die nicht dem Bronze-Typ entsprechen (Verunreinigungen) erhalten. Während die Bildung einphasiger Proben bei dem Einbau von Ta^{5+} in die Serie $A_{0.3}(W^{6+}_{0.7}W^{5+}_{0.3-y}Ta^{5+}_{y})O_3$ bis zu y < 0.1 und jener von V^{5+} in die Serie $A_{0.3}(W^{6+}_{0.7}W^{5+}_{0.3-y}V^{5+}_{y})O_3$ bis zu y = 0.15 limitiert ist, änderte ein co-doping die Mischbarkeit auf y = 0.3 (Ta^{5+} und V^{5+} = 0.15) in $K_{0.3}(W^{6+}_{0.7}W^{5+}_{0.3-y}Ta^{5+}_{y/2}V^{5+}_{y/2})O_3$ Mischkristallen. Mit steigender Ta^{5+} oder V^{5+} Konzentration verändern sich die *a*- und *c*-Gitterparameter anisotrop, wobei der *a*-Gitterparameter kleiner und der c-Gitterparameter größer wird, gefolgt von einem nicht-linearen Anstieg des Anisotropiefaktors ($A = |a - c|$). Der Grad der Substitution von W^{5+} wird durch einen Jahn-Teller-Effekt zweiter Ordnung (SOJT) der d^0-Kationen W^{6+}, Ta^{5+} und V^{5+} erklärt. Der verwendete Verzerrungsindex zeigt eine vollständige Substitution von W^{5+} in $K_{0.3}(W^{6+}W^{5+})O_3$ durch eine gleichzeitige Mischbesetzung von Ta^{5+} und V^{5+}, welche statistisch auf die Lagen von W^{5+}/W^{6+} verteilt sind. Da ein Jahn-Teller-Verzerrung zweiter Ordnung für $W^{5+}(d^1)$ nicht möglich ist, wird gezeigt, dass die Konzentration von W^{5+} in Wolframbronzen eine wichtige Rolle für die lokale Symmetrie der WO_6-Oktaeder spielt. Für eine Substitution von W^{5+} mit SOJT zugänglichem $Ta^{5+}(d^0)$ wird das Einringen zusätzlicher Verzerrungen in das MO_6-Oktaeder vermutet. Da Ta^{5+} ein schwacher Verzerrer wie W^{6+} ist, fluktuiert der „out-of-center" Oktaeder-Verzerrungsindex (Δ_d) für die Serie $A_{0.3}(W^{6+}_{0.7}W^{5+}_{0.3-y}Ta^{5+}_{y})O_3$ in einem schmalen Bereich. Andererseits ist V^{5+} ein starker Verzerrer, stärker noch als W^{6+}. Daher entwickelt das MO_6-Oktaeder im System $A_{0.3}(W^{6+}_{0.7}W^{5+}_{0.3-y}V^{5+}_{y})O_3$ eine zunehmende Größen von Δ_d mit steigendem y; das schwach verzerrte Ursprungssystem transformiert zu stark verzerrten MO_6-Oktaedern für y = 0.15. Gleichzeitige Substitution von W^{5+} durch V^{5+} und Ta^{5+} führt zu einer neuen SOJT-Verzerrung (Größenordnung von Δ_d), welche den Bereich der chemischen Mischbarkeit endgültig limitiert. Zum Einbau von moderaten Ta^{5+} und starken V^{5+} SOJT-Verzerrern neigt das System zu anderen möglichen energiesparenden Mechanismen wie dem Kippen und Drehen der WO_6-Oktaeder. Die resultierende Konsequenz wird im der Expansions/Kontraktions Verhalten der Metrikparameter bei steigendem y beobachtet.

REFERENCES

[1] F. Wöhler, *Ann. Chim. Phys*. **43** (1823) 29.

[2] R.J.D. Tilley, *Int. J. Refract. Met. Hard Mater*. **13** (1995) 93.

[3] E. Salje, *Acta Crystalogr*. **B 33** (1977) 574.

[4] B. Gerand, G. Nowogrocki, J. Guenot, M. Figlarz, *J. Solid State Chem*. **29** (1979) 429.

[5] K.H. Cheng, A.J. Jacobson, M.S. Whittingham, *Solid State Ionics* **5** (1981) 355.

[6] C.J. Howard, H.T. Stokes, *Acta Crystallogr*. **A 61** (2005) 93.

[7] G. Hägg, *Nature* **135** (1935) 874.

[8] G. Hägg, *Z. Phys. Chem*. **B 29** (1935) 192.

[9] A. Laurent, *Ann. Chim. Phys*. **67** (1838) 215.

[10] L.A. Hallopeau, *Ann. Chim. Phys*. **19** (1900) 92.

[11] E. Schäfer, *Z. Anorg. Allg. Chem*. **38** (1903) 142.

[12] H.R. Shanks, *J. Cryst. Growth* **13/14** (1972) 433.

[13] A. Hussain, *Chem. Commun*. University of Stockholm, No. 2 (1978) 1.

[14] P. Labbe, *Key Eng. Mater*. **68** (1992) 293.

[15] T. Ekström, R.J.D. Tilley, *Chem. Scr*. **16** (1980) 1.

[16] L. Bartha, A.B. Kiss, T. Szalay, *Int. J. Refract. Met. Hard Mater*. **13** (1995) 77.

[17] R.K. Stanley, R.C. Morris, W.G. Moulton, *Phys. Rev*. **B 20** (1979) 1903.

[18] M.J. Sienko, S.M. Morehouse, *Inorg. Chem*. **2** (1963) 485.

[19] C.G. Granqvist, *Sol. Energy Mater. Sol. Cells* **60** (2000) 201.

[20] C.J. Raub, A.R. Sweedler, M.A. Jensen, S. Broadston, B.T. Matthias, *Phys. Rev. Lett*. **13** (1964) 746.

[21] L.H. Cadwell, R.C. Morris, W.G. Moulton, *Phys. Rev*. **B 23** (1981) 2219.

[22] S. Reich, G. Leitus, Y. Tssaba, Y. Levi, A. Sharoni, O. Millo, *J. Supercond. Inc. Nov. Magn*. **13** (2000) 855.

[23] G. Leitus, H. Cohen, S. Reich, *Phys*. **C 371** (2002) 321.

[24] L. Kihlborg, R. Sharma, *J. Microsc. Spectrosc. Electron*. **7** (1982) 387.

[25] A. Deschanvres, M. Frey, B. Raveau, J.C. Thomazeau, *Bull. Soc. Chim. Fr*. (1968) 3519.

[26] R. Sharma, L. Kihlborg, *Mater. Res. Bull*. **16** (1981) 377.

[27] R. Sharma, *Mater. Res. Bull*. **20** (1985) 1373.

[28] I.P. Klimova, V.I. Voronkova, V.K. Yanovskii, *Inorg. Mater*. **31** (1995) 245.

[29] R. Sabatier, G. Baud, *J. Inorg. Nucl. Chem*. **34** (1972) 873.

[30] X. Yang, C. Li, M.-S. Mo, J. Zhan, W. Yu, Y. Yan, Y. Qian, *J. Cryst. Growth* **249** (2003) 594.

[31] Z. Gu, Y. Ma, T. Zhai, B. Gao, W. Yang, J. Yao, *Chem. Eur. J*. **12** (2006) 7717.

[32] P.F. Weller, B.E. Taylor, R.L. Mohler, *Mater. Res. Bull*. **5** (1970) 465.

[33] Y. Miyamoto, S. Kume, J.-P. Doumerc, P. Hagenmuller, *Mater. Res. Bull*. **18** (1983) 1463.

[34] M.A. Dubson, D.F. Holcomb, *Phys. Rev*. **B 32** (1985) 1955.

[35] A. Hussain, A. Ul-monir, M.M. Murshed, C.H. Rüscher, *Z. Anorg. Allg. Chem*. **628** (2002) 416.

[36] K.R. Dey, Synthesis and Chacterisation of Alkali Metal Tungsten Bronzes; Li_xWO_3 and $M_xM'_yW_{1-y}O_3$ (M = Li, Na, Cs and M`= Nb, Mo) Systems, Universität Hannover, 2004.

[37] T. Debnath, Structure, Chemical Composition and Optical Property Relationship of Alkali-Metal Tungsten Oxides and Niobium Tungsten Oxides, Universität Hannover, 2008.

[38] T. Debnath, S.C. Roy, C.H. Rüscher, A. Hussain, *J. Mater. Sci*. **44** (2009) 179.

[39] M.M.R. Shakil, T. Debnath, C.H. Rüscher, A. Hussain, *J. Bangladesh Chem. Soc*. **25** (2012) 38.

[40] A.M. Abdullah, T. Debnath, C.H. Rüscher, A. Hussain, *J. Sci. Res*. **4** (2012) 507.

[41] S.A. Lawrence, S. Stevenson, K. Mavadia, P.A. Sermon, *Proc. R. Soc. Lond. A. Math. Phys. Sci*. **411** (1987) 95.

[42] K.L. Ngai, T.L. Reinecke, *J. Phys. F: Met. Phys*. **8** (1978) 151.

[43] K.L. Ngai, R. Silberglitt, *Phys. Rev*. **B 13** (1976) 1032.

[44] A.S. Ribnick, B. Post, E. Banks, in:, Adv. Chem., ACS, 1963, pp. 246–253.

[45] A. Magnéli, *Acta Chem. Scand*. **5** (1951) 670.

[46] K.R. Dey, C.H. Rüscher, T.M. Gesing, A. Hussain, *Mater. Res. Bull*. **42** (2007) 591.

[47] C.H. Rüscher, K.R. Dey, T. Debnath, I. Horn, R. Glaum, A. Hussain, *J. Solid State Chem*. **181** (2008) 90.

[48] B.W. Brown, E. Banks, *J. Am. Chem. Soc*. **76** (1954) 963.

[49] M.E. Straumanis, S.S. Hsu, *J. Am. Chem. Soc*. **72** (1950) 4027.

[50] P.J. Wiseman, P.G. Dickens, *J. Solid State Chem*. **17** (1976) 91.

[51] A. Magnéli, *Ark. Foer Kemi* **1** (1949) 213.

[52] L. Kihlborg, A. Klug, *Chem. Scr*. **3** (1973) 207.

[53] F. Takusagawa, R.A. Jacobson, *J. Solid State Chem*. **18** (1976) 163.

[54] A. Magnéli, *Acta Chem. Scand*. **7** (1953) 315.

[55] J. Ranninger, K.P. Sinha, *Proc. Indian Acad. Sci*. **95** (1985) 93.

[56] T.E. Gier, D.C. Pease, A.W. Sleight, T.A. Bither, *Inorg. Chem*. **7** (1968) 1646.

[57] N.D. Zakharov, P. Werner, I.P. Zibrov, V.P. Filonenko, M. Sundberg, *Cryst. Res. Technol*. **35** (2000) 713.

[58] X. Xu, H.W. Schmalle, J.R. Günter, *Solid State Ionics* **76** (1995) 221.

[59] P.E. Bierstedt, T.A. Bither, F.J. Darnell, *Solid State Commun*. **4** (1966) 25.

[60] A. Hussain, L. Kihlborg, *Acta Crystallogr*. **A 32** (1976) 551.

[61] A. Hussain, *Acta Chem. Scand*. **A 32** (1978) 479.

[62] T. Ekström, R.J.D. Tilley, *J. Solid State Chem*. **24** (1978) 209.

[63] T. Ekström, R.J.D. Tilley, *J. Solid State Chem*. **28** (1979) 259.

[64] M.M. Dobson, J.L. Hutchison, R.J.D. Tilley, K. A. Watts, *J. Solid State Chem*. **71** (1987) 47.

[65] N.D. Zakharov, Z.L. Weber, V.P. Filonenko, I.P. Zibrov, M. Sundberg, *Mater. Res. Bull*. **31** (1996) 373.

[66] N.D. Zakharov, P. Werner, I.P. Zibrov, V.P. Filonenko, M. Sundberg, *J. Solid State Chem*. **147** (1999) 536.

[67] R. Sharma, *Acta Chem. Scand*. **A 39** (1985) 397.

[68] M.J. Sienko, in:, Adv. Chem., ACS, 1963, pp. 224–236.

[69] B.W. Brown, E. Banks, *Phys. Rev*. **84** (1951) 609.

[70] L.D. Ellerbeck, H.R. Shanks, P.H. Sidles, G.C. Danielson, *J. Chem. Phys*. **35** (1961) 298.

[71] H.R. Shanks, P.H. Sidles, G.C. Danielson, in:, Adv. Chem., ACS, 1963, pp. 237–245.

[72] A.R. Sweedler, C.J. Raub, B.T. Matthias, *Phys. Lett*. **15** (1965) 108.

[73] W.A. Kamitakahara, K. Scharnberg, H.R. Shanks, *Phys. Rev. Lett*. **43** (1979) 1607.

[74] J.D. Greiner, H.R. Shanks, D.C. Wallace, *J. Chem. Phys*. **36** (1962) 772.

[75] P.G. Dickens, M.S. Whittingham, *Q. Rev. Chem. Soc*. **22** (1968) 30.

[76] L.E. Conroy, M.J. Sienko, *J. Am. Chem. Soc*. **74** (1952) 3520.

[77] D.R. Wanlass, M.J. Sienko, *J. Solid State Chem*. **12** (1975) 362.

[78] R.J. Bouchard, J.L. Gillson, *Inorg. Chem*. **7** (1968) 969.

[79] A. Magnéli, *Nov. Acta Regiæ Soc. Sci. Ups*. [4] **14** (1950).

[80] J.F. Owen, K.J. Teegarden, H.R. Shanks, *Phys. Rev*. **B 18** (1978) 3827.

[81] J.F. Smith, G.C. Danielson, *J. Chem. Phys*. **22** (1954) 266.

[82] M.E. Straumanis, *J. Am. Chem. Soc*. **71** (1949) 679.

[83] K.S. Park, H.G. Kim, Y.H. Kim, C.H. Park, K. Do Kim, *Chem. Eng. Res. Des*. **89** (2011) 2389.

[84] F. Corà, M.G. Stachiotti, C.R.A. Catlow, C.O. Rodriguez, *J. Phys. Chem*. **B 101** (1997) 3945.

[85] O. Glemser, C. Naumann, *Z. Anorg. Allg. Chem*. **265** (1951) 288.

[86] P.G. Dickens, R.J. Hurditch, *Nature* **215** (1967) 1266.

[87] G.M. Sheldrick, Shelxs-86, Progr. Cryst. Struct. Determ. Univ. Göttingen, Ger. (1986).

[88] G.M. Sheldrick, Shelxl-93, Progr. Refinement Cryst. Struct. Univ. Göttingen, Ger. (1993).

[89] A.C. Larson, R.B. Von Dreele, Gen. Struct. Anal. Syst. (GSAS), Los Alamos Natl. Lab. Rep. LAUR (2004) 86.

[90] M.A. Wechter, H.R. Shanks, A.F. Voigt, *Inorg. Chem*. **7** (1968) 845.

[91] T. Vogt, P.M. Woodward, B.A. Hunter, *J. Solid State Chem*. **144** (1999) 209.

[92] Q. Zhong, J.R. Dahn, K. Colbow, *Phys. Rev*. **B 46** (1992) 2554.

[93] K. H. Cheng, M.S. Whittingham, *Solid State Ionics* **1** (1980) 151.

[94] R.J. Cava, A. Santoro, D.W. Murphy, S.M. Zahurak, R.S. Roth, *J. Solid State Chem*. **50** (1983) 121.

[95] M.S. Rahman, M.M. Murshed, T.M. Gesing, *Zeitschrift Für Krist. - Cryst. Mater*. **229** (2014) 797.

[96] W.H. Jones Jr., E.A. Garbaty, R.G. Barnes, *J. Chem. Phys*. **36** (1962) 494.

[97] E. Banks, A. Goldstein, *Inorg. Chem*. **7** (1968) 966.

[98] R.D. Shannon, *Acta Crystallogr*. **A 32** (1976) 751.

[99] A.J. Mark, I.D. Raistrick, R.A. Huggins, *J. Electrochem. Soc*. **130** (1983) 776.

[100] P.S. Halasyamani, K.R. Poeppelmeier, *Chem. Mater*. **10** (1998) 2753.

[101] A.D. Walkingshaw, N.A. Spaldin, E. Artacho, *Phys. Rev*. **B 70** (2004) 165110.

[102] S.T. Triantafyllou, P.C. Christidis, C.B. Lioutas, *J. Solid State Chem*. **133** (1997) 479.

[103] M.M. Murshed, T.M. Gesing, *Mater. Res. Bull*. **48** (2013) 3284.

[104] T.M. Gesing, C.B. Mendive, M. Curti, D. Hansmann, G. Nénert, P.E. Kalita, K.E. Lipinska, A. Huq, A.L. Cornelius, M.M. Murshed, *Zeitschrift Für Krist. - Cryst. Mater*. **228** (2013) 532.

[105] M.M. Murshed, C.B. Mendive, M. Curti, G. Nénert, P.E. Kalita, K. Lipinska, A.L. Cornelius, A. Huq, T.M. Gesing, *Mater. Res. Bull*. **59** (2014) 170.

[106] M. Boulova, N. Rosman, P. Bouvier, G. Lucazeau, *J. Phys. Condens. Matter* **14** (2002) 5849.

[107] M.F. Pye, P.G. Dickens, *Mater. Res. Bull*. **14** (1979) 1397.

[108] A.J. Schultz, H. Horiuchi, *Acta Crystallogr*. **C 42** (1986) 641.

[109] D.M. Sagar, D. Fausti, S. van Smaalen, P.H.M. van Loosdrecht, *Phys. Rev*. **B 81** (2010) 045124.

[110] J.P. Doumerc, F. Kabbaj, G. Campet, J. Claverie, M. Pouchard, *Solid State Coummnications* **39** (1981) 1045.

[111] K.R. Dey, T. Debnath, C.H. Rüscher, M. Sundberg, A. Hussain, *J. Mater. Sci*. **46** (2011) 1388.

[112] M. Maczka, J. Hanuza, A. Majchrowski, *J. Raman Spectrosc*. **32** (2001) 929.

[113] K. Robinson, G. V. Gibbs, P.H. Ribbe, *Science* **172** (1971) 567.

[114] P.S. Halasyamani, *Chem. Mater*. **15** (2004) 3586.

[115] R.G. Pearson, *Proc. Nat. Acad. Sci.* USA **72** (1975) 2104.

[116] I.D. Brown, http://www.ccp14.ac.uk/ccp/web-Mirrors/i_d_brown/ (2006).

[117] I.D. Brown, *Acta Crystallogr*. **B 33** (1977) 1305.

[118] M.E. Fleet, *Mineral. Mag*. **40** (1976) 531.

[119] H.G. Bachmann, F.R. Ahmed, W.H. Barnes, *Zeitschrift Für Krist. Bd*. **115** (1961) 110.

[120] L. Kihlborg, A. Hussain, *Mater. Res. Bull*. **14** (1979) 667.

[121] J. Guo, C. Dong, L. Yang, H. Chen, *Mater. Res. Bull*. **43** (2008) 779.

[122] P. Labbé, M. Goreaud, B. Raveau, J.C. Monier, *Acta Crystallogr*. **B 34** (1978) 1433.

[123] R. Brusetti, P. Bordet, J. Marcus, *J. Solid State Chem*. **172** (2003) 148.

[124] J. Oi, A. Kishimoto, T. Kudo, *J. Solid State Chem*. **103** (1993) 176.

[125] N.C. Stephenson, A.D. Wadsley, *Acta Crystallogr*. **18** (1965) 241.

[126] J. Graham, A.D. Wadsley, *Acta Crystallogr*. **20** (1966) 93.

[127] H. Bartl, D. Schuster, F.A. Schröder, *Zeitschrift Für Krist*. **149** (1979) 127.

[128] M. Ghedira, J. Chenavas, M. Marezio, *J. Solid State Chem*. **57** (1985) 300.

[129] D. Yin, J. Wang, R. Wang, J. Shi, H. Zou, *J. Phys. Condens. Matter* **16** (2004) 9001.

[130] W.J. Schutte, J.L. de Boer, *Acta Crystallogr*. **B 49** (1993) 579.

[131] L.E. Depero, M. Zocchi, F. Zocchi, F. Demartin, *J. Solid State Chem*. **104** (1993) 209.

[132] W.G. Mumme, J.A. Watts, *J. Solid State Chem*. **2** (1970) 16.

[133] K. Eda, F. Kunotani, N. Uchiyama, *J. Solid State Chem*. **178** (2005) 1471.

[134] M. Sato, B.H. Grier, H. Fujishita, S. Hoshino, A.R. Moodenbaugh, *J. Phys. C: Solid State Phys.* **16** (1983) 5217.

[135] R. Brusetti, H. Schober, P. Bordet, S. Eibl, J. Bossy, *Phys. Rev*. **B 76** (2007) 174511.

[136] J.F. Scott, R.F. Leheny, J.P. Remeika, A.R. Sweedler, *Phys. Rev*. **B 2** (1970) 3883.

[137] F. Galasso, W. Darby, *J. Phys. Chem*. **68** (1964) 1253.

[138] T. Debnath, C.H. Rüscher, T.M. Gesing, J. Koepke, A. Hussain, *J. Solid State Chem*. **181** (2008) 783.

[139] A.K. Raychaudhuri, *Phys. Rev*. **B 44** (1991) 8572.

[140] J.-P. Doumerc, J. Marcus, M. Pouchard, P. Hagenmuller, *Mater. Res. Bull*. **14** (1979) 201.